Subcellular proteomics and iPSC modeling uncover reversible mechanisms of axonal pathology in Alzheimer's disease

Yifei Cai [1, #], Jean Kanyo [2, *], Rashaun Wilson [2, *], Shveta Bathla [3, 4, *], Pablo Leal Cardozo [4, *], Lei Tong [1, *], Shanshan Qin [5, *], Lukas A. Fuentes [6, *], Iguaracy Pinheiro-de-Sousa [7, *], Tram Huynh [1, *], Liyuan Sun [1, *], Mohammad Shahid Mansuri [3, 4], Zichen Tian [1], Hao-Ran Gan [1], Amber Braker [8], Hoang Kim Trinh [1], Anita Huttner [9], TuKiet T. Lam [2, 3, 10], Evangelia Petsalaki [7], Kristen J. Brennand [4, 11], Angus C. Nairn [3, 4, 12], Jaime Grutzendler [1, 13, #]

1. Department of Neurology, Yale University, New Haven, CT 06511
2. Keck MS & Proteomics Resource, Yale University, New Haven, CT, 06511
3. Yale/NIDA Neuroproteomics Center, Yale University, New Haven, CT 06511
4. Department of Psychiatry, Yale University, New Haven, CT 06511
5. John A. Paulson School of Engineering and Applied Sciences, Harvard University, Cambridge, MA, USA 02134
6. Department of Cell Biology, Yale University School of Medicine, New Haven, CT, 06511
7. European Molecular Biology Laboratory, European Bioinformatics Institute, Hinxton, UK
8. Yale College, Department of Neuroscience, Yale University, New Haven, CT 06520
9. Department of Pathology, Yale University, New Haven, CT 06520
10. Department of Molecular Biophysics and Biochemistry, Yale University, New Haven, CT, 06511
11. Department of Genetics, Yale University, New Haven, CT 06520
12. Department of Pharmacology, Yale University, New Haven, CT 06520
13. Department of Neuroscience, Yale University, New Haven, CT 06511

[*] These authors contributed equally.

[#] Correspondence: yifei.cai@yale.edu, jaime.grutzendler@yale.edu

ABSTRACT

Axonal spheroids (dystrophic neurites) are commonly found around amyloid deposits in Alzheimer's disease (AD). They impair electrical conduction, disrupt neural circuits, and correlate with AD severity. Despite their significance, the mechanisms underlying spheroid formation remain unknown. To address this, we developed a proximity labeling proteomics approach to uncover the proteome of spheroids in human postmortem and mouse brains. Additionally, we established a human iPSC-derived AD model allowing mechanistic investigation of spheroid pathology and optical electrophysiology. This approach revealed the subcellular molecular architecture of spheroids and identified abnormalities in key biological processes, including protein turnover, cytoskeleton dynamics, and lipid transport. Notably, the PI3K/AKT/mTOR pathway, which regulates these processes, was activated within spheroids. Furthermore, phosphorylated mTOR levels in spheroids strongly correlated with AD severity in humans. Importantly, inhibition of mTOR in iPSC-derived neurons and in mice ameliorated spheroid pathology. Altogether, our study provides a multidisciplinary toolkit for investigating mechanisms and novel targets for axonal pathology in neurodegeneration.

INTRODUCTION

A major pathological hallmark in Alzheimer's disease (AD) is the accumulation of aggregated extracellular β-amyloid (Aβ) peptide deposits [1]. However, the precise mechanisms through which these deposits trigger downstream neuronal changes and contribute to cognitive deficits remain unknown. While amyloid plaques have been shown to cause overall synapse loss [2] and dendritic spine reduction in their vicinity [3], a less understood, yet potentially critical pathological hallmark are the axonal spheroids that develop around plaques. Specifically, we and others have shown that hundreds of axons but not dendrites in the vicinity of individual amyloid plaques develop enlarged spheroid-like structures (traditionally termed dystrophic neurites) [4-10]. These plaque-associated axonal spheroids (PAAS) have been shown to correlate with AD severity [4, 11] and markedly disrupt axonal electrical conduction [4, 12, 13] and neuronal network function [4], potentially leading to cognitive impairment. PAAS contain large numbers of enlarged and enzyme-deficient endolysosomal vesicles [4, 14-16], and autophagosomes [15, 17]. Spheroid enlargement may be driven by the accumulation of these vesicles [4], and by the disruption of axonal cytoskeleton and transport [16, 18-22]. Ultimately, the presence of axonal spheroids may further impair axonal trafficking, leading to downstream synaptic dysfunction and axonal degeneration [3, 23-25]. Additionally, it has been proposed that PAAS may play a role in the propagation of tau pathology through neuronal networks [26]. Therefore, PAAS could be a critical neuropathological hub implicated in circuit disruption and proteinopathy, contributing to cognitive decline in AD [3, 4, 12, 13, 23, 27].

Axonal spheroids can form as a result of a variety of insults and have been observed in many pathological processes, ranging from acute neural injury to age-related neurodegenerative conditions. These spheroids share morphological and subcellular cytoskeletal and organelle similarities, including the accumulation of certain proteins such as Amyloid Precursor Protein (APP) and Cathepsins [14, 22]. However, significant mechanistic differences exist given the diversity of pathological processes involved. For example, in models of neural injury, spheroid formation has been shown to depend on alterations in the cytoskeleton and disruption of axonal and membrane tension [22, 28]. This process is associated with phosphatidylserine exposure, leading to glial phagocytosis [22, 29]. Conversely, in Alzheimer's disease, plaque-associated spheroids have been shown to be long-lasting and are not typically engulfed by phagocytes [4, 30-32].

Despite these observations, PAAS have not been a major focus of mechanistic investigations, and the cell biological processes involved in their formation remain poorly understood. In this study, we developed a proteomics approach to systematically investigate the molecular composition of PAAS, by employing proximity labeling to selectively isolate the subcellular proteome of PAAS in human postmortem and mouse brain. Using this approach, we uncovered the presence of protein turnover, cytoskeleton dynamics and lipid transport as key biological processes in PAAS. Furthermore, we identified hundreds of previously unknown proteins and signaling pathways that are expressed in PAAS, some of which could play important roles in PAAS formation.

83 To investigate the structural dynamics, functional consequences, and potential reversibility of
84 PAAS, we established a versatile human iPSC-derived AD model that recapitulates PAAS
85 pathology. This model enabled us to conduct longitudinal imaging of PAAS and optical
86 electrophysiology using calcium sensors in human neurons, revealing the growth patterns and
87 disruption in action potential conduction caused by PAAS. To further investigate the mechanisms
88 of spheroid growth, we focused on the mTOR signaling pathway which was identified in the PAAS
89 proteomics and confirmed to be expressed within PAAS. Both genetic and pharmacological
90 inhibition of the mTOR pathway in human iPSC neurons and in mice led to a marked reduction in
91 PAAS pathology. Given that mTOR is a master regulator of protein turnover, lipid metabolism and
92 axonal cytoskeletal remodeling [33-35], these findings underscore the importance of these
93 biological processes in PAAS formation.
94
95 Altogether, the integration of subcellular proteomics in postmortem human brain, human iPSC
96 AD modeling, and molecular manipulation of PAAS in human neurons and mice, provides new
97 insight into the complex cell biology and reversibility of axonal pathology in AD.

RESULTS

Proximity labeling of proteins within axonal spheroids in the human postmortem AD brain

Proximity labeling is a recently developed methodology used to biotinylate proteins within a specific cellular or subcellular compartment through genetic expression of localized peroxidases or biotin ligases in living cells and animals [36-40]. This method allows the selective protein isolation and subsequent identification of subcellular proteomes using liquid chromatography with tandem mass spectrometry (LC-MS/MS) technology [41, 42]. A modification of this approach was recently introduced enabling localized protein biotinylation in fixed tissues, by means of horseradish peroxidase (HRP)-conjugated antibodies targeted to a subcellular compartment [43-46]. Leveraging these methodologies, we devised and refined an antibody-based proximity labeling approach to uncover the proteome of PAAS in both human AD postmortem brains and AD-model mice (5XFAD) (**Figure 1; Figures S1-S4 and Movie S1**).

Our approach was based on the observation that phospholipase D3 (PLD3), an endolysosomal protein, is highly abundant within PAAS (**Figures 1C and S2E-G**) [4, 47-50], and is specifically expressed in neurons [4, 47] and absent in glial cells [4]. Although low levels of PLD3 are also found in neuronal cell bodies (**Figure S2**), quantitative immunofluorescence demonstrated that the majority of PLD3 originates from PAAS (**Figure S2G**). Leveraging this finding, we used PLD3 as a protein bait for proximity labeling proteomics of PAAS. This involved the sequential incubation of postmortem AD human or mouse brains with primary antibody against PLD3 and secondary HRP-conjugated antibody, followed by a peroxidation reaction in the presence of hydrogen peroxide and Biotin-XX-Tyramide (**Figure 1D**). This resulted in robust biotinylation of proteins contained within PAAS, as confirmed by streptavidin labeling, with minimal background outside the boundaries of axonal spheroids (**Figures 1E-H**). To further validate the spatial precision of proximity labeling, we employed Stimulated Emission Depletion (STED) super-resolution imaging, demonstrating the high precision of proximity labeling of axonal spheroids in AD human brains (**Figure S3**). Additionally, to provide evidence of the subcellular specificity of proximity labeling, we conducted parallel experiments utilizing the neuronal nuclear and perinuclear cytoplasm marker NeuN as the protein bait. (**Figure S2C-D**).

Furthermore, we optimized the protein lysis method, resulting in a significant improvement in protein extraction efficiency compared to previous studies [43]. This new protocol involved increased SDS concentration to 2% in basic Tris-HCl solution (pH = 8.0), which led to significantly increased protein extraction yield by effectively decrosslinking proteins in fixed postmortem tissue (**Figure S4A** and method section). Using this approach, we performed pulldown of biotinylated proteins from the lysed tissues and subsequently detected them through streptavidin-HRP western blotting. Our analysis revealed a diverse array of proteins, including the protein baits PLD3 or NeuN, along with axonal spheroid proteins RAGC and Cathepsin B (**Figures 1I and Figures S4B-D**). Thus, the refined proximity labeling method for postmortem brain samples provides a robust strategy for tagging and isolating proteins enriched in axonal spheroids, thereby facilitating comprehensive mass-spectrometry-based proteomic profiling.

Proteomic analysis of plaque-associated axonal spheroids

To uncover the proteome of axonal spheroids, samples from individuals with AD and unaffected controls were processed for PLD3 proximity labeling protein biotinylation (**Figures 2A and S5**). Human frontal cortex postmortem samples were obtained from 39 individuals, sourced from the Yale Alzheimer's Research Center (Yale ADRC, n = 8 AD and 2 control samples) and the Banner Sun Health Research Institute (Banner, n = 17 AD and 12 control samples), with detailed clinical and postmortem neuropathological data (**Figure S1**). All AD subjects exhibited high levels of amyloid plaques and other pathological hallmarks of AD, while control individuals had minimal or no amyloid plaque burden. For PAAS proximity labeling proteomics, we selected 6 AD individuals (3 females and 3 males), with the highest amyloid plaque burden (**Figure S1C**), along with 8 unaffected controls (3 females and 5 males). Additionally, 25 AD individuals (13 females and 12 males) and 7 unaffected controls (2 females and 5 males) were chosen for immunofluorescence validation of protein expression.

Through proteomic analysis of these human samples, we identified a total of 2,360 proteins (**Figures 2B and 2C**). The process of identifying the PAAS proteomes involved three steps (**Figures 2B and 2C**). First, to eliminate non-specific protein binders to beads, we compared PLD3 antibody-labeled samples to no-antibody samples, using cutoffs for p-value of < 0.05, false discovery rate (FDR) < 0.1, and fold change > 1.5. To ensure the stringency of the proteomic data, we compared normalized total precursor intensity (NTPI) and normalized total spectra count (NTSC) methods for quantification (**Figure S6**). We found that 870 proteins (NTSC) and 965 proteins (NTPI) remained after applying these statistical cutoffs, and 849 proteins were shared between the two methods. Next, we used the 849 shared proteins for downstream analysis. Second, we searched for glial cell-specific proteins and found only two (see method section), which were then excluded from the dataset, leaving 847 proteins. Finally, we aimed to exclude proteins specific to neuronal soma and neuropil, by comparing the proteomes of PLD3 antibody-labeled AD samples to unaffected controls, applying cutoffs for p-value of < 0.05 and fold change > 1.5 or < 0.67. Given that the PLD3-labeling in unaffected controls is derived from neuronal soma and neuropil given the lack of plaques, the proteins with fold change > 1.5 (98 proteins) represented those enriched in PAAS and/or broadly increased in AD, while those with a fold change < 0.67 (51 proteins) represented those specific to neuronal soma and neuropil, and/or proteins decreased in AD (**Figure 2B**). To increase stringency, we removed proteins with a fold change < 0.67 from the PAAS proteomic dataset (**Figure 2B**). As a result, 821 proteins remained, representing the PAAS proteomes in AD humans, all of which exhibited a fold change enrichment greater than 1.95 (**Figures 2B, 2C, Figures S7-S8 and Table S1**).

For comparative analysis, parallel experiments were conducted with 15-month-old 5XFAD mice (**Figure S9**). Using a similar proteomic strategy, we identified 856 PAAS proteomic hits in mice (**Figures 2A-C, Figure S9A** and **Table S1**, also see method section). All 856 proteins had a fold change greater than 1.66 (**Table S1**), among which 476 proteins were shared between AD humans and 5XFAD mice (**Figure S9B**). The proteomic analyses in both humans and mice uncovered hundreds of proteins that were not previously known to be expressed in PAAS, as well as those previously reported (**Figure 2D, Figure S9A and S10, and Table S2**).

184 Various controls were implemented to ensure specificity. This included additional proteomics
185 using Lamp1 as a bait in 5XFAD mice, which detected 510 overlapping protein hits with PLD3
186 However, Lamp1 proximity labeling also detected many more proteins derived from glial cells
187 (**Figure S11**), consistent with its expression in these cells. To further confirm the robustness of
188 proteomic hits, we used anti-biotin beads for pulldown of biotinylated peptides, showing results
189 that were highly consistent with those from the streptavidin beads pulldown (**Figure S12**).
190 Additionally, to further examine the subcellular specificity of the antibody-based proximity
191 labeling proteomic approach, we included NeuN, a neuronal nuclei and perinuclear cytoplasm
192 marker [51], as a control protein bait. In contrast to the PLD3-labeled PAAS proteome, the NeuN-
193 labeled proteome showed distinct specificity to nuclei and neuronal soma (**Figure S13 and Table**
194 **S1**).

195 **Protein turnover and cytoskeletal dynamics are key signatures in axonal spheroids**

196 To gain insights into the molecular mechanisms associated with axonal spheroid pathology, we
197 conducted Gene Ontology (GO) annotation of biological process, molecular function and cellular
198 component using the human PAAS proteomics dataset of 821 proteins, followed by pathway
199 enrichment analysis. The results showed that the proteomic hits were mainly associated with
200 axon, synapse, cytoskeleton, lysosome and proteosome complex (Figure **3A and Table S4**). These
201 findings likely reflect the axonal origin of PAAS and the massive accumulation of endolysosomal
202 organelles within them, as demonstrated by immunofluorescence imaging and electron
203 microscopy (**Figures 1B-C and Movie S1**) [4, 14]. Since many synapse-related proteins are
204 involved in vesicle fusion, such as the SNARE complex, these proteins are also actively involved
205 in endolysosomal function. Given the fact that PAAS structures do not contain pre- and post-
206 synaptic features (**Movie S1**), we speculate that the synapse-related signatures from the GO
207 annotation imply the presence of vesicle fusion processes within the endolysosomal pathway.
208
209 Next, we performed signaling pathway analysis using the human PAAS proteome. We found that
210 10 out of the top 17 CNS-related pathways are involved in three main modules: synapse/vesicle
211 fusion, protein turnover and cytoskeleton (**Figure 3B**), which is consistent with the findings from
212 the GO analysis (**Figure 3A**). Specifically, among these pathways, we identified 5 pathways related
213 to the cytoskeleton (e.g., axonal guidance), 3 related to synapse and vesicle fusion (e.g.,
214 synaptogenesis), and 2 related to protein turnover (e.g., phagosome maturation) (**Figure 3B** and
215 **Table S5**). Additionally, beyond the top-ranked pathways, we also observed signaling pathways
216 related to synapse and vesicle fusion, such as Clathrin-mediated endocytosis signaling, as well as
217 pathways related to cytoskeleton growth and dynamics, such as actin cytoskeletal signaling and
218 Rho family GTPase signaling (**Figure 3C**). Furthermore, pathways related to protein turnover, such
219 as protein ubiquitination, autophagy and phagosome formation, were also identified. In addition,
220 we noted the activation of the PI3K/AKT and mTOR signaling pathways, along with inhibition of
221 the PTEN signaling (**Figure 3C**), all of which have been implicated in the regulation of protein
222 turnover and axonal growth [52]. Importantly, subsets of proteomic hits from these identified
223 pathways were observed to be increased in AD humans compared to controls (**Figure 3D**).
224
225 To confirm the expression of proteomic hits in PAAS, we selected various proteins from different
226 pathways for validation using high-resolution immunofluorescence confocal microscopy. These

227 included proteins associated with synaptogenesis, vesicle fusion, and calcium signaling (e.g.,
228 SYT11 and CAMK2A), and proteins involved in cytoskeleton dynamics (e.g., SPTBN1) (**Figure 3E,**
229 **Figure S14 and Table S2**). A complete list of validated proteins in this study can be found in **Figure**
230 **S10** and **Table S2**. For immunofluorescence validation, we used either SMI312 or PLD3 to reveal
231 the structure of PAAS. SMI312 labels neurofilament and serves as a pan-axonal marker. Under
232 normal conditions, SMI312 signals reveal the typical morphology of axons. However, in the
233 context of AD, SMI312 is not only expressed along axons but also accumulates significantly in
234 PAAS, indicating cytoskeletal abnormalities. SMI312 has been widely validated as a marker for
235 PAAS due to its ability to highlight these structures in pathological conditions [15, 16]. Spheroids
236 can be easily identified with this marker, making SMI312 very useful for colocalizations studies in
237 conjunction with other antibodies. However, SMI312 is only expressed in a subset of spheroids
238 [14]. Similarly, the newly validated proteins from our proteomic dataset demonstrate
239 heterogeneity in the degree of expression. This heterogeneous protein expression pattern within
240 spheroids suggests a potential mechanistic sequence of events at various stages during spheroid
241 formation and growth.
242
243 Additionally, we conducted parallel PAAS proteomics analysis in 5XFAD mice. Similar to the
244 human PAAS proteome, we observed the presence of GO terms related to axon, cytoskeleton,
245 SNARE binding, as well as lysosome and endosome transport (**Figure S9C**). In addition, many
246 signaling pathways related to synapse/vesicle fusion, protein turnover and cytoskeleton
247 dynamics were captured in the PAAS proteomes from 5XFAD mice **(Figures S9D-E).**

248 **Lipid transport signaling is markedly upregulated in axonal spheroids**

249 To investigate the aberrant signaling in PLD3-labeled AD brains compared to unaffected controls,
250 we employed gene set enrichment analysis (GSEA) (**Figure 4A and Table S6**). This analysis
251 revealed a significant upregulation of biological processes related to lipid transport (**Figures 4A**
252 **and 4B**). Among the top-ranked proteins associated with these processes were ATP8A1, C3, APOE,
253 ATG9A, ATP8A2, TMEM30A, HEXB, and HDLBP (**Figure 4C**), all of which were identified in the
254 PAAS proteome and increased in AD (**Figure 4D**, related to **Figure 2B, and Figure S10**). Conversely,
255 GSEA analysis demonstrated the downregulation of biological processes related to ribosome,
256 translation, and RNA metabolism in PLD3-labeled AD brains compared to unaffected controls
257 (**Figure 4A**). Given that the PLD3-labeled signals in unaffected controls are derived from neuronal
258 soma and neuropil, these downregulated signals reflect the protein functions associated with
259 neuronal soma and neuropil identified in the unaffected control brains.
260
261 To validate the enrichment of the top-ranked lipid-related proteomic hits found in PAAS,
262 including APOE, HDLBP, C3, HEXB, and TMEM30A, we performed immunofluorescence confocal
263 imaging (**Figures 4E, 4F and Figure S15A**). Notably, APOE, which is the strongest genetic risk
264 factor for AD and a lipid transporter [53], was among the top hits. We observed varying degrees
265 of expression of these proteins in axonal spheroids in AD human brains (**Figures 4E, 4F, Figure**
266 **S15A and Table S2**). Among them, Complement C3 (C3), APOE and high-density lipid binding
267 protein (HDLBP) exhibited the highest expression in axonal spheroids and aberrant axons around
268 amyloid plaques, but much less in distal axons away from plaques (**Figure 4E, Figure S15A and**
269 **Table S2**). Additionally, these proteins were found to be expressed in cell bodies, neuropil, and

amyloid plaque-related regions, consistent with their expected protein distribution patterns (**Figure S15A and Table S2**). Notably, HDLBP showed a peculiar pattern of segregation within a subset of thickened axon segments where the pan-axonal marker SMI312 was absent (**Figure 4G**), suggesting that lipid metabolism dysregulation may precede the enlargement of axonal spheroids. Regarding HEXB, known to be specifically expressed in microglia in mice [54], we found that in human brains it was expressed in PAAS and neuronal cell bodies (**Figure S15B**), consistent with human single cell transcriptional profiles [55].

mTOR signaling is expressed in axonal spheroids and phosphorylated mTOR S2448 correlates with Alzheimer's disease

The PAAS proteomics results drew our focus to the PI3K/AKT/mTOR axis, as it emerged as an activated signaling pathway within PAAS (**Figure 3C** and **Figure S9E**). This pathway is known to be a master regulator of mRNA translation, metabolism and protein turnover [35, 52]. In line with this, protein turnover, lipid metabolism, and axonal cytoskeleton dynamics were identified as prominent signatures in our proteomic analysis (**Figures 3, 4 and Figure S9D-E**) [33-35]. Therefore, we selected key proteins within the PI3K/AKT/mTOR axis for validation. Among them, mTOR, RAGA (RRAGA), RAGC (RRAGC), LAMTOR1 and AKT1 were detected in the PAAS proteomes in humans and/or mice, while PIK3R4, RHEB and RAPTOR were not detected (**Figure S10 and Tables S1 and S2**). Immunofluorescence staining revealed the presence of all selected proteins associated with the PI3K/AKT/mTOR axis in axonal spheroids in both postmortem AD human brains and 5XFAD mice (**Figure 5A**). The proteins that were detected in the PAAS proteomes showed moderate to high immunofluorescence signals in spheroids, while those that were not detected showed moderate to low expression (**Figure 5A and Table S2**). Notably, phosphorylated-mTOR-S2448, a marker of mTOR signaling activation, was found to be expressed in axonal spheroids in AD human brains, but not in unaffected controls (**Figures 5B-D**). This observation suggests that phosphorylated-mTOR-S2448 could potentially serve as a marker for disease progression. Overall, these findings underscore the involvement and activation of the PI3K/AKT/mTOR axis within axonal spheroids in AD.

Human iPSC modeling replicates cellular and functional abnormalities of axonal spheroids

To establish a comprehensive strategy for investigating selected proteomic hits and their potential roles in spheroid formation, we utilized long-term human iPSC-derived neuron [56] and astrocyte co-cultures (**Figures 6A-B and S16A-D**). A similar approach was recently shown to replicate the formation of axonal spheroids upon administration of exogenous aggregated β-amyloid 1-42 [57]. We simplified the human neuron induction protocol by using the *NGN2*-induced glutamatergic neuron approach [56] (see method section), making it more accessible for most laboratories. Additionally, we increased the overall neuronal density in the cultures to better mimic the axonal spheroids observed around amyloid plaques in the human brain. Our optimized model successfully generated Thioflavin S-positive amyloid deposits surrounded by many axonal spheroids (**Figures 6B, Figures S16E-F, S17A and S18B-C**). These spheroids accumulated lysosomes and autophagosomes (**Figures 6B-C**), and expressed phosphorylated Tau S235, S396 and S404 (**Figure S16G**), closely resembling axonal spheroids in humans [4, 58].

313 This culture system enabled us to perform longitudinal structural and functional imaging,
314 providing insights into the dynamics and consequences of spheroid pathology. By utilizing
315 reporter AAV-viruses to label neurons and lysosomes, we were able to track the formation of
316 spheroids following administration of Aβ 1-42. By visualizing individual axons through confocal
317 microscopy, we observed the gradual formation of spheroids and lysosomal accumulation as
318 early as day 1, with spheroids increasing in size over a 7-day observation period after treatment
319 (**Figures 6C**).
320
321 We also investigated the functional repercussions of spheroid formation in this human iPSC-
322 derived AD model. Employing calcium imaging with the reporter GCaMP8f, we measured the Ca^{2+}
323 rise time in axonal segments on both sides of axonal spheroids following electrical stimulation.
324 We observed a significant difference in the slope of the calcium rise time in process segments
325 with spheroids compared to those without (**Figures 6D-F**). This is consistent with impaired action
326 potential conduction across the spheroids in human neurons, similar to our earlier in vivo findings
327 in 5XFAD mice [4]. Additionally, we noted a very prolonged calcium decay time in process
328 segments with spheroids relative to normal processes and somata, indicating disrupted calcium
329 homeostasis within spheroids (**Figures 6G-H**).
330
331 **mTOR signaling inhibition reduces spheroid pathology in human neurons**
332 We further explored the role of PI3K/AKT/mTOR signaling in the development and expansion of
333 axonal spheroids using the human iPSC model. Consistent with our observations in postmortem
334 human brains (**Figure 5**), the human iPSC-derived AD model exhibited the expression of proteins
335 associated with the PI3K/AKT/mTOR signaling pathway within axonal spheroids (**Figure 6I and**
336 **Figure S17**).
337
338 To assess the impact of mTOR inhibition on axonal spheroid pathology, we utilized Torin1, a
339 compound that inhibits both mTORC1 and mTORC2 [59, 60]. Treating 3-month-old iPSC-derived
340 human neurons and astrocyte co-cultures with Torin1 for 7 days led to a significant suppression
341 of mTOR signaling, evidenced by reduced levels of mTOR downstream effectors p-p70 S6K (Thr
342 389) and p-4E BP1 (Thr 37/46), without affecting their total protein levels (**Figure 6J**). To assess
343 the effects of Torin1 on the formation and reversibility of axonal spheroids, we treated cultures
344 with Torin1 either before or after β-amyloid exposure and spheroid formation. Pre-treatment
345 with Torin1 prior to Aβ exposure resulted in a considerable decrease in both the number and size
346 of individual spheroids (**Figures 6K-P**), while treatment with Torin1 after Aβ exposure reduced
347 the number of spheroids but did not alter their size (**Figures 6Q-R and Figures S18A-C**).
348 Importantly, none of these outcomes were attributable to axonal loss (**Figure 6N and Figure**
349 **S18D**), changes in neuronal density or amyloid plaque size (**Figures 6O, 6P, Figures S16H-I and**
350 **S18E**). Thus, our findings indicate that mTOR signaling plays an important role in amyloid-induced
351 spheroid formation and suggest that targeting mTOR could be a promising approach for both
352 preventing and reversing, as well as initiation and maintenance of spheroid pathology.
353
354 **Amelioration of spheroid pathology in 5XFAD mice through genetic manipulation of mTOR**
355 To investigate the effect of mTOR signaling on axonal spheroids in vivo, we employed a viral-
356 mediated Cre/lox-based *Mtor* knockout approach in 5XFAD mice (**Figures 7A-C and S19A-D**).

357 Using heterozygous *Mtor*-floxed-5XFAD mice [61] and infecting them with AAV9-hsyn-cre-2a-
358 tdTomato, we achieved partial loss of mTOR expression in neurons. Sparse neuronal infection
359 allowed us to clearly visualize individual spheroids (**Figures 7D-E**), revealing a significant decrease
360 in axonal spheroid size following heterozygous *Mtor* knockout (**Figures 7F-G**).
361
362 To assess the overall impact on spheroid size and number, we measured the axonal spheroid halo
363 size around individual amyloid plaques. For this, we infected *Mtor*-floxed-5XFAD mice with AAV-
364 PHP.eB-hSyn-Cre-GFP virus, enabling dense neuronal infection, thereby inducing widespread
365 *Mtor* heterozygous knockout in neurons (**Figures 7H and Figures S19B, D and E**). This
366 manipulation significantly reduced the axonal spheroid halo size around plaques without
367 affecting amyloid plaque size (**Figures 7I-J and Figures S19E-H**). Importantly, despite mTOR's
368 known role in cell growth and maturation [35, 59], the heterozygous *Mtor* knockout did not alter
369 the size of neuronal cell bodies (**Figure 7K and Figure S19F**). These in vivo findings in mice,
370 paralleling those in vitro with human iPSC-derived neurons, highlight the potential of
371 PI3K/AKT/mTOR signaling as a therapeutic target for mitigating axonal spheroid pathology in AD.
372
373 Signaling pathways associated with lysosome biogenesis and autophagy are likely to play
374 important roles in the accumulation of aberrant endolysosomes in spheroids. In addition, local
375 mRNA translation has been shown to be important for axonal outgrowth, which could play a role
376 in spheroid formation [62, 63]. Considering the known effects of mTOR on lysosome biogenesis,
377 autophagy and local mRNA translation [35, 52], we explored related downstream molecules.
378 Using AAV-PHPeB-hSyn-Cre to induce extensive neuronal infection in mTOR-heterozygous-
379 floxed-5XFAD mice, we achieved widespread mTOR heterozygous knockout specifically in
380 neurons (**Figures 7A-C and 7H**). Immunofluorescence confocal imaging was used to assess the
381 expression levels of TFEB (lysosomal biogenesis transcription factor), p-p70S6K (regulator of
382 mRNA local synthesis), and LC3B (a marker of autophagy) in neuronal somata, with automated
383 quantitative analysis comparing expression between mTOR heterozygous knockout mice and
384 controls (**Figures 7L-O**). Results indicated increased expression of TFEB and LC3B (**Figures 7L-M**),
385 suggesting enhanced lysosomal biogenesis and autophagy. Additionally, the levels of p-p70S6K
386 were decreased (**Figures 7N-O**), which may be associated with reduction in mRNA local
387 translation [52].
388
389 We further examined whether mRNA local translation occurs at axonal spheroids. Initially, we
390 probed the presence of mRNA species in axonal spheroids using RNAscope in 5XFAD mice (**Figure**
391 **7P and Figure S20A**). For this we used a probe against mRNA polyA tails and compared labeling
392 patterns to a scrambled control probe. We found that the polyA but not the control probe signal
393 was present in axonal spheroids, indicating the localization of mRNA in these structures (**Figure**
394 **7Q and Figures S20B-D**) (see methods for spheroid detection during RNAscope). Next, we
395 examined the occurrence of mRNA local translation at axonal spheroids by performing an *in vivo*
396 puromycylation assay in 5XFAD mice (**Figure 7R and Figure S21A**). We detected nascent proteins
397 labeled by puromycin within axonal spheroids, and treatment with the protein translation
398 inhibitor anisomycin reduced the amount of labeling (**Figure 7S and Figure S21A-C**), indicating
399 that local mRNA translation may occur within axonal spheroids. To examine whether mTOR
400 inhibition plays a role in regulating nascent protein production in spheroids, we performed both

401 pharmacological and genetic manipulations *in vivo.* We first used Torin1 to inhibit mTOR in 5XFAD
402 mice and observed that the puromycin signal remained unchanged. Additionally, we used mTOR-
403 floxed mice and a PHPeB-hSyn-Cre virus to genetically knock out mTOR in neurons. However,
404 neither the homozygous nor heterozygous mTOR knockouts had a significant effect on the
405 puromycin signal (**Figures 7A-C, Figures S19A-D, and Figures S21D-F**). These results indicate that
406 under our experimental conditions (**Figures S21D-F**), mTOR likely does not control local protein
407 translation within axonal spheroids.
408
409 Altogether, these experiments indicate that the reduction in axonal spheroid size and number
410 observed after mTOR inhibition is likely due to its enhancement of lysosomal biogenesis and
411 autophagy, rather than modulation of local protein translation in spheroids.

412 **DISCUSSION**
413
414 Plaque-associated axonal spheroids, also known as dystrophic neurites, have been recognized for
415 over a century [10] and are one of the most prevalent neuropathological hallmarks in AD [11, 14,
416 64, 65]. However, the molecular composition and cellular biology underlying the progression of
417 this pathology have not been systematically studied, primarily because of a lack of appropriate
418 methodologies. In this study, we implemented a comprehensive approach to investigate the
419 molecular and cellular mechanisms of PAAS formation. We developed a subcellular proximity
420 labeling proteomics approach in postmortem human and mouse brains [43], which allowed us to
421 uncover the molecular architecture of PAAS and other subcellular compartments. Through
422 bioinformatics analysis and high-resolution confocal imaging validation, we identified hundreds
423 of proteins and signaling pathways previously not known to be associated with PAAS, revealing
424 lipid transport, protein turnover and cytoskeletal dynamics as signature biological processes
425 associated with PAAS. Additionally, we found activation of the PI3K/AKT/mTOR signaling within
426 PAAS, a pathway known to be a master regulator of these biological processes. Overall, the
427 human PAAS proteomics provided a comprehensive view of the protein composition and
428 potential signaling pathways operating within axonal spheroids (**Figure 8, Figure S10 and Table**
429 **S2**). To investigate the functional implications of these findings on axonal spheroids pathogenesis
430 in humans, we utilized an optimized human iPSC-derived AD model [57] that faithfully replicates
431 amyloid plaque and PAAS formation. Both pharmacological and genetic inhibition of mTOR
432 signaling in this model and in AD-like mice resulted in a significant reduction in PAAS pathology.
433 This study, therefore, uncovers the molecular architecture and functional abnormalities of PAAS
434 in human neurons and implicates the PI3K/AKT/mTOR axis as a key signaling pathway in PAAS
435 formation and growth. Furthermore, it suggests a new potential strategy for mitigating axonal
436 pathology, independent of amyloid removal.
437
438 To uncover the PAAS proteome, we employed proximity labeling proteomics with subcellular
439 resolution, a technique that overcomes the lack of cellular and subcellular specificity of
440 conventional tissue proteomics, including micro-dissected amyloid plaques [66-68]. Using an
441 antibody-based biotinylation method [43, 44] to tag proteins in axonal spheroids, without
442 requiring overexpression of an exogenous peroxidase or biotin ligase [36, 37, 41], allowed us to
443 obtain comparative proteomes from widely available postmortem tissues. We selected PLD3 as
444 an antibody bait because this protein is highly enriched in PAAS of both humans and mice [47,
445 48] and is almost exclusively expressed in neurons [4, 47], thus minimizing the potential for
446 contamination from other cell types. Indeed, comparison between PLD3- and Lamp1-labeled
447 proteomes in 5XFAD mice showed that the PLD3-labeled proteome is much more specific for
448 neuronal and axonal structures (**Figure S11**).
449
450 Utilizing our proteomic strategy, we discovered a range of proteins previously unknown to be
451 enriched in PAAS, along with those already identified in these structures (**Figure 8**, **Figure S10,**
452 **Tables S1 and S2**). Our proteomics analysis in AD humans highlighted the activation of three key
453 signature biological processes that are likely involved in the formation and growth of PAAS
454 (**Figures 3 and 4**). These key signatures include: 1) Proteolysis Dysfunction: This was indicated by
455 the accumulation of proteins associated with endocytosis, phagosome, proteosome, ubiquitin-

456 mediated proteolysis, and lysosome acidification (**Figures 3, 5, 8 and Table S2**). Prior studies have
457 shown that protease-deficient lysosomes and autophagosomes within PAAS [14], and the
458 enlargement of these vesicles, mediates the overall increase in spheroid size [4], highlighting the
459 critical role of aberrant lysosomal function in spheroid formation and growth. 2) Cytoskeletal
460 Dysregulation: we found that PAAS were enriched with activated signaling pathways, such as
461 actin cytoskeletal signaling, RAC signaling and actin nucleation by the ARP-WASP complex.
462 Conversely, pathways like RHOGDI signaling, which has been shown to regulate Rho family
463 GTPase, were inhibited (**Figures 3C and S9E**) [69, 70]. This indicates that ongoing cytoskeletal
464 reorganization and plasticity within PAAS could be important events in the initial formation and
465 enlargement of these structures. Moreover, such cytoskeletal changes could impact both
466 retrograde and anterograde axonal cargo transport, leading to further accumulation of
467 endolysosomal vesicles [18, 28, 71], and the subsequent expansion of spheroids. 3) Lipid
468 Transport and Metabolism: our results indicate that lipid transport is highly activated in PAAS
469 (**Figures 4A-D**), and proteins involved in lipid transport and metabolisms, such as APOE, HDLBP
470 and C3, are highly expressed within axonal spheroids and aberrant axons around amyloid plaques
471 (**Figures 4B-G and Figure S15A**). Among these proteins, APOE is the most significant risk gene in
472 AD and is a lipid transporter [53]. TMEM30A, ATP8A1 and ATP8A2 (**Figures 4C and 4E**) compose
473 the P4-ATPase complex, which controls the asymmetric membrane lipid distribution, maintains
474 membrane stability and regulates vesicle-mediated protein transport [72]. The enrichment of
475 these proteins likely relates to the massive accumulation of endolysosomal vesicles within PAAS,
476 which must require active local lipid transport, synthesis and metabolism. This is in line with
477 previous findings that lipids participate in mediating axonal lysosome delivery and spheroid
478 formation [21]. Interestingly, complement C3, a crucial protein for activating the complement
479 system [73] that is also implicated in lipid metabolism [74, 75], exhibited the highest expression
480 in axonal spheroids and aberrant axons (**Figures 4E, 4F and Figure S15A**). This aligns with prior
481 research indicating the expression of complement proteins in dystrophic neurites around
482 compact amyloid plaques [76-78], and could suggest a connection between complement
483 pathway activation in the formation of axonal spheroids, potentially independent of
484 neuroimmune interactions. Importantly, based on our previous work showing that microglia do
485 not polarize toward spheroids and that spheroids are very long lasting [4, 31, 32], we suggest that
486 in this case, C3 is not likely to be playing a role in glial engulfment. The precise role of C3 within
487 spheroids will require additional investigation in the future.
488
489 The PI3K/AKT/mTOR axis emerged as a key activated signaling pathway within PAAS (**Figures 3C**
490 **and S9E**). Additionally, the activation of this pathway in human postmortem brains showed a
491 strong correlation with AD (**Figures 5B-C**). The PI3K/AKT/mTOR pathway is known for its
492 inhibitory effects on cell autophagy, endosome, autophagosome maturation [79], lysosomal
493 biogenesis and proteasome assembly [52], while simultaneously promoting axonal outgrowth
494 [62, 63, 80] and lipid synthesis [52, 81]. Interestingly, certain lipids like phosphatidic acid and
495 cholesterol have been shown to activate the mTORC1 complex [82, 83]. This suggests that lipids
496 present within PAAS could mediate the activation of mTOR signaling, which in turn may play a
497 role as a modulator of PAAS formation by regulating the three key biological processes that we
498 identified within PAAS (lipid transport, protein turnover and cytoskeletal dynamics) (**Figures 3**
499 **and 4**).

500
501 The pharmacological and genetic inhibition of mTOR signaling in our human iPSC-derived AD
502 model led to a marked reduction in PAAS pathology (**Figures 6 and 7**). Moreover, by using hSyn
503 promoter driven Cre viruses in vivo, we achieved neuron-specific mTOR heterozygous knockout
504 in 5XFAD mice, thereby avoiding potential confounding effects of mTOR manipulations in glial
505 cells. Investigation of downstream mechanisms revealed that mTOR knockdown enhanced
506 autophagy, which could operate at the whole cell level and locally at axonal spheroids,
507 considering the extensive accumulation of endolysosmal vesicles in these structures.
508 Furthermore, we noted the presence of mRNA and nascent proteins within axonal spheroids,
509 indicating a potential for local translation at these sites. Although mTOR signaling is known to
510 modulate local translation in neurons in various contexts [62, 63, 84], our study did not show
511 changes in local translation levels following mTOR knockout or pharmacological inhibition (**Figure**
512 **S21D-F**).
513
514 In addition to the PI3K/AKT/mTOR, we observed the activation of other signaling pathways within
515 PAAS, including calcium signaling and amyloid processing (**Figures 3C and 8**). Regarding calcium
516 homeostasis, proteins involved in calcium signaling like CAMK2 and calmodulin were identified
517 in PAAS (**Figures 3E and Table S2**), suggesting a significant role of local calcium signaling
518 dysregulation in PAAS pathogenesis. This is supported by our longitudinal calcium imaging in
519 human neurons, which demonstrated that axonal spheroids disrupt calcium rise and decay times
520 following electrical stimulation, indicating impaired action potential conduction and calcium
521 homeostasis within PAAS. Recent studies have shown that abnormal local calcium efflux from
522 deacidified late endosomes and amphisomes can affect axonal transport of these vesicles [85],
523 indicating a complex interaction between various signaling pathways during PAAS formation and
524 growth.
525
526 Our human iPSC-derived AD model successfully replicated PAAS pathology, characterized by
527 abundant spheroid formation around thioflavin S positive amyloid plaques and significant
528 accumulation of endolysosomal vesicles, cytoskeletal elements, and phosphorylated tau within
529 PAAS. The administration of exogenous β-amyloid in this model (**Figure 6A-D**) supports the
530 theory that spheroids are formed in response to extracellular amyloid deposition rather than
531 being the source of these deposits [18, 86]. Longitudinal imaging of individual axons in human
532 neurons showed rapid spheroid formation and lysosome accumulation within days after Aβ
533 administration. Additionally, axons showed active growth during spheroid formation, as opposed
534 to a dying-back pattern (**Figure 6C**), consistent with our previous *in vivo* observations in mice [4].
535 Despite widespread exposure to diffuse Aβ in this model, abundant axonal spheroids were only
536 observed next to compact thioflavin S positive deposits (**Figure 6B, Figures S16E-F and S18B-C**).
537 This is consistent with observations in humans showing that diffuse amyloid deposits (thioflavin
538 S negative) are not typically surrounded by PAAS, whereas thioflavin S positive deposits usually
539 have extensive PAAS pathology [31]. This strongly suggests that specific changes in β amyloid
540 conformation are critical for inducing PAAS formation. Applying Torin1 before amyloid plaque
541 treatment can answer whether mTOR inhibition has an effect on axonal spheroid initiation,
542 whereas applying Torin1 after amyloid plaque treatment and axonal spheroid formation can

543 answer whether mTOR inhibition has an effect on axonal spheroid maintenance, although
544 spheroids likely continue to form in a gradual way following amyloid administration.
545
546 There are several potential limitations of our study. First, while our STED super-resolution
547 imaging indicated that the radius of antibody-based proximity labeling in brain tissue is less than
548 50 nm, it is possible that some proteins that are distal to PLD3 were not identified in the PAAS
549 proteome. However, the high enrichment of PLD3 in axonal spheroids increases the likelihood of
550 protein biotinylation, as evidenced by our ability to capture most proteins previously described
551 in these structures, including not only endolysosomal-related proteins, but also cytoskeletal
552 proteins, such as SPTBN1, and proteins expressed on the cell surface, such as receptor NTRK2
553 (**Figures 2D, 8, Figure S9A, S10 and Table S2**). Second, although PLD3 is found in spheroids of
554 both AD humans and mice, some labeling does occur at neuronal cell bodies and neuropil (~27%
555 of PLD3 signal) (**Figures S2E-G**). We addressed this by eliminating proteins potentially derived
556 from neuronal cell bodies (**Figure 2B**, also see method section), but we cannot completely rule
557 out the presence of some neuronal cell body-specific proteins in the PAAS proteome. For
558 example, in theory if a protein is up-regulated in AD and expressed only in the neuronal soma but
559 not in PAAS, that could constitute a potential false positive in this dataset, although we have not
560 found such situation thus far. Third, the low number of plaques and axonal spheroids in early-
561 stage AD limited our ability to compare the levels of the various PAAS proteins at different stages
562 of disease progression due to limited protein yield. Future studies could employ emerging
563 techniques for multiplexed high-resolution quantitative imaging [87] for comparisons at different
564 disease stages. Fourth, the human iPSC-derived AD model recapitulates the formation of
565 spheroids around amyloid plaques, but it does so through a rapid process that may not fully
566 reflect the *in vivo* situation. Future models may need refining for a more chronic buildup of
567 amyloid deposits and potentially include co-culturing with other cell types like microglia to more
568 closely mimic the *in vivo* plaque microenvironment.
569
570 Altogether, the proteomics resources and methodologies we developed for analyzing axonal
571 pathology in human postmortem brains, iPSC-derived human neurons and *in vivo* open
572 opportunities for elucidating mechanisms controlling the initiation and progression of axonal
573 pathology, and for testing new therapeutic targets. While this study focused on axonal spheroids
574 associated with amyloid plaques, spheroids can be found in other neurodegenerative disorders
575 [21, 88-90]. Therefore, the multidisciplinary strategies established here will facilitate future
576 studies into the diverse cell biological processes governing axonal spheroid pathology in AD and
577 other neurodegenerative disorders. Ultimately, this will provide crucial insights into the role of
578 axonal pathology in neurodegeneration and neural circuit disruption, with significant therapeutic
579 implications.

580 **FIGURE AND FIGURE LEGEND**

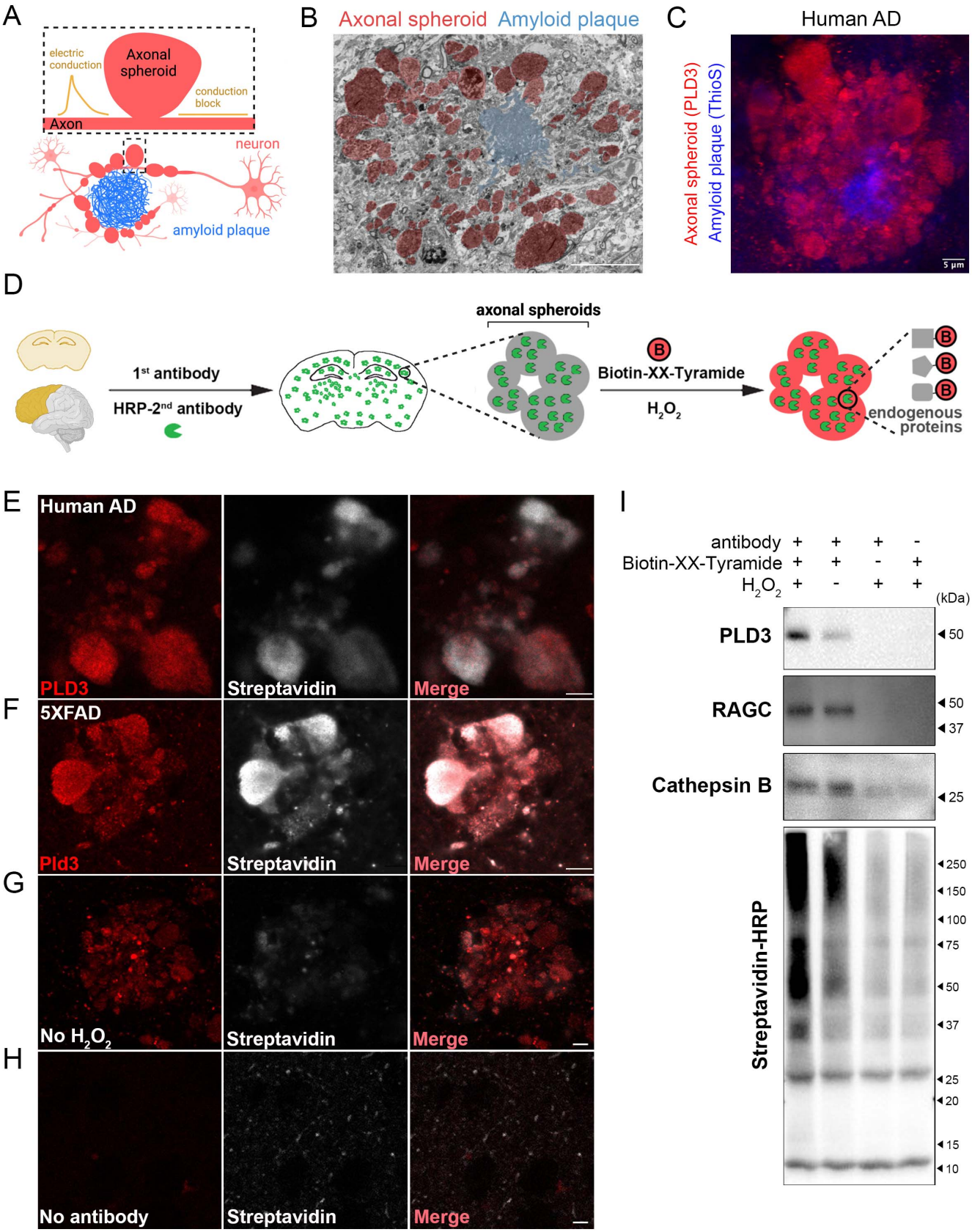

581 **Figure 1. Proximity labeling of proteins within plaque-associated axonal spheroids**

582 **A.** Schematic showing axons with spheroids (red) around an amyloid plaque (blue). Spheroids
583 cause electric conduction delay and blockage along axons [4]. **B.** A FIB-SEM image from a 5XFAD
584 mouse shows spheroids (red) around an amyloid plaque (blue). Scale bar = 20 µm. Related to
585 **Movie S1**. **C.** Immunofluorescence confocal deconvolved image shows that PLD3 is highly
586 enriched in axonal spheroids (red, PLD3) around amyloid plaques (blue, ThioflavinS) in
587 postmortem AD human brain. **D.** A schematic showing the pipeline for proximity labeling PAAS
588 proteomics in postmortem brains. Postmortem AD human or mouse brains were incubated with
589 primary antibody against PLD3 and HRP-conjugated secondary antibody, followed by
590 biotinylation reaction in the presence of Biotin-XX-Tyramide and hydrogen peroxide. **E-H.**
591 Proximity labeling biotinylation of proteins within PAAS in **(E)** human AD and **(F)** 5XFAD mouse
592 brains. **(E-F)** Biotinylated proteins were revealed by streptavidin-Alexa fluor 647. **(G-H)** Control
593 conditions including **(G)** no H_2O_2 or **(H)** no-antibody labeling markedly reduced biotinylation.
594 Scale bar = 5 µm. **I.** Streptavidin-HRP western blot demonstrates efficient streptavidin bead pull-
595 down of biotinylated proteins, including the protein bait PLD3, and the known axonal spheroid
596 proteins RAGC and Cathepsin B. See also **Figures S1-S4**.

A

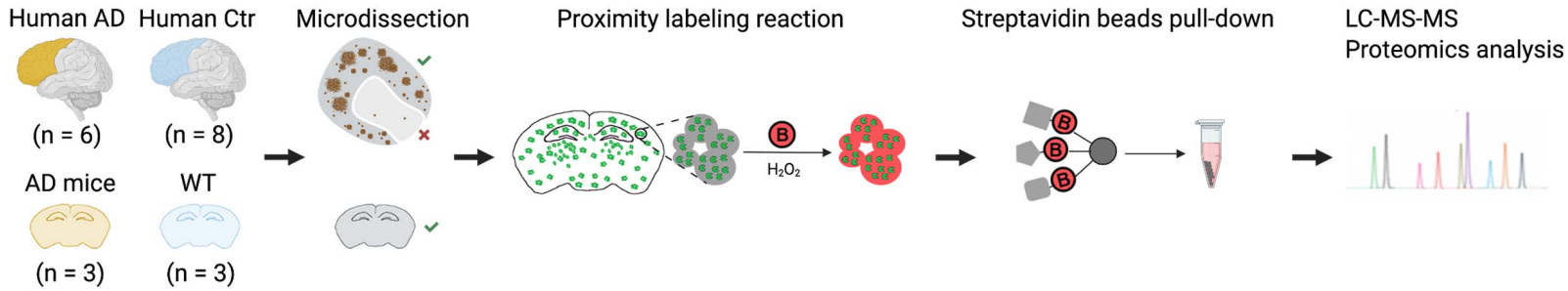

B

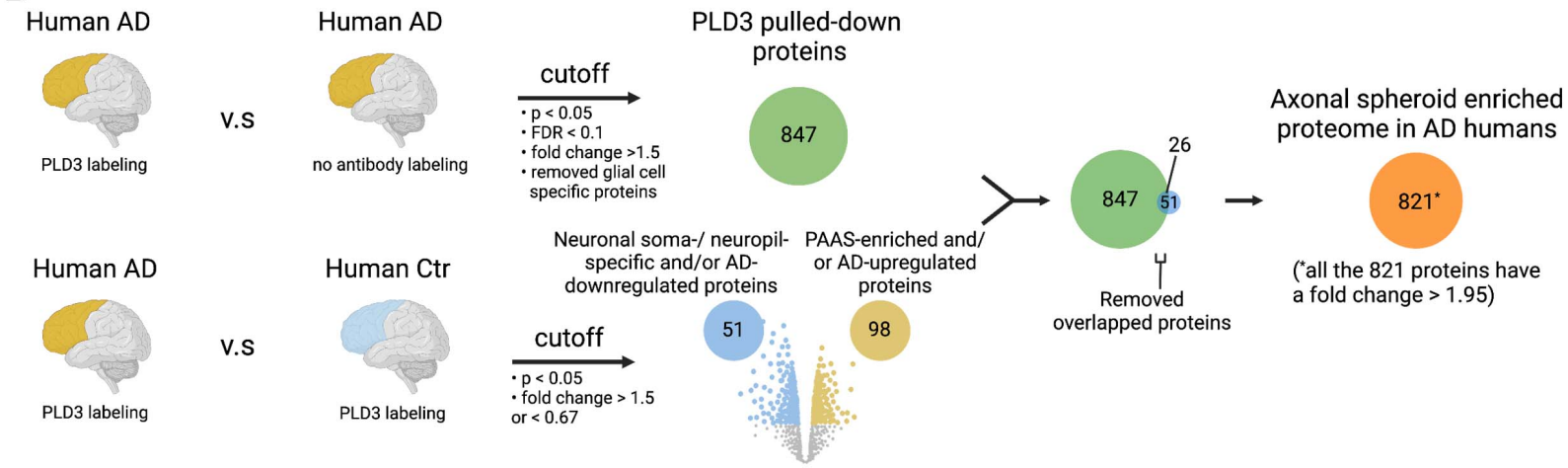

C

	5XFAD mice	AD humans
Protein detected	2371	2360
	PLD3 labeled v.s no antibody labeled	
Cutoff	p < 0.05, FDR < 10%, fold change >1.5	
Post-cutoff	922	849
	removed glial cell specific proteins	
Neuronal expressed	917	847
	removed non-specific proteins from neuronal soma and neuropil	
Axonal spheroid proteome	856	821

D

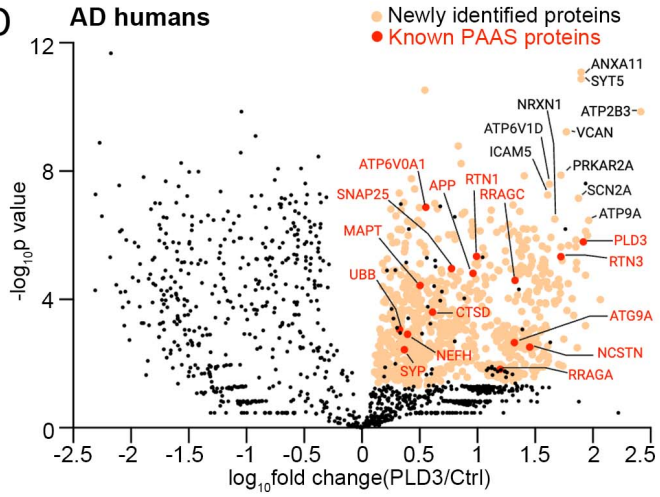

Figure 2. Proteomic analysis of plaque-associated axonal spheroids in AD humans and 5XFAD mice

A. Schematic showing the technical pipeline of PAAS proteomic analysis. The grey matter regions with high plaque load were microdissected out from human AD brain sections under guidance of a fluorescent stereomicroscope. Similarly, the grey matter regions were dissected from unaffected control brain sections. **B.** Statistical pipeline for revealing PAAS proteomes in humans

604 (related to **Figure 2C and Figure S2E-G**). The same pipeline was applied to uncover PAAS
605 proteomes in 5XFAD mice. **C.** Table showing the statistical cutoffs and summary of identified
606 proteomic hits in AD humans and 5XFAD mice. The final PAAS proteome in humans contains 821
607 proteins (all of them have a fold change > 1.95), and the final PAAS proteome in mice contains
608 856 proteins (all of them have a fold change > 1.66). **D.** Volcano plot show proteins that passed
609 the statistical cutoffs (orange dots) in AD humans. The top 10 proteomic hits with the lowest p-
610 value and highest fold changes are indicated by their gene names in black. Selected known PAAS
611 proteins are labeled as red dots, with their gene names in red. The black dots among the yellow
612 ones represent proteins filtered out by the statistical pipeline (**Figure 2B**). (See **Table S1** for full
613 list of proteomic hits). See also **Figures S5-S13**.

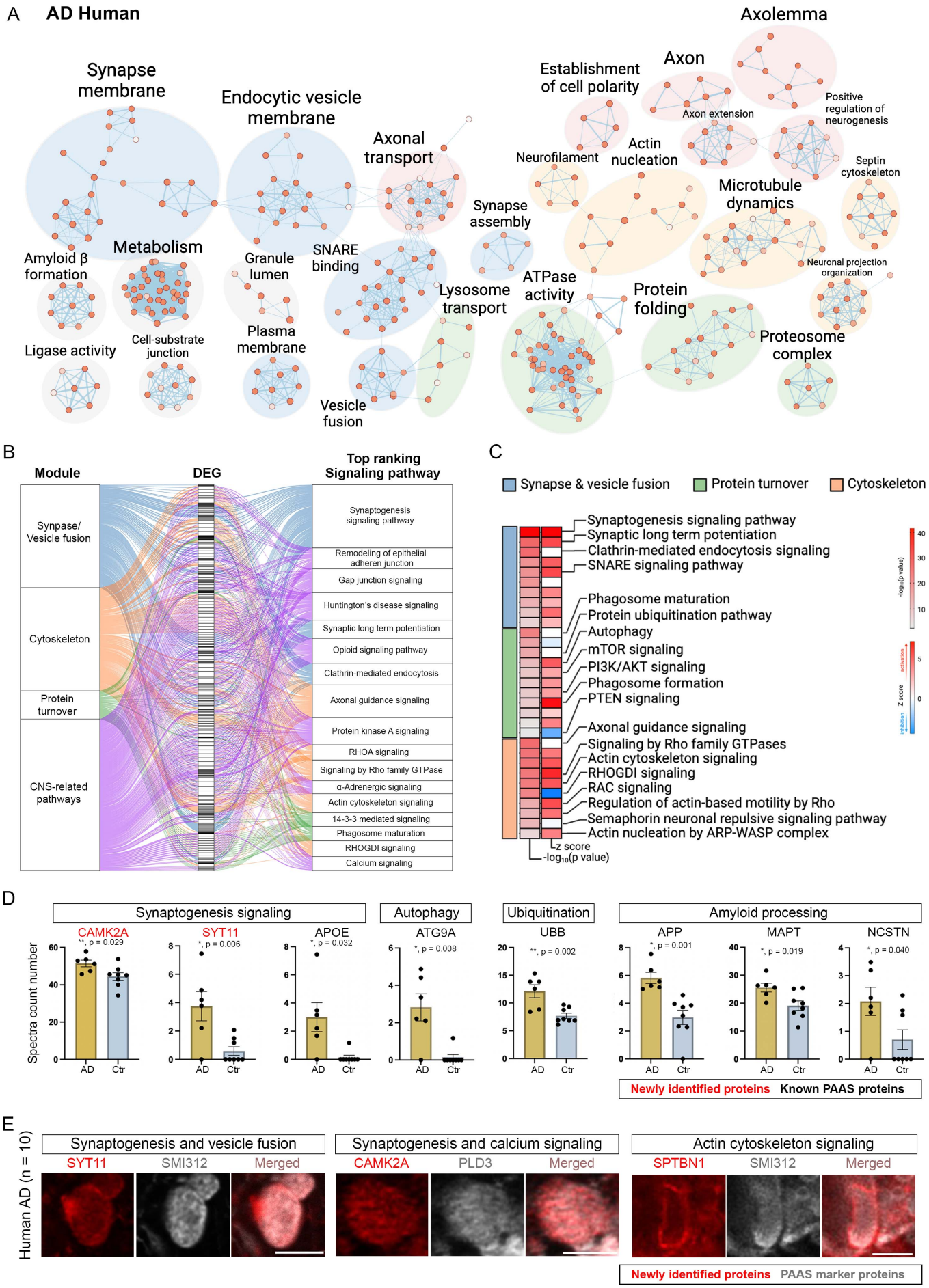

A
AD Human
Synapse membrane
Endocytic vesicle membrane
Axonal transport
Establishment of cell polarity
Axon
Axolemma
Axon extension
Positive regulation of neurogenesis
Neurofilament
Actin nucleation
Septin cytoskeleton
Microtubule dynamics
Synapse assembly
Amyloid β formation
Metabolism
Granule lumen
SNARE binding
Lysosome transport
ATPase activity
Protein folding
Neuronal projection organization
Ligase activity
Cell-substrate junction
Plasma membrane
Vesicle fusion
Proteosome complex
B
Module
DEG
Top ranking Signaling pathway
Synpase/ Vesicle fusion
Cytoskeleton
Protein turnover
CNS-related pathways
Synaptogenesis signaling pathway
Remodeling of epithelial adheren junction
Gap junction signaling
Huntington's disease signaling
Synaptic long term potentiation
Opioid signaling pathway
Clathrin-mediated endocytosis
Axonal guidance signaling
Protein kinase A signaling
RHOA signaling
Signaling by Rho family GTPase
α-Adrenergic signaling
Actin cytoskeleton signaling
14-3-3 mediated signaling
Phagosome maturation
RHOGDI signaling
Calcium signaling
C
Synapse & vesicle fusion
Protein turnover
Cytoskeleton
Synaptogenesis signaling pathway
Synaptic long term potentiation
Clathrin-mediated endocytosis signaling
SNARE signaling pathway
Phagosome maturation
Protein ubiquitination pathway
Autophagy
mTOR signaling
PI3K/AKT signaling
Phagosome formation
PTEN signaling
Axonal guidance signaling
Signaling by Rho family GTPases
Actin cytoskeleton signaling
RHOGDI signaling
RAC signaling
Regulation of actin-based motility by Rho
Semaphorin neuronal repulsive signaling pathway
Actin nucleation by ARP-WASP complex
z score
-log10(p value)
D
Synaptogenesis signaling
Autophagy
Ubiquitination
Amyloid processing
CAMK2A
SYT11
APOE
ATG9A
UBB
APP
MAPT
NCSTN
Spectra count number
AD
Ctr
Newly identified proteins
Known PAAS proteins
E
Human AD (n = 10)
Synaptogenesis and vesicle fusion
Synaptogenesis and calcium signaling
Actin cytoskeleton signaling
SYT11
SMI312
Merged
CAMK2A
PLD3
Merged
SPTBN1
SMI312
Merged
Newly identified proteins
PAAS marker proteins

615 **Figure 3. Pathway enrichment and signaling pathway analyses reveal that proteins related to**
616 **protein turnover and the cytoskeleton are key components of PAAS**

617 **A.** Pathway enrichment analysis of PAAS proteome in AD human brains. The Enrichment Map
618 represents a network of pathways where edges connect pathways with many shared genes. Node
619 color reflects the FDR of each pathway. The theme labels were curated based on the main
620 pathways of each subnetwork. Subnetworks with a minimum of four pathways connected by
621 edges are shown. **B**. IPA pathway analysis of the PAAS proteome in AD humans. Top ranking CNS-
622 related signaling pathways are shown. The signaling pathways are summarized as four modules.
623 The alluvium plot shows different color-coded modules connect to the differentially expressed
624 genes (DEGs) and the DEGs connects to the pathways that they are involved. **C.** IPA pathways
625 related to the three modules (synapse/vesicle fusion, protein turnover and cytoskeleton) with p-
626 values less than 0.01 are listed. Heatmaps indicate either the $-\log_{10}$ (p-value) or the z score of
627 each signaling pathway (pathways with a z score in red are predicted to be activated while blue
628 ones are predicted to be inhibited). **D.** Bar chart shows representative proteomic hits from the
629 signaling pathways in (**C**). The newly identified proteins are labeled in red, and the known PAAS
630 proteins are labeled in black. n = 6 Human AD, and n = 8 unaffected human control brains were
631 utilized. Error bars indicate SEM. **E.** Representative immunofluorescence confocal images of
632 newly identified proteins (red) expressed in spheroids (grey) in AD postmortem brains. Scale bar
633 = 5 µm. Zoom-out images are shown in **Figure S14**. Quantification was performed in n = 10 AD
634 human brains. Protein expression quantifications can be found in **Table S2**. See also **Figures S9**
635 **and S14.**

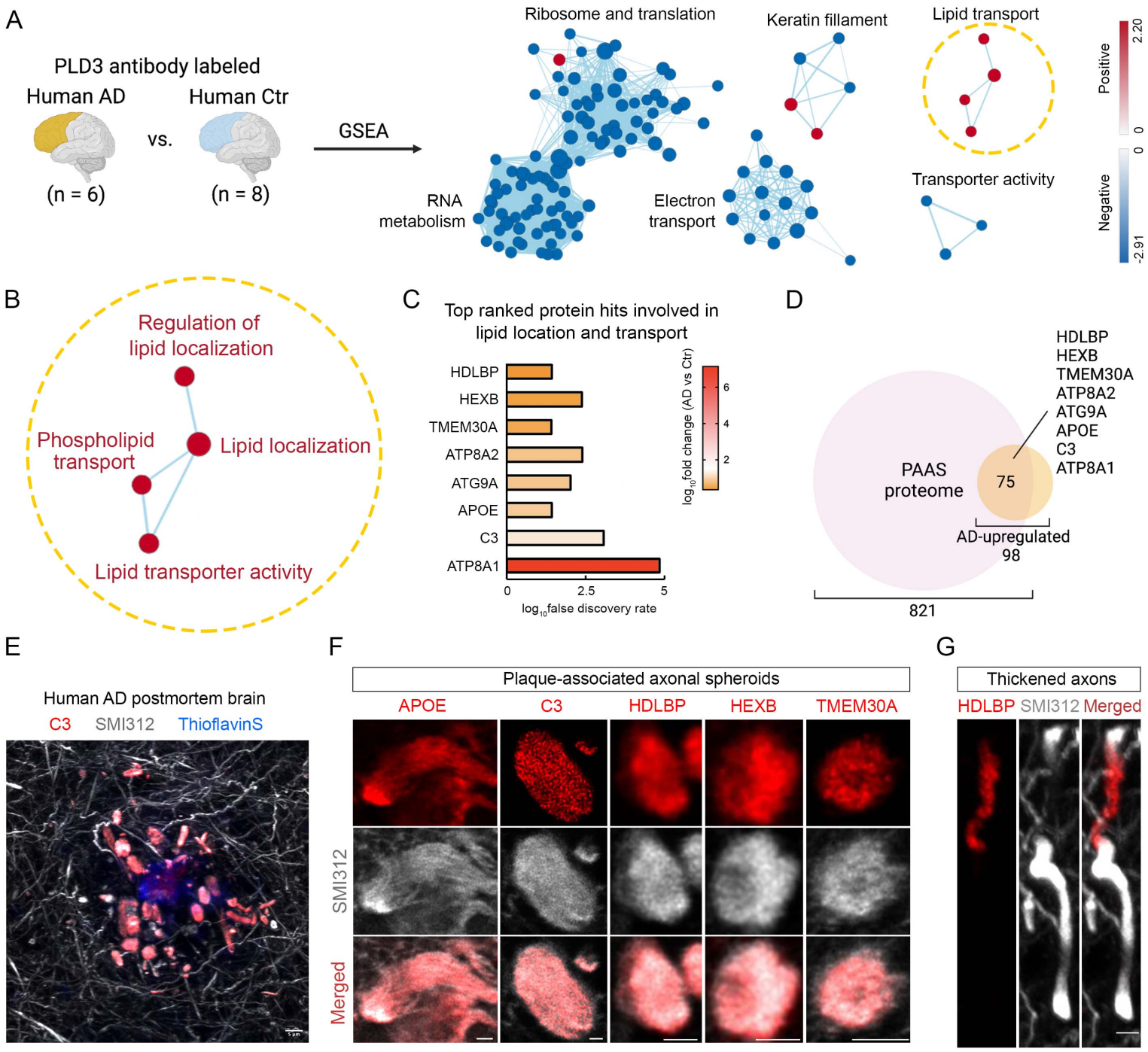
A
PLD3 antibody labeled
Human AD
Human Ctr
vs.
(n = 6)
(n = 8)
GSEA
Ribosome and translation
Keratin fillament
Lipid transport
RNA metabolism
Electron transport
Transporter activity
Positive
Negative
2.20
0
0
-2.91
B
Regulation of lipid localization
Phospholipid transport
Lipid localization
Lipid transporter activity
C
Top ranked protein hits involved in lipid location and transport
HDLBP
HEXB
TMEM30A
ATP8A2
ATG9A
APOE
C3
ATP8A1
0
2.5
5
log10false discovery rate
log10fold change (AD vs Ctr)
6
4
2
D
HDLBP
HEXB
TMEM30A
ATP8A2
ATG9A
APOE
C3
ATP8A1
PAAS proteome
75
AD-upregulated
98
821
E
Human AD postmortem brain
C3
SMI312
ThioflavinS
F
Plaque-associated axonal spheroids
APOE
C3
HDLBP
HEXB
TMEM30A
SMI312
Merged
G
Thickened axons
HDLBP
SMI312
Merged

636

637 **Figure 4. Proteins involved in lipid transport are upregulated in PAAS**

638 **A.** Gene set enrichment analysis (GSEA) was performed to compare PLD3-labeled proteins
639 between AD humans and unaffected controls. Pathway enrichment analysis was performed to
640 cluster GSEA nodes. Each node represents a biological process or cellular component. The name
641 of each cluster was curated based on the main GSEA biological processes and cellular
642 components within each cluster. See also **Table S6**. **B.** Detailed information on the lipid transport
643 cluster. The biological process or cellular component of each node is listed. **C.** The 8 top-ranked
644 proteomic hits involved in the lipid transport cluster. The bar chart shows the fold change and
645 FDR of these hits by comparing PLD3-labeled AD humans versus unaffected control humans. **D.**
646 Venn diagram shows that the 8 top-ranked lipid transport-related proteins are shared between
647 the human PAAS proteomes (821 proteins) and the AD-upregulated proteins (98 proteins). There
648 are 75 proteins shared between these two datasets. **E-F.** Representative (**E**) zoomed-out and (**F**)
649 zoomed-in immunofluorescence confocal images of the top-ranked lipid-related proteomic hits
650 in AD human brain, including C3, APOE, HDLBP, HEXB and TMEM30A. Scale bar = 5 µm. Zoomed-
651 out images of all the proteins are shown in **Figure S15**. Quantification was performed in n = 3 AD
652 human brains. Protein expression quantifications can be found in **Table S2**. **G.** Representative
653 immunofluorescence confocal images show the anti-colocalized distribution of HDLBP (red) and
654 the pan-axonal marker SMI312 (grey) within thickened axons in the AD human postmortem brain
655 (n = 3). Scale bar = 5 µm.

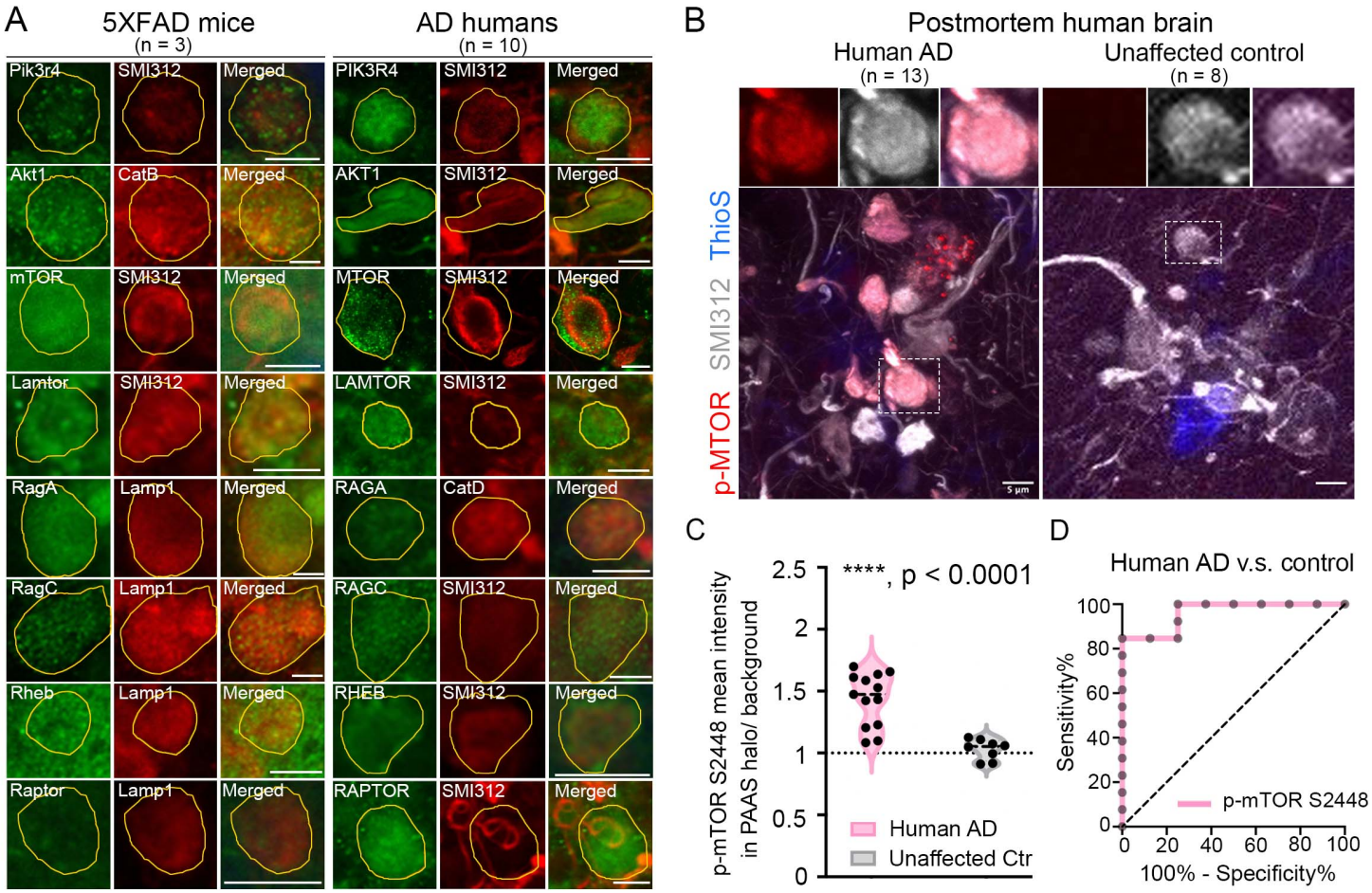

Figure 5. mTOR signaling is expressed in axonal spheroids and is associated with Alzheimer's pathology

A. Immunofluorescence confocal imaging validation of selected proteomic hits and the related proteins in the PI3K/AKT/mTOR axis, revealing that signaling molecules of the PI3K/AKT/mTOR axis are expressed in PAAS in both AD humans and 5XFAD mice. PAAS were labeled using traditional markers including neurofilament SMI312, Cathepsin B (CatB), Cathepsin D (CatD), or Lamp1. PAAS are outlined in yellow. Scale bar = 5 µm. Protein expression quantification results can be found in **Table S2**. **B.** Phosphorylated-mTOR-S2448 (red) is highly enriched within PAAS (grey, SMI312) around amyloid plaques (blue, ThioflavinS) in severe AD. Scale bar = 5 µm. **C.** Quantification of the mean fluorescence intensity levels of p-mTOR-S2448 within axonal spheroid halos normalized to background fluorescence, comparing human AD (n = 13 brains) versus unaffected controls (n = 8 brains). Unpaired t-test (Mann Whitney test), two-tailed, ****, $p < 0.0001$. The Black dashed line indicates the median. **D.** A Receiver Operating Characteristic (ROC) curve shows that the p-mTOR-S2448 level in PAAS significantly separates AD brains from those of unaffected controls. The area under the ROC curve = 0.962, standard error = 0.038, 95% confidence interval = 0.888 to 1.000, p-value = 0.0005.

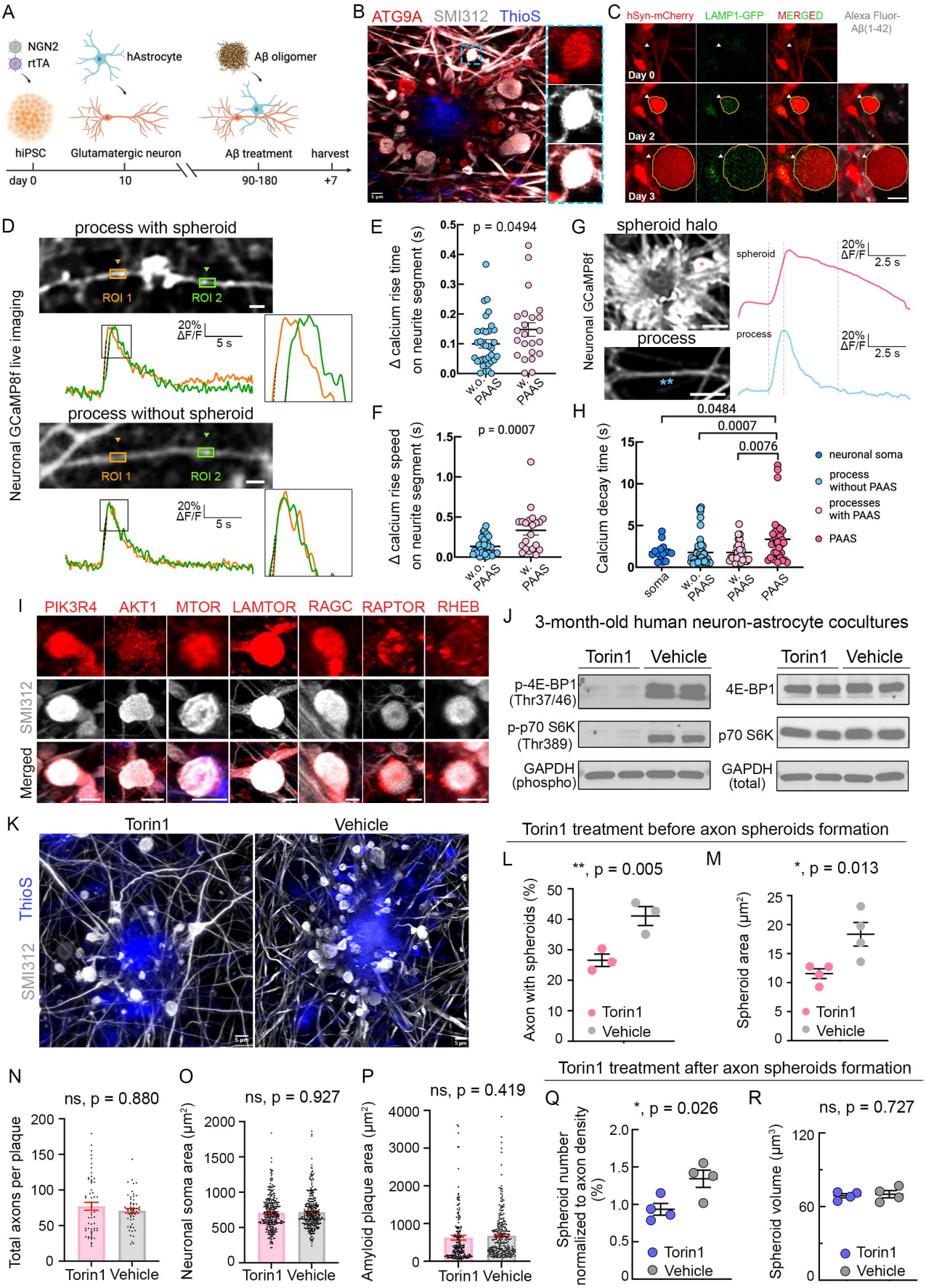
A
NGN2
rtTA
hAstrocyte
Aβ oligomer
hiPSC
Glutamatergic neuron
Aβ treatment
harvest
day 0
10
90-180
+7
B
ATG9A SMI312 ThioS
C
hSyn-mCherry
LAMP1-GFP
MERGED
Alexa Fluor-Aβ(1-42)
Day 0
Day 2
Day 3
D
process with spheroid
ROI 1
ROI 2
20% ΔF/F
5 s
process without spheroid
Neuronal GCaMP8f live imaging
E
p = 0.0494
Δ calcium rise time on neurite segment (s)
w.o. PAAS
w. PAAS
F
p = 0.0007
Δ calcium rise speed on neurite segment (s)
G
spheroid halo
spheroid
process
2.5 s
H
0.0484
0.0007
0.0076
Calcium decay time (s)
soma
neuronal soma
process without PAAS
processes with PAAS
PAAS
I
PIK3R4
AKT1
MTOR
LAMTOR
RAGC
RAPTOR
RHEB
SMI312
Merged
J
3-month-old human neuron-astrocyte cocultures
Torin1
Vehicle
p-4E-BP1 (Thr37/46)
4E-BP1
p-p70 S6K (Thr389)
p70 S6K
GAPDH (phospho)
GAPDH (total)
K
Torin1
Vehicle
ThioS
SMI312
Torin1 treatment before axon spheroids formation
L
**, p = 0.005
Axon with spheroids (%)
M
*, p = 0.013
Spheroid area (μm²)
N
ns, p = 0.880
Total axons per plaque
O
ns, p = 0.927
Neuronal soma area (μm²)
P
ns, p = 0.419
Amyloid plaque area (μm²)
Torin1 treatment after axon spheroids formation
Q
*, p = 0.026
Spheroid number normalized to axon density (%)
R
ns, p = 0.727
Spheroid volume (μm³)

673 **Figure 6. A human iPSC-derived AD model demonstrates that mTOR signaling inhibition reduces**
674 **PAAS pathology**

675 **A.** The workflow shows the generation of a human iPSC-derived neuron and astrocyte co-culture
676 AD model to recapitulate axonal spheroid pathology around amyloid plaques. Human iPSCs
677 (hiPSCs) are plated at day 0 to generate *NGN2*-induced glutamatergic human neurons. Human
678 primary astrocytes (hAstrocytes) are seeded at day 10, followed by 3 to 6 months of co-culture.
679 Oligomerized Aβ 1-42 peptides are administered for 7 days to the neuron-glia co-culture. **B.**
680 Confocal deconvolved image shows the robust formation of axonal spheroids (grey, SMI312) in
681 human neurons around amyloid deposits (blue, ThioflavinS). These spheroids expressed the
682 axonal cytoskeleton marker SMI312 (grey) and autophagosome marker ATG9A (red), resembling
683 PAAS in postmortem AD brains. **C.** Time-lapse imaging of human neurons shows the formation
684 of a spheroid (arrowhead) from a neurite (red, AAV9-hSyn-mCherry labeled). Lysosomes (green,
685 AAV2-CMV-LAMP1-GFP labeled) accumulate within spheroids. Spheroids (arrowhead) near Aβ
686 deposits (grey) enlarged over time. **D-H.** Neuronal GCaMP8f imaging in human iPSC AD model.
687 **(D)** Representative images showing CAMKII-GCaMP8f labeled neuronal processes with (upper
688 panel) or without (lower panel) axonal spheroids. Representative traces showing calcium
689 dynamics recorded from neuronal processes segments in the human iPSC AD model. The y axis
690 indicates the normalized ΔF/F of calcium transients. The dotted black lines indicates the calcium
691 rise slope. **(E)** Quantification of calcium rise time and **(F)** calcium rise speed. Each dot represents
692 a neuronal process from three independent experiments. Unpaired two-tailed Mann Whitney t
693 test was performed. **(G)** Representative images showing CAMKII-GCaMP8f signal from axonal
694 spheroid halo or neuronal processes. Representative traces showing that calcium decay time is
695 much slower in spheroids (pink asterisk) than in neuronal processes (blue asterisks). The y axis
696 indicates the normalized ΔF/F of calcium transients. **(H)** Quantification showing calcium decay
697 time in neuronal soma (blue), neuronal processes without spheroids (light blue), neuronal
698 processes with spheroids (light pink) and spheroids (pink). Each dot represents a neuronal
699 process from three independent experiments. One-way ANOVA was performed to compare
700 groups. **I.** mTOR signaling molecules (red) are expressed in hiPSC-derived axonal spheroids (grey,
701 SMI312). Large-field-of-view images are shown in **Figure S17**. **J.** Western blot showing that Torin1
702 treatment markedly inhibited mTOR signaling, as revealed by the significant reduction of mTOR
703 downstream effectors phosphorylated 4E-BP1 and phosphorylated p70 S6K, while their total
704 protein level remained unchanged. **K-R.** Torin1 treatment reduced axonal spheroid pathology in
705 iPSC-derived human neurons. **(K)** Immunofluorescence confocal deconvolved images show that
706 Torin1 reduced axonal spheroids (grey, SMI312) around Aβ deposits (blue, ThioflavinS). **(L-P)**
707 Torin1 treatment before amyloid plaque and spheroid formation. **(L)** Quantification of the
708 percentage of axons with spheroids relative to the total number of axons around Aβ deposits.
709 Torin group and vehicle groups (n = 3 independent experiments for each group). Paired t-test,
710 two-tailed, **, p = 0.005. **(L)** Quantitative analysis of axonal spheroid size. Paired t-test, two-
711 tailed, *, p = 0.013. Torin and vehicle groups (n = 4 independent experiments for each group). (**J-**
712 **K**) Each dot represents an experiment in which 20 to 30 ROIs around plaques were quantified. **(N)**
713 Quantification of axon number around an amyloid plaque in each ROI (represented by black dots).
714 ROIs were quantified for Torin1 and vehicle treatment groups, n = 56 and n = 55, respectively.
715 Unpaired t-test, two-tailed, p = 0.880. **(O)** Quantification of neuronal soma size (related to **Figure**
716 **S15I**). Each dot represents an individual neuronal soma. Torin1 treatment group n = 298, vehicle

717 group n = 316. Unpaired t-test, two-tailed, p = 0.927. **(P)** Quantification of amyloid plaque size.
718 Each dot represents an amyloid plaque. Torin1 treatment group n = 201, vehicle group n = 253.
719 Unpaired t-test, two-tailed, p = 0.419. **(Q-R)** Torin treatment after amyloid plaque and spheroid
720 formation, related to **Figure S18**. Quantification of (Q) spheroid number normalized to axon
721 density and (R) spheroid size. Unpaired Mann Whitney t-test, two-tailed was performed. Torin
722 and vehicle groups (n = 4 independent experiments for each group). **(A-R**) All experiments were
723 validated independently at least three times using cultures derived from two independent hiPSC
724 lines. Scale bar = 5 µm, except scale bar = 5 µm in panel G. See also **Figures S16-S18**.

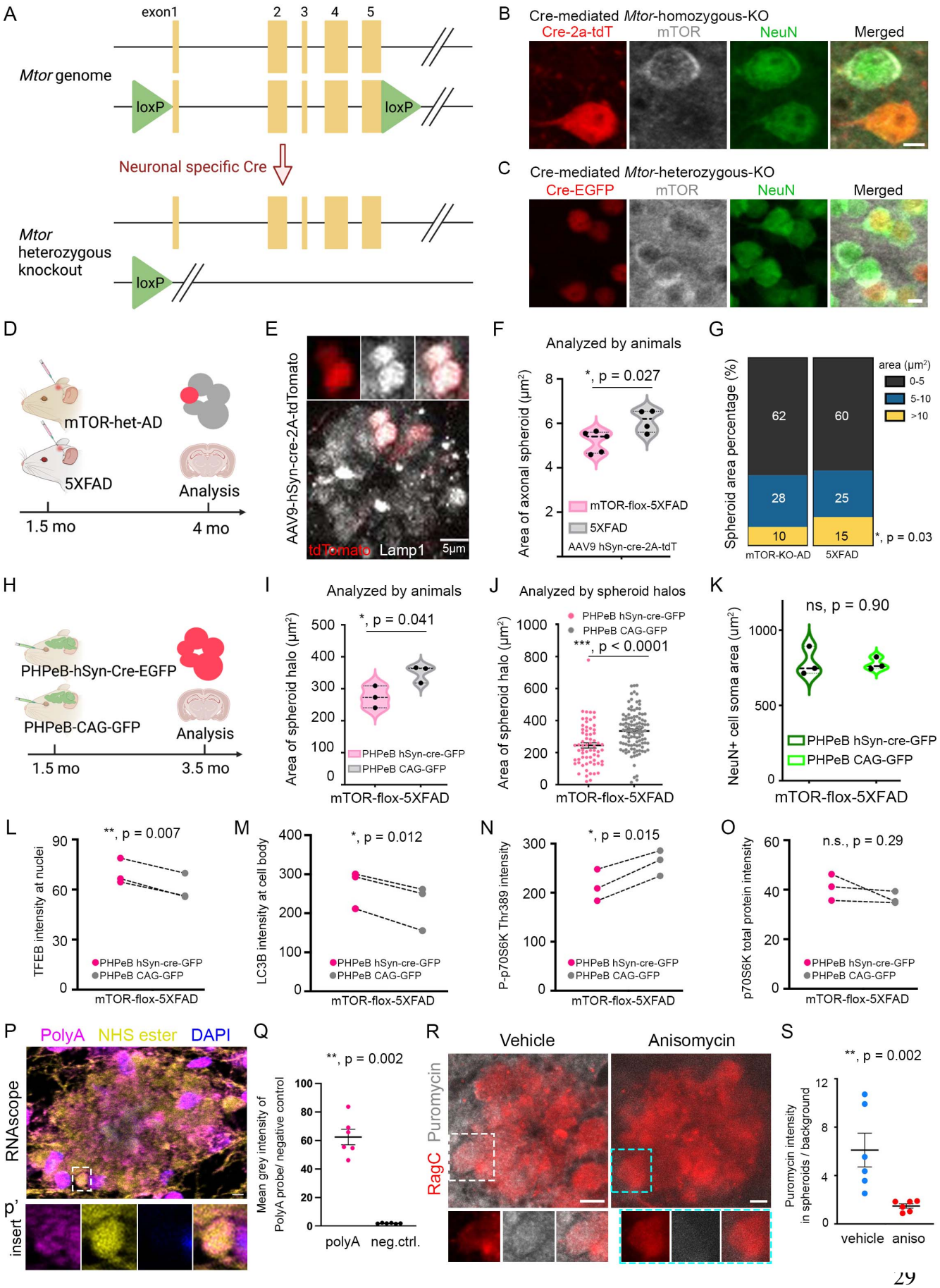
A
exon1
2
3
4
5
Mtor genome
loxP
loxP
Neuronal specific Cre
Mtor heterozygous knockout
loxP
B
Cre-mediated Mtor-homozygous-KO
Cre-2a-tdT
mTOR
NeuN
Merged
C
Cre-mediated Mtor-heterozygous-KO
Cre-EGFP
mTOR
NeuN
Merged
D
mTOR-het-AD
5XFAD
Analysis
1.5 mo
4 mo
E
AAV9-hSyn-cre-2A-tdTomato
tdTomato
Lamp1
5μm
F
Analyzed by animals
*, p = 0.027
Area of axonal spheroid (μm²)
mTOR-flox-5XFAD
5XFAD
AAV9 hSyn-cre-2A-tdT
G
Spheroid area percentage (%)
area (μm²)
0-5
5-10
>10
62
60
28
25
10
15
*, p = 0.03
mTOR-KO-AD
5XFAD
H
PHPeB-hSyn-Cre-EGFP
PHPeB-CAG-GFP
Analysis
1.5 mo
3.5 mo
I
Analyzed by animals
*, p = 0.041
Area of spheroid halo (μm²)
PHPeB hSyn-cre-GFP
PHPeB CAG-GFP
mTOR-flox-5XFAD
J
Analyzed by spheroid halos
PHPeB hSyn-cre-GFP
PHPeB CAG-GFP
***, p < 0.0001
Area of spheroid halo (μm²)
mTOR-flox-5XFAD
K
ns, p = 0.90
NeuN+ cell soma area (μm²)
PHPeB hSyn-cre-GFP
PHPeB CAG-GFP
mTOR-flox-5XFAD
L
**, p = 0.007
TFEB intensity at nuclei
PHPeB hSyn-cre-GFP
PHPeB CAG-GFP
mTOR-flox-5XFAD
M
*, p = 0.012
LC3B intensity at cell body
PHPeB hSyn-cre-GFP
PHPeB CAG-GFP
mTOR-flox-5XFAD
N
*, p = 0.015
P-p70S6K Thr389 intensity
PHPeB hSyn-cre-GFP
PHPeB CAG-GFP
mTOR-flox-5XFAD
O
n.s., p = 0.29
p70S6K total protein intensity
PHPeB hSyn-cre-GFP
PHPeB CAG-GFP
mTOR-flox-5XFAD
P
PolyA
NHS ester
DAPI
RNAscope
p'
insert
Q
**, p = 0.002
Mean grey intensity of PolyA probe/ negative control
polyA
neg.ctrl.
R
Vehicle
Anisomycin
Puromycin
RagC
S
**, p = 0.002
Puromycin intensity in spheroids / background
vehicle
aniso

726 **Figure 7. mTOR signaling inhibition reduces axonal spheroid pathology *in vivo***
727 **A.** Schematic of neuronal-specific conditional knockout of *Mtor* in the heterozygous floxed mouse.
728 **B-C.** Immunofluorescence confocal images showing neuronal specific Cre-mediated *Mtor*
729 homozygous knockout **(B)**, and heterozygous knockout **(C)** in *Mtor*-floxed mice using AAV9-hSyn-
730 Cre-2A-tdTomato, or AAV PHPeB-hSyn-Cre-EGFP, respectively. (**B**) mTOR expression (grey) was
731 absent in Cre-expressing neurons (red), compared to the adjacent neuron (green, NeuN) without
732 Cre expression. (**C**) mTOR expression (red) was reduced in Cre-expressing neurons (green),
733 compared to other neurons (grey, NeuN) without Cre expression. Scale bar 5 µm. **D.** Experimental
734 design of virally mediated genetic manipulation to study the impact of *Mtor* heterozygous
735 knockout on individual axonal spheroids in heterozygous *Mtor*-floxed-5XFAD mice**. E.**
736 Immunofluorescence confocal images showing AAV9-hSyn-Cre-2A-tdTomato sparsely labeling
737 individual axonal spheroids (red) within a spheroid halo (Lamp, grey). **F.** Quantification showing
738 that AAV9-mediated *Mtor* heterozygous knockout in heterozygous *Mtor*-flox-5XFAD mice
739 significantly reduced the size of individual axonal spheroids. Each dot represents an animal (n =
740 5 in each group). Unpaired t-test, two-tailed, *, p = 0.027. **G.** Using the same results in (**F**),
741 quantification analysis shows that *Mtor* heterozygous knockout significantly reduced the
742 percentage of larger axonal spheroids (area greater than 10 μm^2). Unpaired t-test, two-tailed, *,
743 p = 0.03. **H.** Experimental design of virally mediated genetic manipulation to study the impact of
744 *Mtor* heterozygous knockout on the size of the axonal spheroid halo in heterozygous *Mtor*-
745 floxed-5XFAD mice. **I.** Quantification showing that AAV.PHPeB-mediated *Mtor* heterozygous
746 knockout in *Mtor*-flox-5XFAD mice significantly reduced the size of axonal spheroid halos. Each
747 dot represents an animal (n = 3 in each group). Unpaired t-test, two-tailed, *, p = 0.041. **J.** Using
748 the same results as in (**I**) and quantified by the axonal spheroid halo. Each dot represents an
749 axonal spheroid halo. Knockout group n = 66 and control group n = 109 halos. Unpaired t-test,
750 two-tailed, ****, p < 0.0001. **K.** AAV PHPeB-hSyn-Cre-EGFP mediated *Mtor* heterozygous
751 knockout did not alter neuronal soma size. Each dot represents an animal (n = 3 in each group).
752 Unpaired t-test, two-tailed, p = 0.90. **L-O.** Investigation of mTOR heterozygous knockout
753 downstream signaling effectors in mTOR-floxed-5XFAD mice, comparing mice injected with
754 PHPeB-hSyn-cre-GFP viruses, with those injected with control viruses PHPeB-CAG-GFP.
755 Immunofluorescence intensity of (**L**) TFEB was measured in neuronal nuclei, and (**M**) LC3B, (**N**) P-
756 p70S6K Thr389, (**O**) p70S6K were measured in neuronal soma in an automated fashion. The
757 littermates and sex were paired as indicated by the paired points in (L-O), paired T-test was
758 performed. Each dot represents an animal (n = 3 in each group). **P.** RNAscope in 5XFAD mice
759 cortices showing that mRNA species (PolyA probe labeled, magenta) are expressed in axonal
760 spheroids (NHS ester labeled, yellow and DAPI negative). NHS ester (yellow) labels the axonal
761 spheroid halo, as well as the extracellular amyloid plaques. Nuclei are labeled with DAPI (blue).
762 Scale bar = 5 µm. **Q.** Quantification showing fluorescence intensity of PolyA probe compared to
763 that of negative control probe in axonal spheroids in 5XFAD mice cortices. Each dot represents
764 a large field of view (FOV), two FOVs are shown in each animal (n = 3 in each group). Unpaired t-
765 test, two-tailed, p = 0.002. **R.** Puromycylation in 5XFAD mice cortices showing nascent peptides
766 (puromycin labeled, grey) in axonal spheroids (RagC labeled, red). Puromycin labeling was
767 significantly reduced with the treatment of translation inhibitor anisomycin. Scale bar = 5 µm. **S.**
768 Quantification of puromycin fluorescence intensity in axonal spheroids, comparing vehicle versus

anisomycin control. Each dot represents a large field of view (FOV), two FOVs are shown in each animal (n = 3 in each group). Unpaired t-test, two-tailed, p = 0.002. See also **Figures S19-S21**.

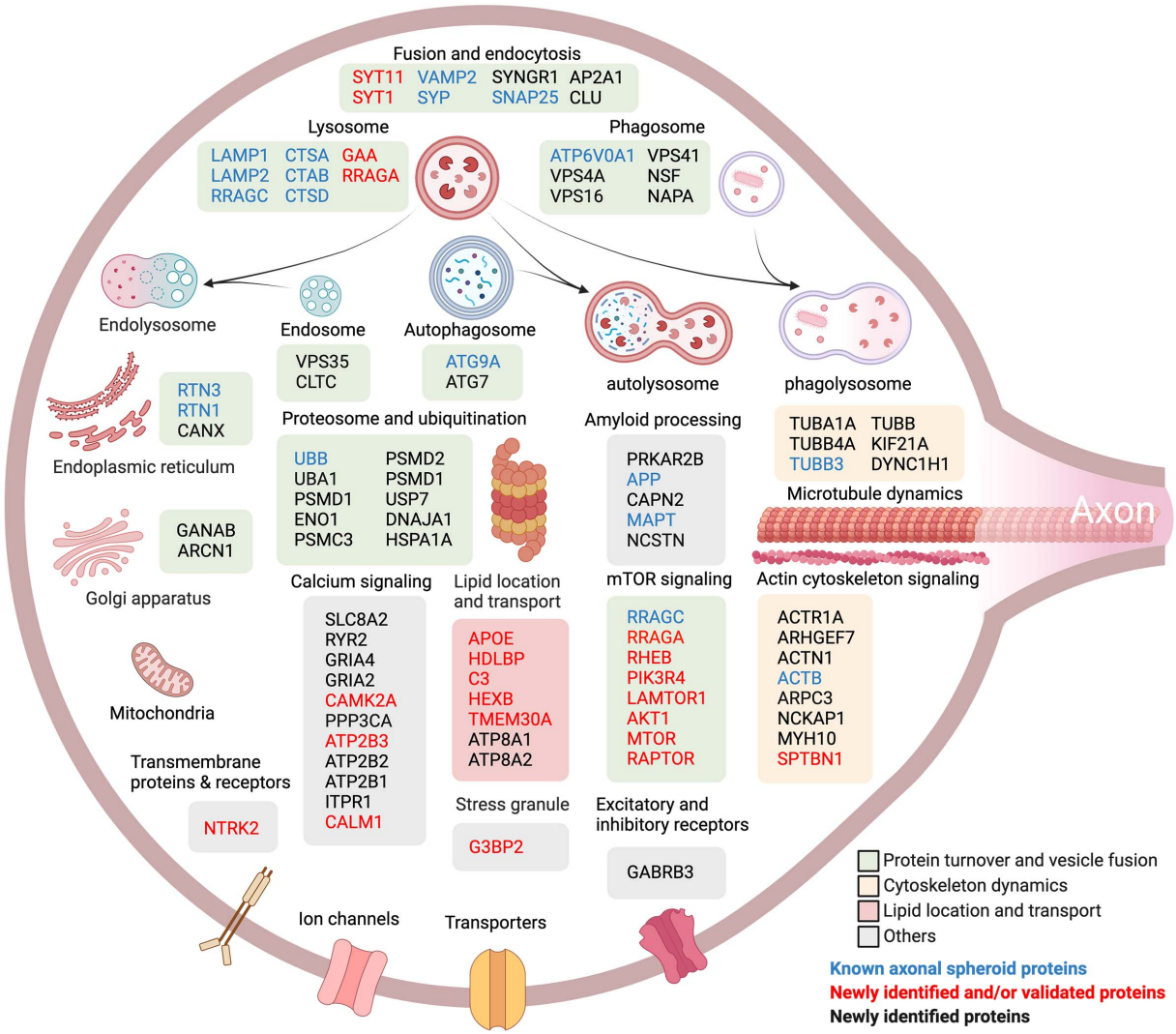

Figure 8. A schematic of the molecular architecture of plaque-associated axonal spheroids

Proximity-labeling proteomics reveals proteins preferentially involved in a variety of subcellular organelles, the ubiquitin-proteosome system and cytoskeleton. These proteins and their signaling pathways relate to biological functions including protein turnover and vesicle fusion (green box); cytoskeletal dynamics (yellow box); lipid localization and transport (red box) and others (grey box). Here we depict selected newly identified and validated proteins as well as those previously known to be enriched in PAAS (lysosomal proteins LAMP1 [4], Cathepsin B and D [14] , RAGC [14], PLD3 [47, 48]; autophagosome protein ATG9A [91] and endoplasmic reticulum protein RTN3 [91] and RTN1 [92]; cytoskeletal neurofilament protein [93], microtubule TUBB3 [20]; synaptic proteins Synaptophysin [5] and VAMP2 [14], APP [31], Tau (MAPT) [26] and Ubiquitin [71, 91]) (**Table S2**).

784 **ONLINE METHODS**

785 **Human postmortem brain tissue**

786 Snap-frozen postmortem human brain specimens of frontal cortices from AD patients and age-
787 matched controls were obtained from the Yale Alzheimer's Disease Research Center and the
788 Banner Sun Health Research Institute. Detailed demographic and clinical information can be
789 found in **Figure S1**. For proximity labeling proteomics, 6 AD cases with intermediate to high AD
790 level [64] and 8 age-matched unaffected controls were used. To reduce inter-sample variability
791 and maximize signal-to-noise by avoiding brains with low-density amyloid deposition, we
792 carefully inspected ~ 40 individual postmortem brains using microscopy and selected for
793 proteomic analysis 6 AD brains with the highest density of amyloid plaques and axonal spheroids
794 within the frontal cortex. The grey matter regions with high plaque load were microdissected out
795 from AD brain sections under visual guidance using a fluorescence stereomicroscope(Leica).
796 Similarly, the grey matter regions were dissected from unaffected control brain sections. For
797 immunofluorescence proteomic validations, 25 severe AD and 14 unaffected control cases were
798 used (**Figure S1**).
799

800 **Human iPSC line and human primary astrocytes**

801 Two fully characterized, de-identified control human iPSC lines NSB3182-3 (female) and NSB2607
802 (male) were used in all experiments [94]. *NGN2*-induced glutamatergic neurons [56] were
803 generated and co-cultured with human primary astrocytes (ThermoFisher #N7805200, or
804 ScienCell #1800) for all experiments [57].
805

806 **Mice**

807 All animal procedures were approved by the Institutional Animal Care and Use Committee at Yale
808 University. WT (C57BL/6J), 5XFAD (Tg6799) mice [95] and mTOR-flox (JAX #011009) mice [61]
809 were obtained from Jackson Laboratory. 5XFAD and WT mice, used for proximity labeling
810 proteomics, were euthanized at 15-month-old, followed by transcardial perfusion. Three male
811 mice per genotype (WT and 5XFAD) were used. Animals used for immunofluorescence proteomic
812 validation were euthanized at 2-3 or 12-15 months of age, with 3 biological replicates per
813 experiment. mTOR-flox mice were cross-bred with 5XFAD mice to create an mTOR-flox-5XFAD
814 line. For AAV-mediated mTOR heterozygous knockout experiments, mTOR-flox-5XFAD mice were
815 injected with AAVs at 6 weeks of age. Five biological replicates (combining male and female mice)
816 in each group were used for AAV9-hSyn-cre-2a-tdT experiment, and 3 male mice in each group
817 were used for AAV-PHPeB experiment.
818

819 **Antibodies and reagents**

820 Full list of primary antibodies for newly validated and known PAAS proteins can be found in **Table**
821 **S2**, including catalog number, RRID, dilution factors and brief staining instructions. Briefly, Anti-
822 PLD3 antibody, anti-SMI312 and anti-Cathepsin D were used to label PAAS in both mice and
823 humans. Anti-Lamp1 and anti-Cathepsin B antibodies were used to label PAAS in mice. For
824 proteomic hits validation, anti-GAA, anti-GBA, anti-TPP1, anti-ATP6V0A1, anti-SYT11, anti-G3BP1,
825 anti-G3BP2, anti-ITM2B, anti-SPTBN1, anti-SV2A, anti-ATP2B3, anti-CAMK2A, anti-Calmodulin,
826 anti-SYT1, anti-CACNA2D1, anti-CACNA1B, anti-NTRK2, anti-mTOR, anti-p-mTOR S2448, anti-

827 PIK3R4, anti-AKT1, anti-LAMTOR, anti-RAGA, anti-RAGC, anti-RHEB, anti-RAPTOR, anti-HDLBP,
828 anti-APOE, anti-C3, anti-HEXB and anti-TMEM30A were used for validating newly identified PAAS
829 proteins. Anti-RAGC, anti-ATG9A, anti-Ubiquitin, anti-RTN3, anti-PKC, anti-synaptophysin, anti-
830 SNAP25, anti-VAMP2 and anti-beta Tubulin III were used for immunostaining of known PAAS
831 proteins. To reveal GFP and tdTomato protein expression, anti-GFP (1:500, RRID:AB_10000240)
832 and anti-RFP (1:200, RRID:AB_2209751) were used respectively. For staining neuronal and glial
833 markers in iPSC-derived human neurons, anti-neurofilament H (1:1000, RRID:AB_2149761), anti-
834 NeuN (1:1000, RRID:AB_10711040), anti-NeuN (1:200, RRID:AB_2532109), anti-Synapsin1/2
835 (1:500, RRID:AB_2622240), anti-PSD95 (1:200, RRID:AB_10807979), anti-S100b (1:500,
836 RRID:AB_2814881), anti-IBA1 (1:100, RRID:AB_2891289) were used. To stain amyloid beta
837 deposits, anti-6e10 (1:200, RRID:AB_2565328) was used. To stain phosphorylated Tau, anti-
838 phospho-Tau S235 (1:1000, Thermo-Fisher), anti-phospho-Tau S396 (1: 200) and anti-phospho-
839 Tau S404 (1:200) were used (RRID see **Table S2**). Dendritic marker MAP2 (1:200, RRID:AB_776174)
840 was used. For puromycylation, anti-puromycin-647 (1:1000, RRID:AB_2736876) was used.
841 Thioflavin S (Sigma-Aldrich, T1892, 2% w/v stock solution, 1:10,000 staining) was used to label
842 amyloid plaques. Alexa dye-conjugated secondary antibodies were used (1:600, ThermoFisher
843 Scientific).
844
845 **Tissue fixation**
846 We have compared the impact of different tissue fixation approaches on the proximity labeling
847 efficacy and protein extraction efficiency. For human brain samples, snap-frozen postmortem
848 human brains coupled with fresh fixation in 4% PFA at 4 °C for ~24 hours worked the best. For
849 mice, freshly perfused mouse brains and fixed in 4% PFA at 4 °C for ~24 hours performed the best
850 in both proximity labeling efficacy and protein extraction efficiency. We found that long-term
851 fixation and storage with the FFPE method markedly reduced both proximity labeling and protein
852 extraction efficiencies.
853
854 **Proximity labeling in brain tissue**
855 Proximity labeling in human and mouse tissue was performed based on [43] with optimizations.
856 Detailed procedures are described below. Axonal spheroids were proximity labeled by using anti-
857 PLD3 or anti-Lamp1 antibodies in mice and humans. Neuronal soma were proximity labeled using
858 anti-NeuN antibody. Briefly, frozen postmortem human brain specimens were fixed by
859 submerging into ice cold 4% paraformaldehyde, and put onto a shaker at 4 °C for ~ 24 hours. For
860 mice, after transcardial perfusion, brains were fixed in 4% paraformaldehyde at 4 °C for ~ 24
861 hours while shaking. Human and mouse brains were vibratome sectioned at 50 µm thickness.
862 Ten sections (around 1cm x 0.8cm each) for human or mouse brain were used in each
863 reaction/per biological replicate. Human sections contained mostly grey matter. Six to eight
864 human biological replicates were used in each group, and three biological replicates were used
865 in each mouse group. Sections were permeabilized by PBS with 0.5% Triton X-100 for 7 min,
866 followed by rinsing with PBST (0.1% Tween-20 in PBS). To quench the endogenous peroxidase
867 activity, sections were incubated in 0.1% H_2O_2 for 10 min, followed by rinsing with PBST twice.
868 Primary antibody diluted in blocking buffer (0.1% Tween-20 with 1% BSA in PBS) was incubated
869 overnight at 4 °C on a shaker, followed by PBST washes for 3 times 20 min/per wash. Secondary
870 antibody conjugated with HRP was incubated in blocking buffer for 1 hour at room temperature,

871 followed by PBST washes for 3 times ~40 min/per wash. Proximity labeling was performed by
872 using Biotin-XX-Tyramide dissolved in 50 mM Tris-HCl buffer (pH = 7.4), with H_2O_2 for 5 min,
873 according to the user's manual (ThermoFisher Scientific B40921). Specifically, every 1 mL of
874 reaction solution was made of 10 µL 1X Biotin-XX-Tyramide and 10 µL 1X H2O2 in 50 mM Tris-
875 HCl buffer. Biotinylation reactions were terminated by rinsing sections with freshly made 500
876 mM sodium ascorbate for 3 times, followed by PBST washes for 3 times.

877 **Enrichment of biotinylated proteins using streptavidin beads**
878 We performed proximity labeling proteomics on fixed brain specimens, which may reduce the
879 protein extraction yield compared to other proximity labeling methods using fresh tissue. Thus,
880 we optimized the protein extraction protocol and largely increased the protein extraction yield
881 compared to previously published methods (**Figure S4A**)[43]. Specifically, brain sections from
882 proximity labeling experiments were lysed and de-crosslinked in 100 mM Tris-HCl buffer (pH =
883 8.0) with 2% SDS and protease inhibitor (Roche) at 95 °C for 45 min with constant shaking. For
884 every 10 brain sections, 500uL lysis buffer was used. Protein lysate was sonicated using Sonic
885 Dismembrator Model 500 (Fisher Scientific) for 3 times, 3 sec/per time at 4°C. Protein lysate was
886 centrifuged at 12k rcf for 5 min. Then, 450 µL protein lysate supernatant was collected from each
887 sample, incubated with 550 µL of PBST containing 200 µL prewashed streptavidin magnetic beads
888 (ThermoFisher Scientific #88817), protease inhibitor and phosphatase inhibitor, to meet a final
889 1mL volume. Samples were then incubated on a 360° rotator at 4 °C overnight. The rest of protein
890 lysates were used for protein concentration measurement by BCA (ThermoFisher Scientific).
891 After incubation, beads were sequentially washed once with PBST, twice with PBST with 1 M NaCl,
892 twice with PBS. Biotinylated proteins were eluted in elution buffer (20 µL of 20 mM DTT and 2
893 mM Biotin in 1X NuPAGE LDS lysis buffer (ThermoFisher) with protease inhibitor and phosphatase
894 inhibitor) at 95 °C for 5min. Supernatant was collected and centrifuged at 12k rcf for 1min,
895 followed by running into a 4%–20% Tris-Glycine gel (Invitrogen) at constant 150 V until all the
896 proteins had run into the gel (approximately 10min). Gel was rinsed once in ultrapure water
897 (AmericanBio) and incubated in ~50 mL of Coomassie blue R-250 staining solution (Bio-Rad) for
898 1 hour incubation. Gel was de-stained with Coomassie blue R-250 destaining solution (Bio-Rad)
899 for 2 hours with 3 times buffer changes. Gel was rinsed with ultrapure water for three times. Gel
900 containing protein samples was visualized, cut with clean blades, and kept at -20 °C.
901

902 **Enrichment of biotinylated peptides using Anti-biotin antibody**
903 The labeled tissue was lysed using 100 mM Tris-HCl buffer (pH = 8.0) with 2% SDS and protease
904 inhibitor (Roche). The lysates were sonicated and then centrifuged at 16,500 g for 10 min at 4°C.
905 The proteins were precipitated using acetone and the pellet was dissolved in 8M urea, 50 mM
906 ammonium bicarbonate (ABC), then sonicated for 30 sec to re-solubilize the proteins. A Bradford
907 Assay was performed to determine protein concentration and 2 mg of protein was used to
908 processed further. Proteins were reduced with 5 mM DTT for 45 min at RT and subsequently
909 carbamidomethylated with 10 mM iodoacetamide for 30 min at RT in the dark. Prior to digestion,
910 the urea concentration was reduced to 2 M with 50 mM ABC) and digested with trypsin at an
911 enzyme:substrate ratio of 1:50 overnight at 37 °C. Following digestion, samples were acidified
912 with 10% formic acid and de-salted using Nest Group C18 macro-spin columns (HMMS18V) as
913 per manufacturer's instructions. Biotinylated peptides were enriched using anti-biotin antibody-

914 based immunoprecipitation (IP). The peptides were dissolved in IAP buffer containing 50 mM
915 MOPS, 10 mM HNa2PO4, 50 mM NaCl at pH 7.5. Anti-biotin beads (Immune Chem
916 Pharmaceuticals) were washed twice in IAP buffer before the samples were added to the beads
917 for incubation on a rotator for 2 hrs at 4°C. The beads were washed twice with IAP buffer and
918 twice with H2O (HPLC-grade). The biotinylated peptides were eluted from the beads using 80%
919 ACN and 0.15% TFA with vortexing followed by a 10 min incubation at room temperature. The
920 elution was repeated twice, and the supernatants were collected and vacuum dried.

921 **Western blotting**
922 For western blot, 4%–20% Tris-Glycine gels (Invitrogen) were used for protein electrophoresis
923 following the manufacturer's protocol. Proteins were transferred to nitrocellulose membranes
924 (BioRad) at constant 350 mA for about 50 min. After blocking with 5% bovine serum albumin
925 (BSA) in TBST (Tris-buffered saline with 0.1% Tween 20) for 1 hour, membranes were incubated
926 with primary antibodies (anti-PLD3 1:250; anti-CatB 1:1000, anti-RAGC 1:1000, anti-NeuN 1:1000;
927 anti-GAPDH 1:1000) diluted in 5% BSA in TBST on a shaker at 4 °C overnight, followed by three
928 times of 15min washes with TBST. Membranes were then incubated with horseradish peroxidase
929 (HRP) conjugated secondary antibodies diluted in 5% BSA in TBST for 1 hour at room temperature,
930 followed by three times of 15min washes with TBST. To blot biotinylated proteins on the same
931 membrane, stripping buffer (ThermoFisher #46430) was used to cover the whole membrane and
932 incubated at room temperature with shaking for 10-12 min, followed by rinsing with PBST for 3
933 times. HRP-conjugated streptavidin (1:1000) was diluted in blocking buffer for 1-2 hours at room
934 temperature or 4 °C overnight. Clarity Western ECL blotting substrate (Bio-Rad) and ChemiDoc
935 MP imaging system (Bio-Rad) were used for chemiluminescence development and detection.
936
937 **In-Gel Digestion**
938 Gel slices were cut into small pieces and washed with 600 µL of water on a tilt-table for 10 min
939 followed by 20 min wash with 600 µL 50% acetonitrile (ACN)/100 mM NH4HCO3 (ammonium
940 bicarbonate, ABC). The samples were reduced by the addition of 100 µL 4.5 mM dithiothreitol
941 (DTT) in 100 mM ABC with incubation at 37ºC for 20 min. The DTT solution was removed and the
942 samples were cooled to room temperature. The samples were alkylated by the addition of 100
943 µL 10mM iodoacetamide (IAN) in 100 mM ABC with incubation at room temperature in the dark
944 for 20 min. The IAN solution was removed, and the gels were washed for 20 min with 600 µL 50%
945 ACN/100 mM ABC, then washed for 20 min with 600 µL 50% ACN/25 mM ABC. The gels were
946 briefly dried by SpeedVac, then resuspended in 100 µL of 25 mM ABC containing 500 ng of
947 digestion grade trypsin (Promega, V5111), and incubated at 37ºC for 16 hrs. The supernatants
948 containing the tryptic peptides were transferred to new Eppendorf tubes. Residual peptides in
949 the gel bands were extracted with 250 µL 80% ACN/0.1% trifluoroacetic acid (TFA) for 15 min,
950 then combined with the original digests and dried in a SpeedVac. Peptides were dissolved in 24
951 µL MS loading buffer (2% acetonitrile, 0.2% trifluoroacetic acid), with 5 µL injected for LC-MS/MS
952 analysis.
953
954 **LC-MS/MS on the Thermo Scientific Q Exactive Plus**
955 LC-MS/MS analysis was performed on a Thermo Scientific Q Exactive Plus equipped with a Waters
956 nanoAcquity UPLC system utilizing a binary solvent system (A: 100% water, 0.1% formic acid; B:

957 100% acetonitrile, 0.1% formic acid). Trapping was performed at 5 µL/min, 99.5% Buffer A for 3
958 min using an ACQUITY UPLC M-Class Symmetry C18 Trap Column (100Å, 5 µm, 180 µm x 20 mm,
959 2G, V/M; Waters, #186007496). Peptides were separated at 37 °C using an ACQUITY UPLC M-
960 Class Peptide BEH C18 Column (130Å, 1.7 µm, 75 µm X 250 mm; Waters, #186007484) and eluted
961 at 300 nL/min with the following gradient: 3% buffer B at initial conditions; 5% B at 2 min; 25% B
962 at 140 min; 40% B at 165 min; 90% B at 170 min; 90% B at 180 min; return to initial conditions at
963 182 min. MS was acquired in profile mode over the 300-1,700 m/z range using 1 microscan,
964 70,000 resolution, AGC target of 3E6, and a maximum injection time of 45 ms. Data dependent
965 MS/MS were acquired in centroid mode on the top 20 precursors per MS scan using 1 microscan,
966 17,500 resolution, AGC target of 1E5, maximum injection time of 100 ms, and an isolation window
967 of 1.7 m/z. Precursors were fragmented by HCD activation with a collision energy of 28%. MS/MS
968 were collected on species with an intensity threshold of 1E4, charge states 2-6, and peptide
969 match preferred. Dynamic exclusion was set to 30 sec.
970
971 **Peptide Identification**
972 Data was analyzed using Proteome Discoverer software v2.2 (Thermo Scientific). Data searching
973 was performed using the Mascot algorithm (version 2.6.1) (Matrix Science) against the
974 SwissProtein database with taxonomy restricted to human (20,368 sequences) or mouse (17,034
975 sequences) as well as a streptavidin sequence. The search parameters included tryptic digestion
976 with up to 2 missed cleavages, 10 ppm precursor mass tolerance and 0.02 Da fragment mass
977 tolerance, and variable (dynamic) modifications of methionine oxidation and carbamidomethyl
978 cysteine. Normal and decoy database searches were run, with the confidence level set to 95%
979 ($p<0.05$). Scaffold v5.1.2 (Proteome Software Inc., Portland, OR) was used to validate MS/MS-
980 based peptide and protein identifications. Peptide identifications were accepted if they could be
981 established at greater than 95.0% probability by the Scaffold Local FDR algorithm. Protein
982 identifications were accepted if they could be established at greater than 99.0% probability and
983 contained at least 2 identified peptides (one uniquely assignable to the protein). Proteins that
984 contained similar peptides and could not be differentiated based on MS/MS analysis alone were
985 grouped to satisfy the principles of parsimony. Proteins sharing significant peptide evidence were
986 grouped into clusters. Label-free quantification was performed with Scaffold software. Spectral
987 intensity values were used for protein quantification between groups.
988
989 To search for biotinylation sites in the anti-biotin antibody pulldown samples, the variable
990 modifications of biotin-xx-tyramide were configured to account for marker ions resulting from
991 fragmentation of biotinylated peptides. These marker ions have the following m/z values and
992 elemental composition losses from the fully modified amino acid: dehyrdrobiotin (m/z-227.08),
993 Biotin-x ion (m/z-340.25), Biotin-xx ion (m/z-453.25), immonium of tyrosine-Bxxp with loss of
994 ammonia (m/z-706.38), immonium of tyrosine-Bxxp (m/z-723.38).
995
996 **Proteomic data analysis**
997 Prior to the data analysis, missing values were removed. For example, if a protein A had 0 spectra
998 count detected in all the samples, including tests and controls, then protein A was removed from
999 the list. Normalized total spectra count (NTSC) and normalized total precursor intensity (NTPI)
1000 are two common methods for proteomic quantification. For PLD3-labeled PAAS proteomes in

1001 humans, we compared NTSC and NTPI methods, and used the shared proteomic hits for
1002 downstream analysis. For PLD3-labeled PAAS proteomes in mice, Lamp1-labeled proteomes in
1003 mice and NeuN-labeled neuronal nuclei and perinuclear cytoplasm proteomes in mice, we used
1004 NTSC for quantification. To obtain the PAAS proteome, differentially expressed proteins were
1005 analyzed by comparing proteomic hits obtained from PLD3-labeled samples versus those from
1006 control samples using no antibody. This allowed the filtering of endogenously biotinylated
1007 proteins and non-specific binders to streptavidin beads. To obtain the optimal cutoff values for
1008 the statistical analysis we tested different degrees of stringency for FDR (0.1, 0.05 and 0.01) and
1009 fold change (1 and 1.5). An optimum cutoff $p < 0.05$, FDR < 0.1 and fold change > 1.5 was used
1010 for these datasets, as it captures the maximum numbers of known PAAS proteins while excluding
1011 the maximum numbers of potential contaminants. Post-cutoff proteomic lists were scrutinized
1012 for possible glial contaminations by cross validations using single cell RNAseq (scRNAseq)
1013 transcriptomics in mice [55] and humans [96] and Tissue Atlas in The Human Protein Atlas [97].
1014 When a gene had an FPKM < 10 in neurons and an FPKM > 10 in other cell types in the mice
1015 scRNAseq dataset [55], or the mean expression level was less than 0.03 in neurons but greater
1016 than 0.03 in glia in the AD pathology human scRNAseq dataset [96], and protein expression was
1017 not detected in neurons from the Tissue Atlas [97], this gene was excluded from the proteomic
1018 results. Two such genes (EPHX1 and PSAT1) were excluded from the PAAS proteome in AD
1019 humans, and five such genes (Gsn, Ephx2, Gfap, Myh9 and Anxa2) were excluded from the PAAS
1020 proteome in AD mice. Proteomic hits that passed these thresholds were considered the final
1021 PAAS proteomes in AD humans or mice. Lists of raw and filtered proteomic hits of PAAS and
1022 neuronal soma proteomes in AD humans and mice can be found in **Table S1**.
1023
1024 For gene ontology analysis (**Figure 3A, Figures S9C and S13B**), we uploaded the final proteomes
1025 to the GeneOntology.org [98, 99], the g:profiler [100] or the ToppGene Suite search portal [101]
1026 and plotted the top ten or top twenty retrieved terms on cellular compartment or biological
1027 process with the lowest false discovery rates. Pathway enrichment analysis was performed by
1028 retrieving Gene Ontology Biological Process, Cellular Component and Molecular function terms
1029 from g:profiler [100] using terms size 5-200. The enrichment map was visualized in Cytoscape
1030 (v3.9.1) [102]. For IPA pathway analysis (**Figures 3B-C and Figures S9D-E**), the human or mice
1031 PAAS proteome was imported into Ingenuity Pathway Analysis (IPA) software (QIAGEN, 2022
1032 release version)[103] for canonical pathway analysis. The top IPA pathways with the lowest false
1033 discovery rates and potential relevance to PAAS pathology were listed. For gene set enrichment
1034 analysis (GSEA) (**Figure 4A**), PLD3 labeled proteomes of AD humans and unaffected controls were
1035 uploaded into the Broad Institute GSEA software 4.3.2 [104] to perform gene ontology analysis
1036 using default values, except the size was set to 200 to remove the larger sets from analysis. GSEA
1037 results were loaded into Cytoscape (v3.9.1) for pathway enrichment analysis using
1038 EnrichmentMap [105] and AutoAnnotate [106] plugins with default values. Principal component
1039 analysis was performed using Qlucore Omics Explorer v3.6 (Qlucore AB, Lund, Sweden).
1040
1041 **Immunofluorescence of fixed specimens and human iPSC-derived co-culture**
1042 The complete list of antibodies, dilution factors, and immunofluorescence instructions for
1043 immunofluorescence staining of fixed specimens of humans and mice, can be found in **Table S2**.
1044 Briefly, for mice and human brains, fixation and vibratome sectioning was the same as described

1045 in the proximity labeling section. Heat-induced sodium citrate antigen retrieval was performed
1046 when necessary (see IF instructions in **Table S2**). Immunofluorescence staining was then
1047 performed with the following protocol: tissue was boiled in 50 mM sodium citrate with 0.05%
1048 tween-20 at 95 °C for 45 min, followed by 30 min cool down at RT and rinse with PBS for three
1049 times. Primary antibodies incubation was 12 hours to 3 days at 4 °C in blocking buffer (PBS with
1050 1% BSA and 0.1% Tween-20) and secondary antibodies were incubated in blocking buffer at 4 °C
1051 overnight. Thioflavin S (Sigma-Aldrich, T1892, 2% w/v stock solution, 1:10,000 staining) was used
1052 for labeling amyloid deposits. Three times washes with PBST were performed before mounting
1053 tissues on slides with PermaFluor (Thermo Scientific, TA-030-FM).
1054
1055 For immunofluorescence of human iPSC-derived neuron-astrocyte co-culture, cells were washed
1056 3 times with pre-warmed PBS before fixing with 4% PFA (ice-cold) at RT for 20 min. Cells were
1057 washed with PBS 15 min x 3 and were blocked with blocking buffer (1% BSA in PBS, plus 0.1%
1058 tween-20) for 1 h. Primary antibodies were diluted in blocking buffer and incubated with cells at
1059 4 °C overnight. Cells were washed with PBST 15 min x 3. Secondary antibodies were diluted in
1060 blocking buffer and incubated with cells at 4 °C overnight. ThioflavinS (2% w/v stock solution,
1061 1:10,000 staining) was diluted in PBS and incubated with cells at RT for 5 min. Cells were washed
1062 with PBST 15 min x 3, before imaging.
1063
1064 **Fixed tissue and live cell time-lapse confocal microscopy imaging**
1065 An upright or an inverted Leica SP8 confocal microscope was used to generate all images. Laser
1066 and detector settings (GaAsP hybrid detection system, photon counting mode) were maintained
1067 constant. For all analyses, single z stack images or tiled images were obtained in the
1068 somatosensory cortex in mice. All images were obtained using a 63x oil immersion objective (N.A.
1069 1.40), 40x water immersion objective (N.A. 1.10) or 25x water immersion objective (N.A. 0.95) at
1070 1,024 x 1,024-pixel resolution, z-step size of 1 µm, as we previously described [31]. When
1071 indicated, deconvolution was performed using the default setting in the Leica SP8 LAS X software.
1072 For time-lapse imaging of spheroids growth in human neurons, 96-well plates were imaged in the
1073 Leica SP8 incubator, with the temperature set at 37°C and supplied with CO_2. Tilling images were
1074 obtained using a 63x oil immersion objective (N.A. 1.40) at 512 x 512-pixel resolution, zoom factor
1075 at 3 and z-step size of 1 or 1.5 µm at every day for 7 days.
1076
1077 **Lentivirus plasmid purification, lentivirus production and concentration**
1078 *Escherichia coli* stocks for pMDLg/pRRE (MDL), pRSV-Rev (Rev), pCMV-VSV-G (VSVG), FUW-
1079 M2rtTA and pLV-TetO-hNGN2-eGFP-Puro were purchased from Addgene (12251, 12253, 8454,
1080 20342 and 79823, respectively). Bacteria was grown in 500 mL of LB Broth (Fisher Scientific,
1081 DF0446-07-5) with 100 µg/mL Ampicillin (Sigma, A9518) overnight at 37 °C and 200 rpm. The
1082 following day, bacterial cells were pelleted by centrifugation at 4000 g for 10 min at 4 °C. The
1083 supernatant was discarded, and plasmids purified using the PureLink™ HiPure Plasmid Filter
1084 Maxiprep Kit (Invitrogen, K210017), following the manufacturer instructions.
1085
1086 Third generation lentiviral vectors were produced as we described [107]. Briefly, HEK 293T cells
1087 (Invitrogen, R700-07) were grown in 15-cm plates (Falcon, 353025) in DMEM (Gibco, 12430054)
1088 supplemented with 10% FBS (Gibco, 10438026) until reaching 70-80% confluency. For cell

1089 transfection, the following solution was prepared in 500 µL of pre-warmed Opti-MEM (Gibco,
1090 31985062) per plate: 12.2 µg of transfer plasmid, 8.1 µg of MDL, 3.1 µg of Rev, 4.1 µg of VSVG
1091 and 110 µL of Polyethylenimine (1 µg/µL; Polysciences, 23966-2). This solution was incubated for
1092 10 min at room temperature, vortexed gently and added dropwise onto HEK 293T cells for
1093 transfection. Medium was changed after 6 h of incubation and harvested at 48 h and 72 h post
1094 transfection. Media containing viral particles was sterile-filtered and concentrated using the
1095 Lenti-X™ Concentrator (Takara Bio, 631231), according to the manufacturer instructions.
1096
1097 **Human neuron-astrocyte co-culture AD model**
1098 Human iPSC control lines 3182-3 and 2607 were used in this study, as we first described this line
1099 in [94]. Maintenance and passaging of human iPSC were performed as we previously described
1100 [108]. Human primary astrocytes (ThermoFisher #N7805200 or ScienCell #1800) were
1101 maintained as described in the user manual. iPSC-derived NGN2-induced glutamatergic neuron
1102 generation was performed as we previously described [108]. Briefly, human iPSCs maintained in
1103 6-well-plates were harvested by incubating in Accutase (Innovative Cell Technologies AT104) 1
1104 mL/per well plus 10 µM ROCK inhibitor THX (RI) (Tocris #1254) at 37 °C for 20 min. Dissociated
1105 iPSCs were then collected in a 50 mL falcon tube and mixed well with DMEM (ThermoFisher
1106 #11966025) (preferably 1:3 Accutase : DMEM). iPSCs were centrifuged for 4 min at RT at 1000 g.
1107 iPSCs were resuspended in 1-2 mL of Stemflex (ThermoFisher) with 10 µM RI and counted, diluted
1108 in Stemflex with THX to a cell suspension concentration of 1e6 cells/mL. Lentiviruses NGN2-Puro
1109 and rtTA (titer 4.40 x 10^10 gc/mL) at 50 uL per 10e6 cells of suspension were added. Cells were
1110 mixed and dispensed at 120k cells/per well (6 well size) coated with 1x Geltrex (ThermoFisher).
1111 Cells were incubated at 37 °C incubator overnight. DIV1: media was replaced with induction
1112 media (DMEM F12 with Glutamax and Sodium Pyruvate (Thermofisher, #10565018), 1% N-2
1113 (Thermofisher, #17502048), 2% B-27-RA (Thermofisher, #12587010), Doxycycline for a final
1114 concentration of 1ug/mL). DIV2 and 3: replaced media with induction media containing
1115 puromycin (2 ug/mL) on each day. DIV4: Neurons were dissociated with Accutase plus 10 µM RI
1116 for 20 min, washed off with 1:3 DMEM, resuspended and centrifuged at 1000 g for 5 min.
1117 Resuspend pellet at a concentration of 1e6 cells/ml in neuron media (Brainphys (STEMCELL, #
1118 05790), 1% N-2, 2% B-27-RA, 1 µg/mL Natural Mouse Laminin (Thermofisher, # 23017015), 20
1119 ng/mL BDNF (R&D, #248), 20 ng/mL GDNF (R&D, #212), 250 µg/mL Dibutyryl cyclic-AMP (Sigma,
1120 #D0627), 200 µM L-ascorbic acid (Sigma, # A4403) and 1x Anti-Anti (ThermoFisher)) with Dox
1121 1µg/mL, puromycin 2 µg/mL, 4 µM AraC (Sigma #C6645) and 10 µM RI. Neurons were replated
1122 onto 2x Geltrex coated 96-well-plates (PerkinElmer #6055302) and seeded at 10e5 per well (96-
1123 well plate size). DIV5: media was replaced with neuron medium containing puromycin 2 µg/mL
1124 and AraC 4 µM. DIV6: media was replaced with neuron medium with 4 µM AraC. DIV8: media
1125 was replaced with neuron medium with 2 µM AraC. DIV10: human primary astrocytes were
1126 dissociated with TrypLE (ThermoFisher), washed with DMEM, centrifuged at 400 rcf for 5 min,
1127 counted and plated into NGN2 neurons culture at 20k cells/per well (96-well-plate size). Human
1128 iPSC-derived neuron-astrocyte co-culture was maintained as previously described [57] with
1129 modifications. Briefly, human neuron-astrocyte co-cultures were maintained in neuron media
1130 plus 1.5% FBS for 1 week, then reduced FBS to 0.5% for another week. Media was half-changed
1131 every other day. After that, human neuron-astrocyte co-cultures were maintained in neuron
1132 maintenance medium (1X BrainPhys Basal (StemCell Technology), 1X B27 with Vitamin A

1133 (ThermoFisher), 1X N2 (ThermoFisher), 5 μg/ml Cholesterol (Sigma-Aldrich), 1 mM Creatine
1134 (Sigma-Aldrich), 10 nM β-estradiol, 200 nM Ascorbic Acid, 1 mM cAMP (Sigma-Aldrich), 20 ng/ml
1135 BDNF (Peprotech), 20 ng/ml GDNF (Peprotech), 1 μg/ml Laminin, 0.5 mM Glutamax
1136 (ThermoFisher), 1 ng/ml TGF-β1 (Peprotech), 1X Normocin (InvivoGen), 50 U/ml Penicillin-
1137 Streptomycin (ThermoFisher)) with half-changed of media every other day until harvest, or other
1138 assays. For AD modeling, amyloid beta 1-42 peptide (AnaSpec AS-72216) was oligomerized to
1139 prepare soluble amyloid beta species as previously described [57, 109]. Briefly, soluble amyloid
1140 beta species were added to the neuron maintenance medium at a final concentration of 5 μM
1141 and applied to the human neuron-astrocyte co-culture for 7 days, with half-change of media
1142 every other day as previously described [57].
1143
1144 For mTOR signaling inhibition, Torin1 (TOCRIS 4247) or vehicle DMSO was added to the neuron
1145 maintenance medium at a final concentration of 250 nM [59], and applied to the human neuron-
1146 astrocyte co-culture 3 days before amyloid beta treatment. Then, Torin1 or vehicle DMSO was
1147 added to the neuron maintenance medium at 250 nM concentration, along with soluble amyloid
1148 beta species at 5 μM concentration, and applied to the human neuron-astrocyte co-culture for 7
1149 days, with a half-change of medium every other day. For Torin1 treatment after axon spheroids
1150 formation, soluble amyloid beta species at 5 μM concentration, and applied to the human
1151 neuron-astrocyte co-culture for 7 days, then Torin1 or vehicle DMSO was added to the neuron
1152 maintenance medium at 250 nM concentration for another 7 days.
1153
1154 For time-lapse imaging of spheroid growth in human neurons, AAV9-hSyn-mCherry (Addgene
1155 #114472) and AAV2-CAG-LAMP1-GFP (home produced as we previously described [4]) were co-
1156 transduced at 2 x 10^9 vg/100 μL medium in 4-month-old co-cultures. Human neuron-glia co-
1157 cultures were treated with amyloid at day 150. Time lapse confocal imaging was performed
1158 several hours before the treatment, and imaged every day post-treatments.
1159
1160 **Calcium imaging in iPSC-derived human neurons**
1161 AAV1-CAMKII-GCamp8f (Addgene #176750, 7 x 10^12 vg/mL) was transduced in 2-month-old
1162 iPSC-derived human neurons, along with AAV9-CB7-mCherry (Addgene # 105544, 1 x 10^13 vg/mL)
1163 at 1 μL per 0.2 mio cells. Transduced cells were maintained with regular media changes. Calcium
1164 imaging was performed one month after transduction. Calcium imaging was performed using an
1165 Andor Dragonfly spinning disk confocal on Nikon Ti2-E microscope. A 20×/0.75 NA air objective
1166 and Zyla scientific complementary metaloxide semiconductor (sCMOS) camera were used.
1167 Imaging was performed in culture medium, a stage-top incubator and objective heater (Oko-Lab)
1168 maintained the sample temperature at 37°C. For stimulated calcium imaging, a pair of tinfoil wire
1169 electrodes separated around 1.5 mm apart was placed in the in the bottom of the well using a
1170 micromanipulator and utilized for electrical stimulation. Electric stimulation was performed using
1171 the trigger out function in the Andor software. GCaMP8f-labeled neurons were imaged through
1172 excitation at 488 nm wavelength with the acquisition speed of 20 Hz, and 512 x 512
1173 resolution. Stimulation trains of 20 ms pulses were delivered to the electrodes at 50 Hz (20 ms
1174 interval) with 300 to 700 μA currents for 1s. Electric stimulation was triggered automatically at
1175 the 100-frame time point, and image for 300 or 500 frames in total. The calcium responses within
1176 the imaging window were monitored upon stimulation.

Calcium imaging raw data were de-noised using DeepCAD-RT [110]. The denoising model was trained with the different datasets acquired with the same imaging conditions. The denoised GCaMP8f fluorescence intensity was normalized to ΔF/F for analysis. Several regions of interest (ROIs) were selected on each axon. The average ΔF before stimulation was used as the baseline measurement. The raw fluorescence intensity over time (F(t)) contained background noise. To isolate the stimulus-evoked signal, we first calculated the average background fluorescence intensity (F0) using data from before stimulus presentation. We then normalized the signal by subtracting F0 at each time point:

$$\frac{\Delta F}{F} \equiv \frac{F(t) - F_0}{F_0}$$

This normalized signal was smoothed using a Savitzky-Golay filter with a window length of 21 data points (1 second) and a polynomial order of 3. This filtering reduced noise while preserving the overall shape of the signal. To quantify the rising slope of the calcium response, we identified the peak of the smoothed signal. The time point halfway to this peak ($t_{1/2}$) was then determined. A linear regression was performed using the 9 data points surrounding $t_{1/2}$. The slope of this regression line provided an estimate of the rising slope of the calcium signal in response to the sensory stimulus.

To determine the onset time of the response for each Region of Interest (ROI) following electrical stimulation, we employed an exponential growth model to fit the rising phase of the signal. Prior to reaching its peak, the normalized calcium trace can be effectively approximated using the following piecewise function:

$$f(t) = \begin{cases} f_0, & t < t_s \\ f_0 + (f_{max} - f_0)(1 - e^{-(t-t_s)/\tau}), & t \geq t_s \end{cases}$$

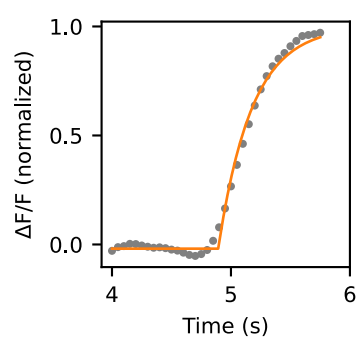

The curve fitting procedure was performed using the curve_fit function available in the scipy.optimize package. In this context, f_0 and f_{max} represent the baseline and maximum normalized calcium signals, respectively. The parameter τ characterizes the timescale of the rising phase, while t_s denotes the response time—the specific time point at which the calcium signal initiates its ascent.

The calcium decay time constant (τ) was estimated by fitting 2.5 s calcium trace beginning from the peak to an exponential equation: Y = a*exp(-x/τ).

Viral-mediated *Mtor* heterozygous knockout in *Mtor*-floxed-5XFAD mice

mTOR is known to be a regulator of cell growth [35, 59], previous studies showed cell size was indistinguishable between the *Mtor* heterozygous knockout and wild-type cells [111], which suggests that the effects of *Mtor* knockout on cell size is *Mtor* gene-copy dose dependent. Thus, we obtained *Mtor* heterozygous floxed AD mice to achieve conditional *Mtor* heterozygous knockout, which had no effect on cell body size (**Figures 6O and S19D**). To achieve global neuronal *Mtor* heterozygous knockout in *Mtor*-floxed-5XFAD mice, 10 µL of AAV-PHPeB-hsyn-

1218 cre-eGFP (Addgene#105540, titer ~1x10^^{13}vg/mL) or AAV-PHPeB-CAG-GFP (Addgene#37825,
1219 titer ~1x10^^{13}vg/mL) was retro-orbitally injected into 6-week-old *Mtor*-floxed-5XFAD mice. To
1220 achieve sparse neuronal *Mtor* heterozygous knockout, 1 µL of AAV9-hsyn-cre-2a-tdT
1221 (Addgene#107738, titer ~1x10^^{13}vg/mL) was diluted with 3 µL of PBS and was injected into the
1222 subarachnoid space of one hemisphere at the level of somatosensory cortex in *Mtor*-floxed-
1223 5XFAD mice, as we previously described [31]. Mouse brains were collected 2 months after virus
1224 injection in the AAV-PHPeB experiment or at 2.5 months for the AAV9-hsyn-cre-2a-tdT injected
1225 mice. Brains were sliced, stained and imaged with confocal microscopy as abovementioned and
1226 as we previously described [31]. For sparsely PHP.eB-hSyn-Cre-GFP viruses labeling in mouse
1227 brains, 3 µL of AAV-PHPeB-hsyn-cre-eGFP (Addgene#105540, titer ~1x10^^{13}vg/mL) was diluted
1228 in 30 µL PBS and retro-orbitally injected.
1229
1230 **RNAscope in 5XFAD mice brain slices**
1231 5XFAD mice brains were freshly dissected and immediately froze in Tissue-TEK O.C.T. compound
1232 (SAKURA) and kept in dry ice with 70% ethanol for 5~10 min, then transferred to -80 °C for long-
1233 term storage. Frozen brain blocks were sectioned at 10 µm thickness by cryostat (Leica).
1234 RNAscope was performed using RNAscope multiplex fluorescent kit V2 (ACD #323270) according
1235 to the fresh frozen tissue protocol. PolyA probe (ACD # 318631) or negative control probe (ACD
1236 #320871) was used during probe incubation. Before counterstain with DAPI and mounting media,
1237 Atto 657 NHS ester (Millipore #07376) was diluted in 1:100 and stained brain section for 10min,
1238 followed by 3-time PBS washes, 5min/per wash. Negative control samples were used to set the
1239 baseline parameters for confocal imaging, before imaging the PolyA probe samples.
1240
1241 NHS ester was used to label the spheroid halo because when we attempted to perform RNAscope
1242 and co-stain with axonal spheroid markers, such as PLD3, SMI312, APP, RAGC, ATP9A, and
1243 ATP6V0A1, we found these antibodies were not compatible with the RNAscope protocol, a well-
1244 known limitation of this technique. Therefore, we leveraged the knowledge from pan-expansion
1245 microscopy [112] that NHS ester can be used to non-specifically label tissues and reveal
1246 subcellular structures using confocal imaging. We applied NHS ester after RNAscope, ensuring
1247 that the NHS ester staining did not interfere with the polyA probe signal from RNAscope.
1248 Interestingly, in the cortex of 5XFAD mice, NHS ester highlighted the neuritic plaque nicely,
1249 allowing us to use it as a marker for spheroids, especially at the periphery of the halo.
1250
1251 **Puromycylation in live mice brains**
1252 Puromycylation was performed as previously described [113] with a few modifications. Briefly,
1253 25 mg puromycin (Sigma #P7255) was diluted in 278 µL of DMSO to make the puromycin stock
1254 solution. Puromycin working solution includes 10 µL of puromycin stock solution, 10 µL DMSO
1255 and 80 µL PEG400 (puromycin final concentration at 9 mg/mL). Anisomycin (Sigma #9789) stock
1256 solution was made as follow: 20 µL DMSO was added to 5 mg anisomycin, and centrifuged at
1257 200g for 3 min. Heat at 42 °C water bath for 2-3 min, until pipet completely dissolved. Then 40
1258 µL of PEG400 was added dropwise with agitation. Solution should keep clear with no
1259 precipitation. Anisomycin working solution was made as follow: 30 µL anisomycin stock solution,
1260 10 µL puromycin stock solution (or DMSO vehicle), and 60 µL PEG400. To make Torin1 stock
1261 solution, 10 mg Torin1 was added to 3.292 mL DMSO and 3.292 mL PEG400 (Torin1 final

concentration at 2.5 mM). Torin1 working solution was made as follow: 30 µL Torin1 stock, 10 µL puromycin stock (or DMSO vehicle), and 60 µL PEG400. All the reagents were freshly made and checked there were no precipitation during the experiment. Mice craniotomy at the somatosensory cortex was done as we previously described [4]. After removing dura, vehicle or anisomycin, or Torin1 working solution was topically applied to cranial window. For anisomycin assay, solution was applied for 30 min, then quickly removed, and replaced with anisomycin plus puromycin solution for 10 min. After quick PBS washes, mice were transcardially perfused with PBS and 4% PFA. For Torin1 treatment, drugs were incubated for 2 hrs, with reapplication 3 times to avoid drying. Brains were vibratome sectioned at 50 µm thickness, sections were incubated for 20 min with coextraction buffer (50 mM Tris-HCl, pH 7.5, 5 mM $MgCl_2$,25mM KCl, protease inhibitor (Roche), and 0.015% digitonin (Wako Chemicals #043-21376)). After three rinses with PBS, sections were incubated in blocking buffer (0.05% saponin, 10 mM glycine, and 5% fetal bovine serum in PBS) for 30min. Then, sections were incubated in blocking buffer with puromycin-647 antibody (Millipore MAB E343-AF647,1:1000), NeuN antibody (ab177487, 1:200) or Lamp1 (DSHB, #1D4B, 1:200) for 72 hours at 4°C. Sections were washed with PBS 3X 10 min, then incubated with secondary antibodies along with puromycin-647 at 4°C overnight, followed by PBS washes 3X 15 min.

STED imaging

STED imaging was performed as we previously described [114]. Briefly, human postmortem brain tissues underwent processing utilizing immunofluorescence staining and proximity labeling techniques outlined in the "Proximity labeling in brain tissues of human and mice" and "Immunofluorescence of fixed specimens" sections until the stage involving secondary antibodies and streptavidin labeling. The axonal spheroids and biotinylated proteins were labeled using STED-compatible secondary antibody Atto594 (Sigma-Aldrich) (1:100 dilution) and Atto647N-streptavidin (Sigma-Aldrich) (1:100 dilution). Subsequently, the tissues were mounted with Prolong Gold (ThermoFisher) following the user manual, and left in the dark at room temperature for 24 to 72 hours before imaging. STED imaging was carried out utilizing a Leica SP8 STED 3× equipped with a pulsed white light laser (SuperK Extreme EXW-12; NKT Photonics) for excitation and a 775 nm pulsed laser for depletion (Onefive Katana-08HP). The alignment of excitation and STED beams was accomplished using 200 nm Crimson Fluospheres (ThermoFisher; F8782). Sample imaging was performed using the following parameters: Sequence 1: 594 nm laser was at 1.15 uW. Sequence 2: 646 nm laser was at 6.4 uW. Sequence 3: 646 nm laser was at 34 uW. Sequence 4: 594 nm laser was 14 uW. Sequences 3 and 4: 775 nm STED laser was at 33 mW.

Samples for Focus Ion Beam/Scanning Electron Microscopy (FIBSEM)

Mice brains or fixed postmortem human brains were vibratome-sectioned into 50 µm thickness as described in the 'proximity labeling in brain tissue' section [4]. Trimmed tissue samples were fixed in 2.5% glutaraldehyde and 2% paraformaldehyde in 0.1M sodium cacodylate buffer pH 7.4 containing 2 mM calcium chloride for 1 hour, then rinsed in buffer and post fixed in 1% osmium tetroxide and 1.5% potassium ferrocyanide for another hour. After rinsing well, the samples were immersed in aqueous 1% thiocarbohydrazide for 30 minutes and then well rinsed. They were then placed in 1% osmium tetroxide in water for 1 hour at room temperature followed by rinsing in distilled water. An overnight en-bloc stain in aqueous 1% uranyl acetate was followed by

1306 rinsing in distilled water and then placed into warm lead aspartate and kept at 600 °C for 1 hour.
1307 After 1 hour of rinsing in distilled water, the samples were dehydrated through an ethanol series
1308 to 100%, followed by 100% propylene oxide. The samples were infiltrated with Durcupan
1309 (Electron Microscopy Sciences) resin over 2 days, then placed in silicone molds and baked at
1310 600 °C for at least 48 hours. The resin block was trimmed to a rough area of interest and the
1311 surface was cleanly cut. The entire pyramid was carefully removed with a fine blade and mounted
1312 on an aluminum stub using conductive carbon adhesive and silver paint (Electron Microscopy
1313 Sciences, Hatfield, PA, U.S.A,) then sputtered with approximately 15 nm Platinum/Palladium
1314 (80/20) using a Cressington HR sputter coating equipment (Ted Pella Inc. Redding CA) to reduce
1315 charging effects.
1316
1317 A dual beam FIBSEM (Zeiss CrossBeam 550) using a Gallium ion source was used to mill and SE2
1318 secondary electron detector was used to image the samples. Smart SEM (Zeiss, Jenna Germany)
1319 was used to set up initial parameters and to find the regions of interest by SEM images at 10 kV
1320 45 µm width and 30 µm height. The actual depth was 22 µm with 10nm/pixel and 10 nm per
1321 slice. A platinum protective layer was deposited at the ROI with the FIB (30 kV, 3 nA) to protect
1322 the structure and reduce charging. Milling and highlighting were done at 30 kV, 50 pA, with a
1323 carbon deposit (30kV 3nA). A course trench was milled (30 kv 30 nA) followed by fine milling (30
1324 kV 3nA) and for final acquisition, a cuboid the area of interest was milled at 30 kV and 300 pA.
1325 After milling each slice an image was taken by detecting backscattered electrons of a primary
1326 electron beam (acceleration voltage of 1.5 kV, imaging current of 2 nA, and aperture diameter of
1327 100 µm) with a pixel dwell time of 3µs Atlas5 (Zeiss) was used for preliminary SEM stack
1328 alignment and FIB/SEM image stacks were saved as Tiff and MRC files. The images were imported
1329 into Dragonfly software (ORS, Montreal Canada) for further alignment, segmentation and 3D
1330 video.
1331
1332 **FIBSEM image annotation and segmentation**
1333 Images from the Z-stack at different Z-locations were imported into APEER (ZEISS). Spheroids and
1334 plaques within the images were then manually annotated. After annotating 37 images, models
1335 were trained to predict each object. Then, individual spheroid and plaque segmentation models
1336 were downloaded and imported into Vision4D 4.1.0 (Arivis) for object segmentation. The entire
1337 Z-stack was then segmented in the analysis pipeline via the Deep Learning Segmenter operation
1338 with all the Z-stacks within the dataset. Next, non-specific and overlapping annotations were
1339 manually corrected using the "Draw Objects Tool." Object color and opacity were modified using
1340 the "Set Object Style" tab to show raw data. The Z-stack was then played using the Movie Player
1341 and recorded using Capture.
1342
1343 **Image analysis and quantification**
1344 All analyses were processed with FIJI (ImageJ) software, unless otherwise described.
1345 1) Quantification of PLD3 raw integrated fluorescence intensity in human brain: following PLD3
1346 immunolabeling, we compared the number and intensity of pixels corresponding to the PAAS
1347 halo versus the rest of the field of view, representing mostly neuronal soma and neuropil. For
1348 this, we used three AD postmortem brains which had been used for PAAS proteomics.
1349 Immunofluorescence staining of PLD3 and thioflavin S staining was performed followed by

1350 confocal imaging. Background autofluorescence signals were measured in unstained brain slices
1351 and subtracted from all subsequent image quantifications to better reflect true PLD3 signal.
1352 PAAS halos were manually circled, and the raw integrated intensity (RawInt) was measured. The
1353 RawInt was also measured for the whole field of view. The sum of RawInt derived from PAAS
1354 halos was subtracted from the RawInt from the whole field of view. By subtracting the halo
1355 RawInt from the total RawInt, we obtained a measurement of the PLD3 labeling outside of
1356 plaques which mainly consists of neuronal cell bodies, neuropil and any minimal background
1357 fluorescence.
1358
1359 2) p-mTOR S2448 fluorescence intensity measurement: in human AD or no/mild AD postmortem
1360 brains, each zoom 1 z-stack image, containing SMI312 positive axonal spheroids around amyloid
1361 plaques, were maximum projected. Then, SMI312 positive spheroid halos were circled, and mean
1362 fluorescence intensity of the p-mTOR S2448 channel was measured within the selected circle. In
1363 the same field of view, regions without spheroids were considered as background. Three such
1364 background regions were selected, circled and p-mTOR mean intensity was measured. The three
1365 "background" p-mTOR mean intensity from each field of view was averaged. Mean intensity (p-
1366 mTOR dystrophy halo) / mean intensity (p-mTOR background) was calculated to represent the p-
1367 mTOR expression level in each axonal spheroid halo. Three fields of view were quantified in each
1368 severe AD patient, and 1-3 fields of view were quantified in each no/mild AD patient. The
1369 averaged p-mTOR expression level in each patient was used for statistical analysis.
1370
1371 3) Measurement of the size of individual axon spheroids in human iPSC-derived neurons in the
1372 Torin1 treatment experiment: SMI312 was used to label spheroids, while ThioflavinS was used to
1373 label amyloid plaques. Tiling images were taken in each well from a 96-well plate and were
1374 maximum projected. For Torin1 treatment before amyloid plaque and spheroid formation,
1375 individual axonal spheroids were circled using the freehand tool on ImageJ, and the circle area
1376 was measured. The total number of axonal spheroid halos analyzed ranged from 50-150 within
1377 each tilling image. Two technical replicate wells were analyzed in each experiment and three
1378 batches of experiments were performed for quantification. For Torin1 treatment after amyloid
1379 plaque and spheroid formation, machine learning based image analysis software Aivia v12 (Leica)
1380 was used to quantify the size and number of spheroids and amyloid plaques, as well as axon
1381 density in an automated fashion. The pixel classifier tool was used to classify each channel.
1382
1383 4) Measurement of the percentage of axonal segments with spheroids in human iPSC-derived
1384 neurons in the Torin1 treatment experiment: The SMI312 staining revealed both axonal
1385 spheroids (the spheroid shape) and axons (the linear shape), therefore allowed us to recognize
1386 individual axon segments. To quantify axons with spheroids, we traced individual axon segments
1387 with linear and continuous signal across the z-stacks within the field of view. An axon with one
1388 or more spheroids formed was defined as axon with spheroid, whereas axon segments without
1389 spheroids observed within the z-stack, were defined as axons without spheroids. In **Figure 6L**, the
1390 percentage of axons with spheroids was calculated by comparing the number of axonal segment
1391 with spheroids over the total number of axonal segments that were observed within the field of
1392 view.
1393

1394 5) Measurement of human neuron cell body size with or without Torin1 treatment: iPSC co-
1395 cultures were infected by AAV2-CB7-GFP (Addgene#105542) at titer ~7x10^9 vg/mL one week
1396 before Torin1 and amyloid beta treatment. Cells were stained with NeuN and GFP antibodies.
1397 Large field tilling imaging was performed in each well. Tilling images were maximum projected
1398 and neurons with both NeuN and GFP positive signals were measured by size, using the freehand
1399 tool in ImageJ. Three technical replicate wells were analyzed in each experiment and two batches
1400 of experiments were done for quantification.
1401
1402 6) Individual axonal spheroid size measurement in the AAV9-hSyn-cre-2a-tdT infected *Mtor*-flox-
1403 5XFAD mice: anti-Lamp1 antibody was used for immunofluorescence staining to showcase the
1404 spheroid halo around amyloid plaques, ThioflavinS was used to label amyloid plaques, and anti-
1405 RFP antibody was used to reveal the tdTomato expression in infected neurons. Tilling images
1406 were taken at the somatosensory cortex of each animal. Three serial brain sections were used
1407 for tilling imaging for each mouse. An individual spheroid was counted when it was both
1408 tdTomato and Lamp1 positive. The individual spheroid size was measured using the freehand
1409 tool in ImageJ to circle the outline of spheroids, where it had the maximum diameter, followed
1410 by measurement of the circled area. The total number of axonal spheroid halo analyzed ranged
1411 from 50-150 in each tilling image.
1412
1413 7) Measurement of spheroid halo size in the AAV-PHPeB infected *Mtor*-flox-5XFAD experiment:
1414 anti-Lamp1 antibody was used for immunofluorescence staining to showcase the spheroid halo
1415 around amyloid plaque, ThioflavinS was used to label amyloid plaques. Tilling images were taken
1416 at the somatosensory cortex of each animal. Three serial brain sections were used for tilling
1417 imaging for each mouse. A customized ImageJ macro was used to segment individual Lamp1
1418 positive spheroid halos and amyloid plaques. Using a customized MATLAB program, the
1419 segmented images were processed to measure the area of individual spheroid halos and amyloid
1420 plaque area, automatically. The spheroid halo area was excluding the area in the center occupied
1421 by the amyloid plaque. The number of axonal spheroid halos and amyloid plaques analyzed
1422 ranged from 30 to 70 in each tilling image from the *Mtor*-flox-5XFAD experiment.
1423
1424 8) Measurement of RNA signals within axonal spheroids: ImageJ free hand tool was used to circle
1425 axonal spheroid structures labeled by Atto-647 NHS ester, and fluorescence intensity from PolyA
1426 probe channel, or negative control probe channel was measured. For measuring puromycin
1427 signals within axonal spheroids or neuronal cell bodies, similarly, ImageJ free hand tool was used
1428 to circle axonal spheroid or cell bodies labeled by Lamp1 or NeuN, respectively, and fluorescence
1429 intensity from puromycin channel was measured.
1430
1431 9) Measurement of NeuN positive neuronal cell soma area in AAV-PHPeB infected *Mtor*-flox-
1432 5XFAD mice: A customized CellProfiler program was used for automated measurement. Briefly,
1433 tilling images were taken from one hemisphere of the somatosensory cortex. Tilling images were
1434 maximum projected before importing them into CellProfiler (Broad Institute). The NeuN channel
1435 was set as the primary object and was used as the marker for size measurement. Three tilling
1436 images were taken from three brain sections of each animal. Three animals were used in each
1437 group.

10) Investigation of mTOR heterozygous knockout downstream signaling effectors in mTOR-floxed-5XFAD mice: Similarly, a customized CellProfiler program was used for automated measurement. Tilling images were maximum projected before analysis. To analyze fluorescence intensity in the nuclei, we used DAPI staining as the primary object and measured signals from the NeuN positive cells. To measure fluorescence intensity from the cell bodies, the NeuN channel was set as the primary object and was used as the marker for fluorescence intensity measurement. We compared mice injected with PHPeB-hSyn-cre-GFP viruses, with those injected with control viruses PHPeB-CAG-GFP. The littermates and sex were paired for comparison. Immunofluorescence intensity of TFEB was measured in neuronal nuclei, while LC3B, P-p70S6K Thr389 and p70S6K were measured in neuronal soma in an automated fashion.

Statistical analysis

No statistical power analysis was used to determine sample sizes, but our sample sizes were similar to those generally employed in the field. All samples were included for analysis. Excel (Microsoft), Prism (GraphPad), Qlucore Omics Explorer v3.6 (Qlucore AB, Lund, Sweden), CellProfiler v4.2.1 (Broad Institute), MATLAB and RStudio (4.0.2) were used for data analysis and plotting. Statistical methods used were described in the figure legend of each relevant panel.

DATA AND CODE AVAILABILITY

Raw proteomics data is provided in **Table S1**. The mass spectrometry proteomics data have been deposited to the ProteomeXchange Consortium via the PRIDE partner repository with the dataset identifier xxx. Reviewer account details: Username: xxx, Password: xxx). The Lamp1 dataset is under the identifier xxx, username: xxx, password: xxx. For sample information see **Table S3**.

Custom codes for FIJI and MATLAB were deposited at GitHub (https://github.com/PaulYJ/Axon-spheroid) as we previously described [4].

The Python code for the analysis of calcium imaging data can be accessed at the following location: https://github.com/ShawnQin/calcium_trace.

The code for the analysis of STED imaging data can be accessed at the following location: https://github.com/bewersdorflab/Yifei-Lukas-Collab.

1471 **REFERENCE**
1472

1473 1. Knopman, D.S., et al., *Alzheimer disease.* Nat Rev Dis Primers, 2021. **7**(1): p. 33.
1474 2. Spires-Jones, T.L. and B.T. Hyman, *The intersection of amyloid beta and tau at synapses*
1475 *in Alzheimer's disease.* Neuron, 2014. **82**(4): p. 756-71.
1476 3. Tsai, J., et al., *Fibrillar amyloid deposition leads to local synaptic abnormalities and*
1477 *breakage of neuronal branches.* Nat Neurosci, 2004. **7**(11): p. 1181-3.
1478 4. Yuan, P., et al., *PLD3 affects axonal spheroids and network defects in Alzheimer's*
1479 *disease.* Nature, 2022. **612**(7939): p. 328-337.
1480 5. Adalbert, R., et al., *Severely dystrophic axons at amyloid plaques remain continuous and*
1481 *connected to viable cell bodies.* Brain, 2009. **132**(Pt 2): p. 402-16.
1482 6. Nardocci, N. and G. Zorzi, *Axonal dystrophies.* Handb Clin Neurol, 2013. **113**: p. 1919-24.
1483 7. Tourtellotte, W.G. and G.W. Van Hoesen, *The axonal origin of a subpopulation of*
1484 *dystrophic neurites in Alzheimer's disease.* Neurosci Lett, 1991. **129**(1): p. 11-6.
1485 8. Vickers, J.C., et al., *Dystrophic neurite formation associated with age-related beta*
1486 *amyloid deposition in the neocortex: clues to the genesis of neurofibrillary pathology.*
1487 Exp Neurol, 1996. **141**(1): p. 1-11.
1488 9. Yasuhara, O., et al., *Two types of dystrophic neurites in senile plaques of Alzheimer*
1489 *disease and elderly non-demented cases.* Neurosci Lett, 1994. **171**(1-2): p. 73-6.
1490 10. Alzheimer, A., et al., *An English translation of Alzheimer's 1907 paper, "Uber eine*
1491 *eigenartige Erkankung der Hirnrinde".* Clin Anat, 1995. **8**(6): p. 429-31.
1492 11. McKee, A.C., K.S. Kosik, and N.W. Kowall, *Neuritic pathology and dementia in*
1493 *Alzheimer's disease.* Ann Neurol, 1991. **30**(2): p. 156-65.
1494 12. Kolaric, K.V., et al., *Focal axonal swellings and associated ultrastructural changes*
1495 *attenuate conduction velocity in central nervous system axons: a computer modeling*
1496 *study.* Physiol Rep, 2013. **1**(3): p. e00059.
1497 13. Wu, Y.T., K. Gilpin, and A. Adnan, *Effects of Focal Axonal Swelling Level on the Action*
1498 *Potential Signal Transmission.* J Comput Neurosci, 2020. **48**(3): p. 253-263.
1499 14. Gowrishankar, S., et al., *Massive accumulation of luminal protease-deficient axonal*
1500 *lysosomes at Alzheimer's disease amyloid plaques.* Proc Natl Acad Sci U S A, 2015.
1501 **112**(28): p. E3699-708.
1502 15. Nixon, R.A., et al., *Extensive involvement of autophagy in Alzheimer disease: an immuno-*
1503 *electron microscopy study.* J Neuropathol Exp Neurol, 2005. **64**(2): p. 113-22.
1504 16. Lee, S., Y. Sato, and R.A. Nixon, *Lysosomal proteolysis inhibition selectively disrupts*
1505 *axonal transport of degradative organelles and causes an Alzheimer's-like axonal*
1506 *dystrophy.* J Neurosci, 2011. **31**(21): p. 7817-30.
1507 17. Wolfe, D.M., et al., *Autophagy failure in Alzheimer's disease and the role of defective*
1508 *lysosomal acidification.* European Journal of Neuroscience, 2013. **37**(12): p. 1949-1961.
1509 18. Stokin, G.B., et al., *Axonopathy and transport deficits early in the pathogenesis of*
1510 *Alzheimer's disease.* Science, 2005. **307**(5713): p. 1282-8.
1511 19. Pigino, G., et al., *Disruption of fast axonal transport is a pathogenic mechanism for*
1512 *intraneuronal amyloid beta.* Proc Natl Acad Sci U S A, 2009. **106**(14): p. 5907-12.

1513 20. Sadleir, K.R., et al., *Presynaptic dystrophic neurites surrounding amyloid plaques are*
1514 *sites of microtubule disruption, BACE1 elevation, and increased Abeta generation in*
1515 *Alzheimer's disease.* Acta Neuropathol, 2016. **132**(2): p. 235-56.
1516 21. Roney, J.C., et al., *Lipid-mediated motor-adaptor sequestration impairs axonal lysosome*
1517 *delivery leading to autophagic stress and dystrophy in Niemann-Pick type C.* Dev Cell,
1518 2021. **56**(10): p. 1452-1468 e8.
1519 22. Yong, Y., et al., *Axonal spheroids in neurodegeneration.* Mol Cell Neurosci, 2021. **117**: p.
1520 103679.
1521 23. Sanchez-Varo, R., et al., *Abnormal accumulation of autophagic vesicles correlates with*
1522 *axonal and synaptic pathology in young Alzheimer's mice hippocampus.* Acta
1523 Neuropathol, 2012. **123**(1): p. 53-70.
1524 24. Essuman, K., et al., *The SARM1 Toll/Interleukin-1 Receptor Domain Possesses Intrinsic*
1525 *NAD(+) Cleavage Activity that Promotes Pathological Axonal Degeneration.* Neuron,
1526 2017. **93**(6): p. 1334-1343 e5.
1527 25. Gerdts, J., et al., *SARM1 activation triggers axon degeneration locally via NAD(+)*
1528 *destruction.* Science, 2015. **348**(6233): p. 453-7.
1529 26. He, Z., et al., *Amyloid-beta plaques enhance Alzheimer's brain tau-seeded pathologies by*
1530 *facilitating neuritic plaque tau aggregation.* Nat Med, 2018. **24**(1): p. 29-38.
1531 27. Knowles, R.B., et al., *Plaque-induced neurite abnormalities: implications for disruption of*
1532 *neural networks in Alzheimer's disease.* Proc Natl Acad Sci U S A, 1999. **96**(9): p. 5274-9.
1533 28. Vickers, J.C., et al., *Axonopathy and cytoskeletal disruption in degenerative diseases of*
1534 *the central nervous system.* Brain Res Bull, 2009. **80**(4-5): p. 217-23.
1535 29. Yong, Y., et al., *Regulation of degenerative spheroids after injury.* Sci Rep, 2020. **10**(1): p.
1536 15472.
1537 30. Wang, Y., et al., *TREM2-mediated early microglial response limits diffusion and toxicity*
1538 *of amyloid plaques.* J Exp Med, 2016. **213**(5): p. 667-75.
1539 31. Yuan, P., et al., *TREM2 Haplodeficiency in Mice and Humans Impairs the Microglia*
1540 *Barrier Function Leading to Decreased Amyloid Compaction and Severe Axonal*
1541 *Dystrophy.* Neuron, 2016. **92**(1): p. 252-264.
1542 32. Condello, C., et al., *Microglia constitute a barrier that prevents neurotoxic protofibrillar*
1543 *Abeta42 hotspots around plaques.* Nat Commun, 2015. **6**: p. 6176.
1544 33. Sardiello, M., et al., *A gene network regulating lysosomal biogenesis and function.*
1545 Science, 2009. **325**(5939): p. 473-7.
1546 34. Manning, B.D. and A. Toker, *AKT/PKB Signaling: Navigating the Network.* Cell, 2017.
1547 **169**(3): p. 381-405.
1548 35. Saxton, R.A. and D.M. Sabatini, *mTOR Signaling in Growth, Metabolism, and Disease.*
1549 Cell, 2017. **168**(6): p. 960-976.
1550 36. Branon, T.C., et al., *Efficient proximity labeling in living cells and organisms with TurboID.*
1551 Nat Biotechnol, 2018. **36**(9): p. 880-887.
1552 37. Rhee, H.W., et al., *Proteomic mapping of mitochondria in living cells via spatially*
1553 *restricted enzymatic tagging.* Science, 2013. **339**(6125): p. 1328-1331.
1554 38. Roux, K.J., et al., *A promiscuous biotin ligase fusion protein identifies proximal and*
1555 *interacting proteins in mammalian cells.* J Cell Biol, 2012. **196**(6): p. 801-10.

1556 39. Uezu, A., et al., *Identification of an elaborate complex mediating postsynaptic inhibition.*
1557 Science, 2016. **353**(6304): p. 1123-9.
1558 40. Mathew, B., et al., *Deciphering Spatial Protein-Protein Interactions in Brain Using*
1559 *Proximity Labeling.* Mol Cell Proteomics, 2022. **21**(11): p. 100422.
1560 41. Li, J., et al., *Cell-Surface Proteomic Profiling in the Fly Brain Uncovers Wiring Regulators.*
1561 Cell, 2020. **180**(2): p. 373-386 e15.
1562 42. Loh, K.H., et al., *Proteomic Analysis of Unbounded Cellular Compartments: Synaptic*
1563 *Clefts.* Cell, 2016. **166**(5): p. 1295-1307 e21.
1564 43. Bar, D.Z., et al., *Biotinylation by antibody recognition-a method for proximity labeling.*
1565 Nat Methods, 2018. **15**(2): p. 127-133.
1566 44. Killinger, B.A., et al., *In situ proximity labeling identifies Lewy pathology molecular*
1567 *interactions in the human brain.* Proc Natl Acad Sci U S A, 2022. **119**(5).
1568 45. Hashimoto, N., et al., *Proteomic analysis of ganglioside-associated membrane*
1569 *molecules: substantial basis for molecular clustering.* Proteomics, 2012. **12**(21): p. 3154-
1570 63.
1571 46. Li, X.W., et al., *New insights into the DT40 B cell receptor cluster using a proteomic*
1572 *proximity labeling assay.* J Biol Chem, 2014. **289**(21): p. 14434-47.
1573 47. Nackenoff, A.G., et al., *PLD3 is a neuronal lysosomal phospholipase D associated with*
1574 *beta-amyloid plaques and cognitive function in Alzheimer's disease.* PLoS Genet, 2021.
1575 **17**(4): p. e1009406.
1576 48. Satoh, J., et al., *PLD3 is accumulated on neuritic plaques in Alzheimer's disease brains.*
1577 Alzheimers Res Ther, 2014. **6**(9): p. 70.
1578 49. Gonzalez, A.C., et al., *Unconventional Trafficking of Mammalian Phospholipase D3 to*
1579 *Lysosomes.* Cell Rep, 2018. **22**(4): p. 1040-1053.
1580 50. Cruchaga, C., et al., *Rare coding variants in the phospholipase D3 gene confer risk for*
1581 *Alzheimer's disease.* Nature, 2014. **505**(7484): p. 550-554.
1582 51. Gusel'nikova, V.V. and D.E. Korzhevskiy, *NeuN As a Neuronal Nuclear Antigen and*
1583 *Neuron Differentiation Marker.* Acta Naturae, 2015. **7**(2): p. 42-7.
1584 52. Liu, G.Y. and D.M. Sabatini, *mTOR at the nexus of nutrition, growth, ageing and disease.*
1585 Nat Rev Mol Cell Biol, 2020. **21**(4): p. 183-203.
1586 53. Martins, I.J., et al., *Apolipoprotein E, cholesterol metabolism, diabetes, and the*
1587 *convergence of risk factors for Alzheimer's disease and cardiovascular disease.* Mol
1588 Psychiatry, 2006. **11**(8): p. 721-36.
1589 54. Masuda, T., et al., *Novel Hexb-based tools for studying microglia in the CNS.* Nat
1590 Immunol, 2020. **21**(7): p. 802-815.
1591 55. Zhang, Y., et al., *Purification and Characterization of Progenitor and Mature Human*
1592 *Astrocytes Reveals Transcriptional and Functional Differences with Mouse.* Neuron,
1593 2016. **89**(1): p. 37-53.
1594 56. Zhang, Y., et al., *Rapid single-step induction of functional neurons from human*
1595 *pluripotent stem cells.* Neuron, 2013. **78**(5): p. 785-98.
1596 57. Bassil, R., et al., *Improved modeling of human AD with an automated culturing platform*
1597 *for iPSC neurons, astrocytes and microglia.* Nat Commun, 2021. **12**(1): p. 5220.
1598 58. Ballatore, C., V.M. Lee, and J.Q. Trojanowski, *Tau-mediated neurodegeneration in*
1599 *Alzheimer's disease and related disorders.* Nat Rev Neurosci, 2007. **8**(9): p. 663-72.

1600 59. Thoreen, C.C., et al., *An ATP-competitive mammalian target of rapamycin inhibitor*
1601 *reveals rapamycin-resistant functions of mTORC1.* J Biol Chem, 2009. **284**(12): p. 8023-
1602 32.
1603 60. Zhao, J., et al., *mTOR inhibition activates overall protein degradation by the ubiquitin*
1604 *proteasome system as well as by autophagy.* Proc Natl Acad Sci U S A, 2015. **112**(52): p.
1605 15790-7.
1606 61. Risson, V., et al., *Muscle inactivation of mTOR causes metabolic and dystrophin defects*
1607 *leading to severe myopathy.* J Cell Biol, 2009. **187**(6): p. 859-74.
1608 62. Poulopoulos, A., et al., *Subcellular transcriptomes and proteomes of developing axon*
1609 *projections in the cerebral cortex.* Nature, 2019. **565**(7739): p. 356-360.
1610 63. Terenzio, M., et al., *Locally translated mTOR controls axonal local translation in nerve*
1611 *injury.* Science, 2018. **359**(6382): p. 1416-1421.
1612 64. Hyman, B.T., et al., *National Institute on Aging-Alzheimer's Association guidelines for the*
1613 *neuropathologic assessment of Alzheimer's disease.* Alzheimers Dement, 2012. **8**(1): p.
1614 1-13.
1615 65. Su, J.H., B.J. Cummings, and C.W. Cotman, *Identification and distribution of axonal*
1616 *dystrophic neurites in Alzheimer's disease.* Brain Res, 1993. **625**(2): p. 228-37.
1617 66. Drummond, E., et al., *The amyloid plaque proteome in early onset Alzheimer's disease*
1618 *and Down syndrome.* Acta Neuropathol Commun, 2022. **10**(1): p. 53.
1619 67. Drummond, E., et al., *Proteomic differences in amyloid plaques in rapidly progressive*
1620 *and sporadic Alzheimer's disease.* Acta Neuropathol, 2017. **133**(6): p. 933-954.
1621 68. Liao, L., et al., *Proteomic characterization of postmortem amyloid plaques isolated by*
1622 *laser capture microdissection.* J Biol Chem, 2004. **279**(35): p. 37061-8.
1623 69. Dovas, A. and J.R. Couchman, *RhoGDI: multiple functions in the regulation of Rho family*
1624 *GTPase activities.* Biochem J, 2005. **390**(Pt 1): p. 1-9.
1625 70. Garcia-Mata, R., E. Boulter, and K. Burridge, *The 'invisible hand': regulation of RHO*
1626 *GTPases by RHOGDIs.* Nat Rev Mol Cell Biol, 2011. **12**(8): p. 493-504.
1627 71. Torres, M., et al., *Defective lysosomal proteolysis and axonal transport are early*
1628 *pathogenic events that worsen with age leading to increased APP metabolism and*
1629 *synaptic Abeta in transgenic APP/PS1 hippocampus.* Mol Neurodegener, 2012. **7**: p. 59.
1630 72. Yang, Y., et al., *Disruption of Tmem30a results in cerebellar ataxia and degeneration of*
1631 *Purkinje cells.* Cell Death Dis, 2018. **9**(9): p. 899.
1632 73. Toapanta, F.R. and T.M. Ross, *Complement-mediated activation of the adaptive immune*
1633 *responses: role of C3d in linking the innate and adaptive immunity.* Immunol Res, 2006.
1634 **36**(1-3): p. 197-210.
1635 74. Barbu, A., et al., *The role of complement factor C3 in lipid metabolism.* Mol Immunol,
1636 2015. **67**(1): p. 101-7.
1637 75. Garcia-Arguinzonis, M., et al., *Alternative C3 Complement System: Lipids and*
1638 *Atherosclerosis.* Int J Mol Sci, 2021. **22**(10).
1639 76. Stoltzner, S.E., et al., *Temporal accrual of complement proteins in amyloid plaques in*
1640 *Down's syndrome with Alzheimer's disease.* Am J Pathol, 2000. **156**(2): p. 489-99.
1641 77. Chen, S., R.C. Frederickson, and K.R. Brunden, *Neuroglial-mediated*
1642 *immunoinflammatory responses in Alzheimer's disease: complement activation and*
1643 *therapeutic approaches.* Neurobiol Aging, 1996. **17**(5): p. 781-7.

1644 78. Eikelenboom, P., et al., *Distribution pattern and functional state of complement proteins*
1645 *and alpha 1-antichymotrypsin in cerebral beta/A4 deposits in Alzheimer's disease.* Res
1646 Immunol, 1992. **143**(6): p. 617-20.
1647 79. Kim, Y.M., et al., *mTORC1 phosphorylates UVRAG to negatively regulate autophagosome*
1648 *and endosome maturation.* Mol Cell, 2015. **57**(2): p. 207-18.
1649 80. Park, K.K., et al., *Promoting axon regeneration in the adult CNS by modulation of the*
1650 *PTEN/mTOR pathway.* Science, 2008. **322**(5903): p. 963-6.
1651 81. Peterson, T.R., et al., *mTOR complex 1 regulates lipin 1 localization to control the SREBP*
1652 *pathway.* Cell, 2011. **146**(3): p. 408-20.
1653 82. Menon, D., et al., *Lipid sensing by mTOR complexes via de novo synthesis of phosphatidic*
1654 *acid.* J Biol Chem, 2017. **292**(15): p. 6303-6311.
1655 83. Castellano, B.M., et al., *Lysosomal cholesterol activates mTORC1 via an SLC38A9-*
1656 *Niemann-Pick C1 signaling complex.* Science, 2017. **355**(6331): p. 1306-1311.
1657 84. Wong, H.H., A.J. Watt, and P.J. Sjostrom, *Synapse-specific burst coding sustained by local*
1658 *axonal translation.* Neuron, 2023.
1659 85. Lie, P.P.Y., et al., *Axonal transport of late endosomes and amphisomes is selectively*
1660 *modulated by local Ca(2+) efflux and disrupted by PSEN1 loss of function.* Sci Adv, 2022.
1661 **8**(17): p. eabj5716.
1662 86. Meyer-Luehmann, M., et al., *Rapid appearance and local toxicity of amyloid-beta*
1663 *plaques in a mouse model of Alzheimer's disease.* Nature, 2008. **451**(7179): p. 720-4.
1664 87. Goltsev, Y., et al., *Deep Profiling of Mouse Splenic Architecture with CODEX Multiplexed*
1665 *Imaging.* Cell, 2018. **174**(4): p. 968-981 e15.
1666 88. Satoh, J.I., et al., *Alzheimer's disease pathology in Nasu-Hakola disease brains.*
1667 Intractable Rare Dis Res, 2018. **7**(1): p. 32-36.
1668 89. Foulds, N., et al., *Adult-Onset Leukoencephalopathy with Axonal Spheroids and*
1669 *Pigmented Glia Caused by a Novel R782G Mutation in CSF1R.* Sci Rep, 2015. **5**: p. 10042.
1670 90. DiFiglia, M., et al., *Aggregation of huntingtin in neuronal intranuclear inclusions and*
1671 *dystrophic neurites in brain.* Science, 1997. **277**(5334): p. 1990-3.
1672 91. Sharoar, M.G., et al., *Sequential formation of different layers of dystrophic neurites in*
1673 *Alzheimer's brains.* Mol Psychiatry, 2019. **24**(9): p. 1369-1382.
1674 92. Shi, Q., et al., *RTN1 and RTN3 protein are differentially associated with senile plaques in*
1675 *Alzheimer's brains.* Sci Rep, 2017. **7**(1): p. 6145.
1676 93. Masliah, E., et al., *An antibody against phosphorylated neurofilaments identifies a subset*
1677 *of damaged association axons in Alzheimer's disease.* Am J Pathol, 1993. **142**(3): p. 871-
1678 82.
1679 94. Hoffman, G.E., et al., *Transcriptional signatures of schizophrenia in hiPSC-derived NPCs*
1680 *and neurons are concordant with post-mortem adult brains.* Nat Commun, 2017. **8**(1): p.
1681 2225.
1682 95. Oakley, H., et al., *Intraneuronal beta-amyloid aggregates, neurodegeneration, and*
1683 *neuron loss in transgenic mice with five familial Alzheimer's disease mutations: potential*
1684 *factors in amyloid plaque formation.* J Neurosci, 2006. **26**(40): p. 10129-40.
1685 96. Mathys, H., et al., *Single-cell transcriptomic analysis of Alzheimer's disease.* Nature,
1686 2019. **570**(7761): p. 332-337.

1687 97. Uhlen, M., et al., *Proteomics. Tissue-based map of the human proteome.* Science, 2015.
1688 **347**(6220): p. 1260419.
1689 98. Ashburner, M., et al., *Gene ontology: tool for the unification of biology. The Gene*
1690 *Ontology Consortium.* Nat Genet, 2000. **25**(1): p. 25-9.
1691 99. Gene Ontology, C., *The Gene Ontology resource: enriching a GOld mine.* Nucleic Acids
1692 Res, 2021. **49**(D1): p. D325-D334.
1693 100. Raudvere, U., et al., *g:Profiler: a web server for functional enrichment analysis and*
1694 *conversions of gene lists (2019 update).* Nucleic Acids Res, 2019. **47**(W1): p. W191-
1695 W198.
1696 101. Chen, J., et al., *ToppGene Suite for gene list enrichment analysis and candidate gene*
1697 *prioritization.* Nucleic Acids Res, 2009. **37**(Web Server issue): p. W305-11.
1698 102. Shannon, P., et al., *Cytoscape: a software environment for integrated models of*
1699 *biomolecular interaction networks.* Genome Res, 2003. **13**(11): p. 2498-504.
1700 103. Kramer, A., et al., *Causal analysis approaches in Ingenuity Pathway Analysis.*
1701 Bioinformatics, 2014. **30**(4): p. 523-30.
1702 104. Subramanian, A., et al., *Gene set enrichment analysis: a knowledge-based approach for*
1703 *interpreting genome-wide expression profiles.* Proc Natl Acad Sci U S A, 2005. **102**(43): p.
1704 15545-50.
1705 105. Merico, D., et al., *Enrichment map: a network-based method for gene-set enrichment*
1706 *visualization and interpretation.* PLoS One, 2010. **5**(11): p. e13984.
1707 106. Kucera, M., et al., *AutoAnnotate: A Cytoscape app for summarizing networks with*
1708 *semantic annotations.* F1000Res, 2016. **5**: p. 1717.
1709 107. Li, A., et al., *Using the dCas9-KRAB system to repress gene expression in hiPSC-derived*
1710 *NGN2 neurons.* STAR Protoc, 2021. **2**(2): p. 100580.
1711 108. Ho, S.M., et al., *Rapid Ngn2-induction of excitatory neurons from hiPSC-derived neural*
1712 *progenitor cells.* Methods, 2016. **101**: p. 113-24.
1713 109. Wang, M., et al., *Transformative Network Modeling of Multi-omics Data Reveals*
1714 *Detailed Circuits, Key Regulators, and Potential Therapeutics for Alzheimer's Disease.*
1715 Neuron, 2021. **109**(2): p. 257-272 e14.
1716 110. Li, X., et al., *Real-time denoising enables high-sensitivity fluorescence time-lapse imaging*
1717 *beyond the shot-noise limit.* Nat Biotechnol, 2023. **41**(2): p. 282-292.
1718 111. Murakami, M., et al., *mTOR is essential for growth and proliferation in early mouse*
1719 *embryos and embryonic stem cells.* Mol Cell Biol, 2004. **24**(15): p. 6710-8.
1720 112. M'Saad, O. and J. Bewersdorf, *Light microscopy of proteins in their ultrastructural*
1721 *context.* Nat Commun, 2020. **11**(1): p. 3850.
1722 113. Biever, A., et al., *Monosomes actively translate synaptic mRNAs in neuronal processes.*
1723 Science, 2020. **367**(6477).
1724 114. Schroeder, L.K., et al., *Dynamic nanoscale morphology of the ER surveyed by STED*
1725 *microscopy.* J Cell Biol, 2019. **218**(1): p. 83-96.
1726 115. Salgado, C.M., et al., *Noise Versus Outliers*, in *Secondary Analysis of Electronic Health*
1727 *Records*. 2016: Cham (CH). p. 163-83.

1728

Acknowledgments

This project was supported by National Institute of Health grants: RF1AG058257, R01NS115544, R01NS111961 (J.G.), a Cure Alzheimer's Fund Research Grant (J.G.), a Yale/NIDA Neuroproteomics Center Pilot Project Grant 2019 (Y.C.), a BrightFocus Foundation Postdoctoral Fellowship Program in Alzheimer's disease Research (A2021003F) (Y.C.), a Yale ADRC Research Scholar Award (Y.C.), an Alzheimer's Association Research Fellowship (23AARF-1020552) (Y.C.), a Yale ADRC grant P30 AG066508 (A.C.N), and the following grants R01AG068030, RF1AG065926, R56AG071291 to K.J.B . We thank Drs. Kenneth Williams, Shannon Leslie, Bobby Mathew and the Yale/NIDA Neuroproteomics Center (P30 DA018343), for providing experimental design advice, technical support and funding opportunities. We thank staff from the Keck MS & Proteomics Resource at the Yale School of Medicine for processing the LC MS/MS experiments. We also thank the Keck MS & Proteomics Resource at the Yale School of Medicine for providing the necessary mass spectrometers and the accompany biotechnology tools funded in part by the Yale School of Medicine and by the Office of The Director, National Institutes of Health (S10OD02365101A1, S10OD019967, and S10OD018034). The funders had no role in study design, data collection and analysis, decision to publish, or preparation of the manuscript. I.P.S and E.P. were supported by EMBL-EBI Core funding. We thank Dr. Anita Huttner and the Yale ADRC (P30 AG066508) for providing human postmortem AD and control brain tissues. Additional MCI and AD brain tissue was provided by the Banner Sun Health Research Institute Brain and Body Donation Program of Sun City, Arizona, supported by the NINDS (U24 NS072026), the NIA (P30 AG19610), the Arizona Department of Health Services (contract 211002), and the Arizona Biomedical Research Commission (contracts 4001, 0011, 05-901 and 1001). We thank Drs. Nur-Taz Rahman and Rolando Garcia Milian from the Yale Medical Library Bioinformatics Support Program for providing advice and technical support for bioinformatics analysis. We thank Dr. Xinran Liu, Ms. Morven Graham and the Center for Cellular and Molecular Imaging Electron Microscopy Facility at Yale Medical School for assistance with the electron microscopy experiments (NSF Major Instrument grant 1725480). We thank Drs. Peng Yuan, Lei Tong and Mengyang Zhang for providing MATLAB and FIJI imageJ coding for plaque and axonal spheroid quantification. We thank Dr. Mengyang Zhang for generating the AAV2-CMV-LAMP-GFP viruses. We thank Drs. Jelena Platisa, Peter O'Brien, Vincent Pieribone, Ilona Kondratiuk, Dhrubajyoti Chowdhury, Thomas Biederer, Shengnan Qiao, Yao Xue and Jimmy Zhou for their generous help and critical advice on the calcium imaging experiments. Calcium imaging was performed using dragonfly spinning disk confocal from the Biederer lab, supported by grant NIH R01 DA018928 (to T.B.). We thank Drs. Teresa Spano and Erin Schuman for their generous help and critical advice on the *in vivo* puromycylation experiments. We thank Dr. Philip Coish for the critical reading of this manuscript. We created schematic figures with BioRender.com.

Author contributions

Y.C. and J.G. conceived and designed the study. Y.C. performed proximity labeling experiments, Y.C., R.W., M.S.M., T.T.L., S. B. and A.C.N. designed protein extraction, enrichment and digestion protocol, Y.C. performed protein extraction, enrichment and western blotting, J.K., R.W., S.B. and T.T.L. performed LC-MS-MS, protein mapping and searching, Y.C. performed proteomics data analysis, Y.C., I.P.S and E.P performed bioinformatics analysis, A.C.N. supervised the proteomics experiments and analysis; L.A.F. and Y.C. performed STED imaging, L.A.F., T.H. and Y.C. performed

STED imaging analysis; Y.C., L.T., and L.S. performed calcium imaging in iPSC model, L.T., S.Q. performed calcium imaging data analysis; A.H. performed pathological evaluation of human brain specimens and provided the tissues; Y.C. and T.H. performed immunofluorescence and confocal imaging; T.H. performed immunofluorescence quantification of newly identified proteomic hits and automated tilling images analysis; Y.C., P.L.C. and K.J.B. established the human iPSC-derived neuron-astrocyte co-culture protocol, P.L.C. performed lentivirus packaging, Y.C. performed AD human neuron-astrocyte co-culture, K.J.B. supervised the human neuron-astrocyte co-culture experiment; Y.C. performed mTOR inhibition in transgenic mice, Y.C., T.H., Z.T., A.B. and K.T. performed quantifications, Y.C. and T.H. performed statistics analysis; H. G. annotated FIBSEM video; Y.C. and J.G. prepared the manuscript. J.G. supervised the study.

Declaration of interests

The authors declare no competing interests.

1784 **SUPPLEMENTARY DATA**

A. Human brain samples (frontal cortex) from Yale ADRC.

Brain Bank	AD/Control	ID	Age (years)	Sex	PMI (h)	AD neuropathological change	AD neuropathological level	Application
Yale ADRC	AD	40-0074	58	female	19	A2, B3, C3	intermediate AD	proteomics, IF
Yale ADRC	AD	40-0036	96	female	7	A2, B3, C2	intermediate AD	proteomics, IF
Yale ADRC	AD	400028	82	male	20	A3, B3, C3	high AD	proteomics, IF
Yale ADRC	AD	400126	75	female	3	A3, B3, C3	high AD	IF
Yale ADRC	AD	400032	84	male	22	A2, B3, C3	intermediate AD	IF
Yale ADRC	AD	400082	70	male	23	A2, B2, C3	intermediate AD	IF
Yale ADRC	AD	400192	83	female	19	A3, B3, C3	high AD	IF
Yale ADRC	AD	400098	83	female	17	A2, B3, C2	intermediate AD	IF
Yale ADRC	Control	400116	83	male	22	A0, B1, C0	NOT AD	proteomics, IF
Yale ADRC	Control	400070	84	male	27	A0, B1, C0	NOT AD	IF

B. Human brain samples (frontal cortex) from Banner Institute.

Brain Bank	AD/Control	ID	Age (years)	Sex	PMI (h)	PlaqueTotal	Plaque density	Braak score	NIA-R	AD neuropathological level	Application
Banner	AD	11-35	93	female	2.83	15	frequent	V	high	intermediate to high AD	IF
Banner	AD	12-27	89	female	2.7	15	frequent	VI	high	intermediate to high AD	IF
Banner	AD	12-49	63	male	5.17	14.5	frequent	VI	high	intermediate to high AD	IF
Banner	AD	13-42	80	male	3	14	frequent	VI	high	intermediate to high AD	IF
Banner	AD	13-54	85	female	3.42	14	frequent	VI	high	intermediate to high AD	IF
Banner	AD	13-75	77	male	3.62	15	frequent	VI	high	intermediate to high AD	IF
Banner	AD	14-48	73	male	4.83	14.5	frequent	VI	high	intermediate to high AD	proteomics, IF
Banner	AD	17-60	82	female	4	15	frequent	VI	high	intermediate to high AD	proteomics, IF
Banner	AD	12-49	63	male	5.17	14.5	frequent	VI	high	intermediate to high AD	proteomics, IF
Banner	AD	07-15	80	male	3.16	15	frequent	VI	high	intermediate to high AD	IF
Banner	AD	07-54	82	female	4	15	frequent	VI	high	intermediate to high AD	IF
Banner	AD	09-42	85	male	3	15	frequent	VI	high	intermediate to high AD	IF
Banner	AD	09-46	60	female	5	15	frequent	VI	high	intermediate to high AD	IF
Banner	AD	10-16	68	female	4.16	15	frequent	VI	high	intermediate to high AD	IF
Banner	AD	15-27	84	female	3.33	15	frequent	VI	high	intermediate to high AD	IF
Banner	AD	18-44	87	male	2.16	15	frequent	VI	high	intermediate to high AD	IF
Banner	AD	16-18	91	male	2.97	14.5	frequent	VI	high	intermediate to high AD	IF
Banner	Control	02-33	85	male	2.25	8.25	moderate	III	criteria not met	Not AD	IF
Banner	Control	04-52	85	male	1.83	6.25	sparse	II	criteria not met	Not AD	IF
Banner	Control	05-12	88	female	2	6.25	moderate	III	criteria not met	Not AD	IF
Banner	Control	98-22	90	male	2.5	8	moderate	III	criteria not met	Not AD	IF
Banner	Control	99-58	> 90	female	2.5	1	sparse	III	criteria not met	Not AD	IF
Banner	Control	18-17	87	female	3.08	0	zero	III	criteria not met	Not AD	proteomics
Banner	Control	18-78	71	male	3.5	0	zero	III	Criteria not met	Not AD	proteomics
Banner	Control	18-64	72	male	4.6	0	zero	I	Criteria not met	Not AD	proteomics
Banner	Control	15-60	82	male	3.33	0	zero	II	Criteria not met	Not AD	proteomics
Banner	Control	13-49	75	female	2.5	0	zero	II	criteria not met	Not AD	proteomics
Banner	Control	15-46	82	female	2.07	1	sparse	I	Criteria not met	Not AD	proteomics
Banner	Control	17-50	90	male	3.41	0.5	sparse	I	Criteria not met	Not AD	proteomics

C

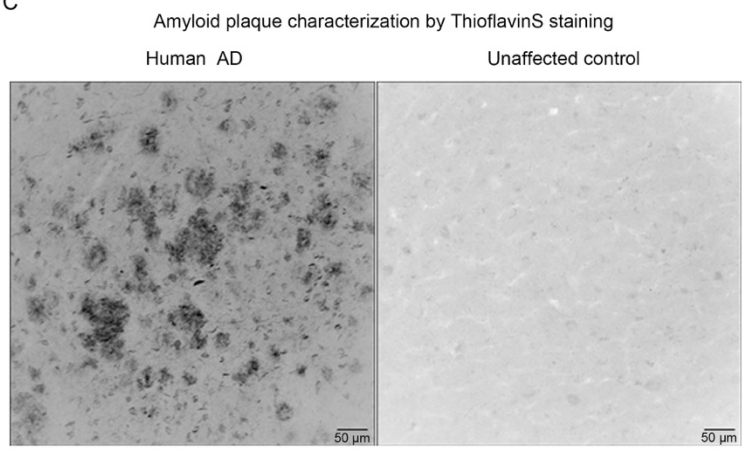

1785 **Figure S1. Metadata associated with the postmortem human brains**
1786 **A-B.** Specimens obtained from: **(A)** the Yale Alzheimer's Research Center and (**B**) the Banner Sun
1787 Health Research Institute. IF = immunofluorescence validation. **C.** Representative images of a
1788 large field of view showing amyloid plaques (dark, ThioflavinS) in postmortem brains of AD
1789 humans and unaffected controls. Scale bar 50 µm.

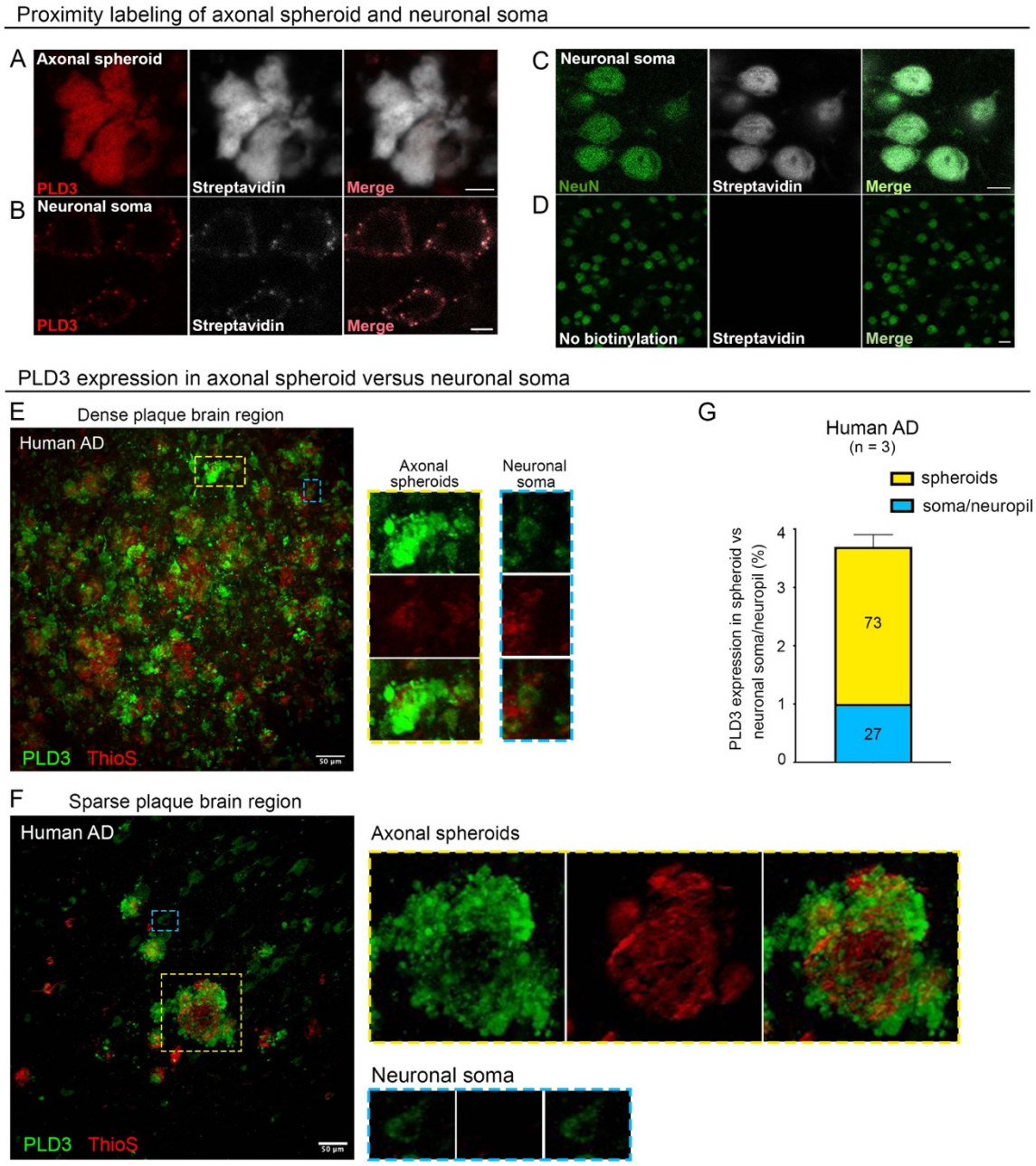

Figure S2. PLD3 expression and proximity labeling of axonal spheroids versus neuronal somata **A-B.** Proximity labeling of PLD3 (red) in (**A**) axonal spheroids versus (**B**) neuronal somata. C. Proximity labeling of NeuN (green, a neuronal soma marker). (**A-C**) Scale bar 5 µm. **D.** No biotinylation reaction control shows that the streptavidin signal was eliminated. Scale bar 50 µm. **E-G.** Comparison of PLD3 expression in axonal spheroids versus neuronal soma. Representative images of PLD3 immunofluorescence staining in AD postmortem brains with (**E**) dense amyloid plaques (red, ThioflavinS stained) and (**F**) sparse amyloid plaques. Inserts show axonal spheroid halos around amyloid plaques (yellow squares) or neuronal soma (blue squares). Scale bar 50 µm. **G.** Quantification of PLD3 expression in axonal spheroids versus neuronal soma/neuropil in AD human postmortem brains (n = 3 brains).

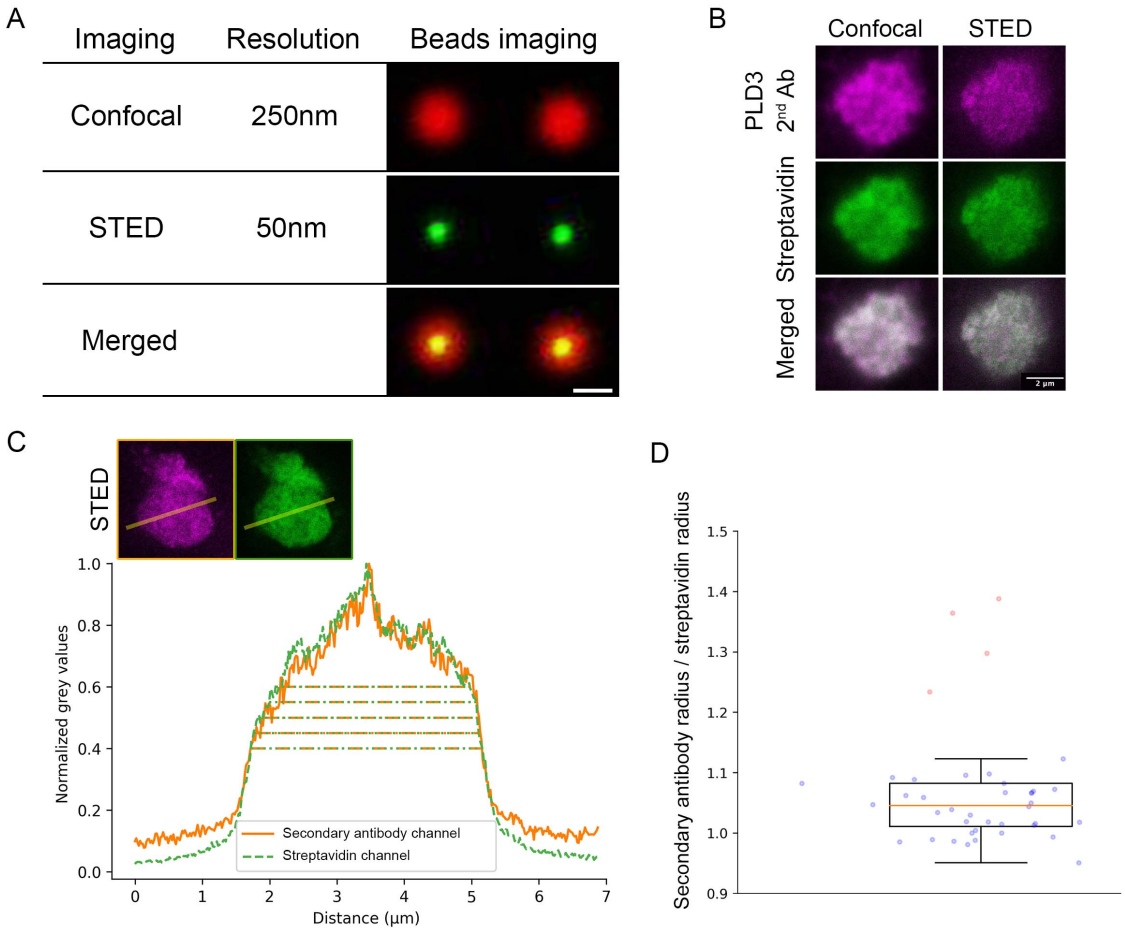

Figure S3. Super-resolution STED imaging reveals high spatial precision of proximity labeling in AD human brain

A. Imaging of beads illustrates the resolution contrast between confocal microscopy (250 nm) and STED microscopy (50 nm). Scale bar = 250 nm. **B-C.** Representative confocal and STED images showing proximity labeling of axonal spheroids (magenta, anti-PLD3 labeled) in AD human postmortem brains. Biotinylated proteins were labeled by streptavidin (green). Scale bar = 2 µm. **C.** A line plot representative of the radius measurements illustrates the signals from both the secondary antibody channel (magenta) and the streptavidin channel (green). **D.** Dot plot depicting the radius ratio between the secondary antibody channel (magenta) and the streptavidin channel (green). Average radius ratio = 141.0 nm, average ratio = 1.04, standard deviation = 0.04. The median value is represented by the orange line, while outliers are denoted by pink circles. Any value surpassing 1.5 times the interquartile range (IQR) above Q3 or below Q1 is classified as an outlier and is subsequently excluded [115].

Optimization of protein extraction from fixed brain tissues

A

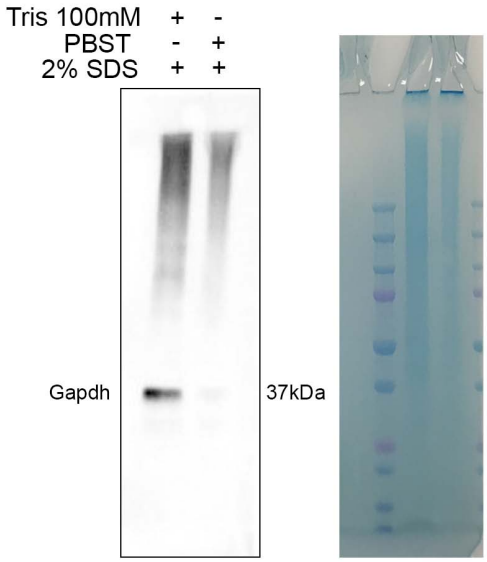

Pull-down of NeuN labeled proteins

B

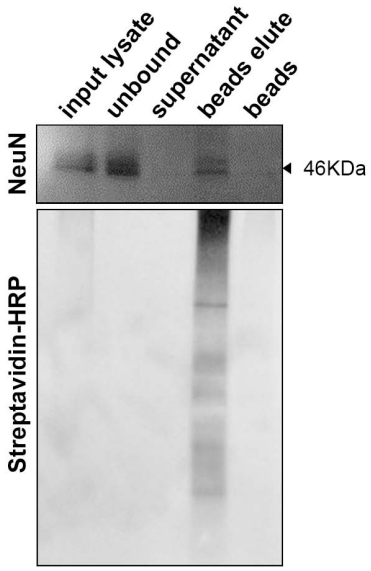

Uncut images of western blots

C

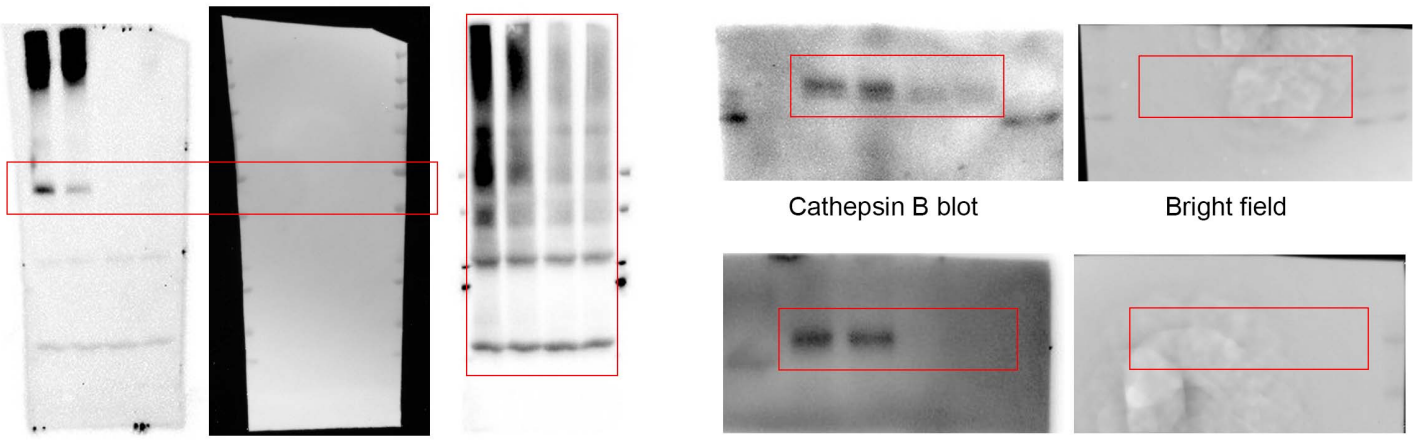

PLD3 blot | Bright field | Streptavidin-HRP blot | Cathepsin B blot | Bright field | RAGC blot | Bright field

D

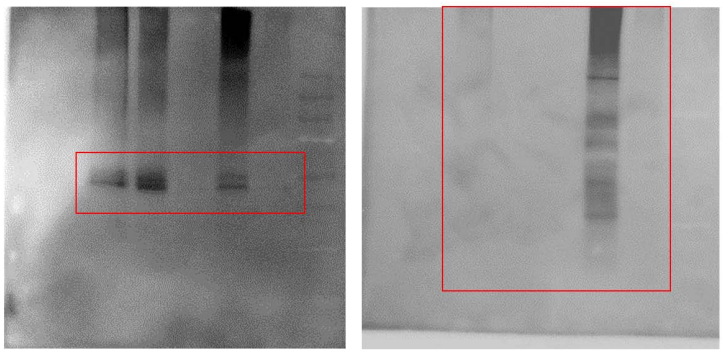

NeuN blot | Streptavidin-HRP blot

1816

1817 **Figure S4. Optimization of protein extraction and western blots**
1818 **A.** Optimization of protein lysis protocol for fixed postmortem brains. The protein lysis buffer
1819 (100 mM Tris-HCL plus 2% SDS) extracted proteins much more efficiently compared to the
1820 previously published method (PBST plus 2% SDS), as indicated by a blot of housekeeping protein
1821 GAPDH and the Coomassie blue gel of the same membrane. **B.** Western blot showing biotinylated
1822 proteins pulled down from an anti-NeuN antibody proximity labeled sample. Biotinylated
1823 proteins, including the protein bait NeuN, were detected in the input brain lysates and
1824 streptavidin bead elutes but not in the supernatant from bead washes nor in the beads
1825 themselves after elution. Although the bait proteins were also detected in the unbound protein
1826 fractions, no streptavidin signal was detected from the unbound proteins, indicating that there
1827 was a portion of endogenous protein baits that was not biotinylated, yet most of the biotinylated
1828 proteins were pulled down efficiently. **C-D.** Uncropped western blot membranes of **(C)** PLD3,
1829 Cathepsin B and RAGC pulled down, related to **Figure 1I**, and **(D)** NeuN pulled down, related to
1830 **Figure S4B**.

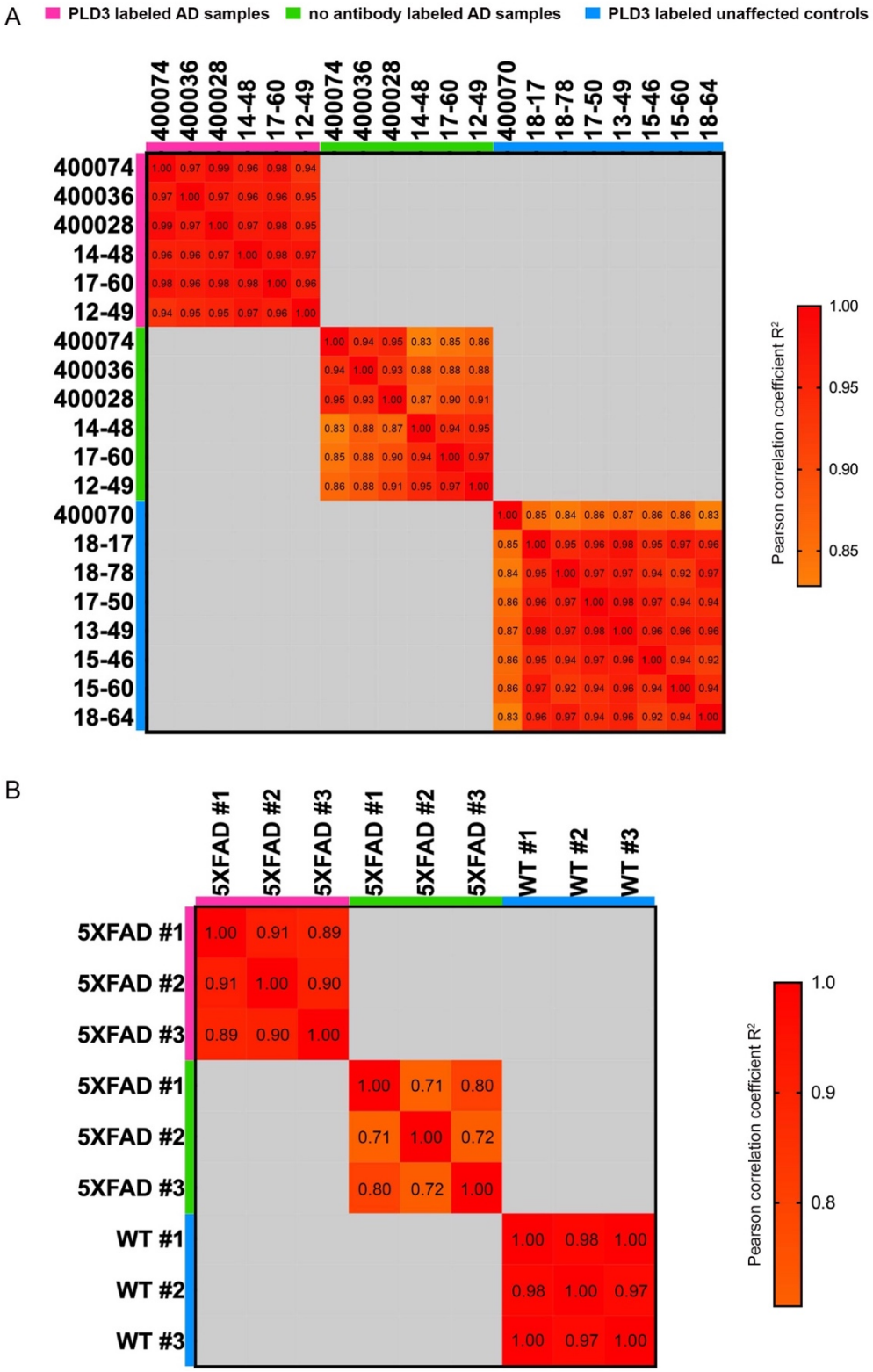

Figure S5. Correlation analysis of proteomics samples in humans and mice

Correlation analysis among biological replicates of PLD3-labeled and no antibody-labeled proteomic samples in (**A**) humans and (**B**) mice. Pearson correlation coefficient R^2 of each comparison is listed in each box.

1835

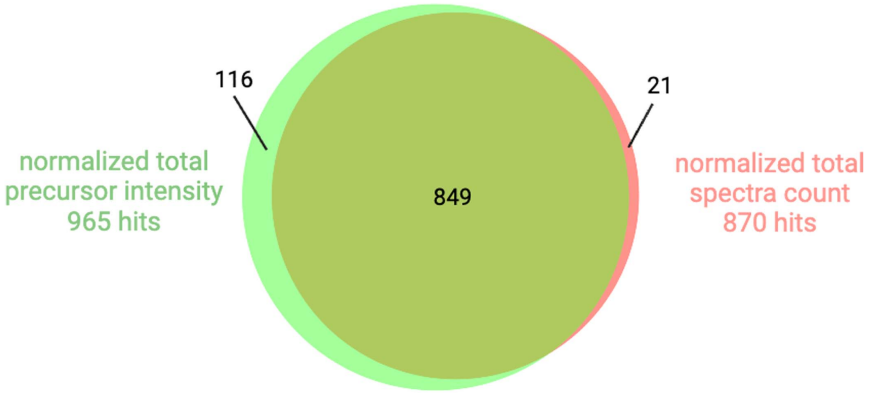

1836 **Figure S6. Quantification approach comparison in human PAAS proteomics.**
1837 Human PAAS proteomics analysis was performed using either normalized total precursor
1838 intensity approach or normalized total spectra count approach. Venn diagram showed the
1839 comparison of 965 proteomics hits and 870 proteomic hits identified by these two approaches
1840 respectively.

A

Breakdown of proteins identified in PLD3-labeled and no antibody-labeled samples in AD humans.

	PLD3 antibody labeled						No antibody labeled					
	AD 1	AD 2	AD 3	AD 4	AD 5	AD 6	AD 1	AD 2	AD 3	AD 4	AD 5	AD 6
Proteins identified (2360 total)	1635	1526	1510	1127	1316	1075	765	809	909	1058	878	943

B

Breakdown of the PAAS proteomic hits identified in each AD human samples.

	AD human#1	AD human#2	AD human#3	AD human#4	AD human#5	AD human#6
Proteins identified (821 total)	793	801	800	722	765	676
Percentage of coverage	96.60%	97.56%	97.44%	87.94%	93.18%	82.34%

1841 **Figure S7. Breakdown of protein numbers identified in each human sample.**
1842 **A.** Table shows all the proteins identified in the PLD3-labeled and no antibody-labeled samples
1843 in each AD humans. **B.** Table shows the identified PAAS proteomic hits number in each AD
1844 humans.

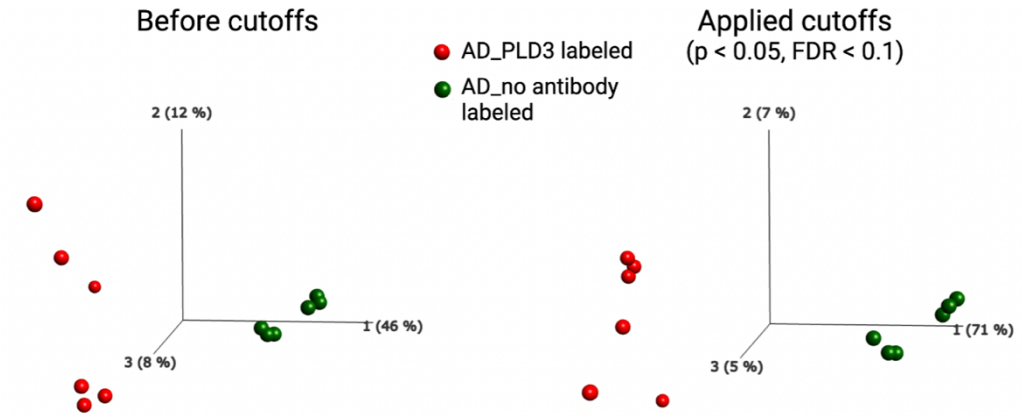

Figure S8. Principal component analysis (PCA) of PLD3-labeled versus no antibody-labeled proteomes in AD human postmortem brains.

PCA plots showing identification of proteins and their quantities were found to be dependent on the presence of the antibody. Even without applying any cutoffs, the PLD3 antibody-labeled samples exhibited clear differentiation from the no antibody-labeled samples. Furthermore, applying cutoffs ($p < 0.05$ and FDR < 0.1) resulted in an increase in PC1 from 46% to 71%.

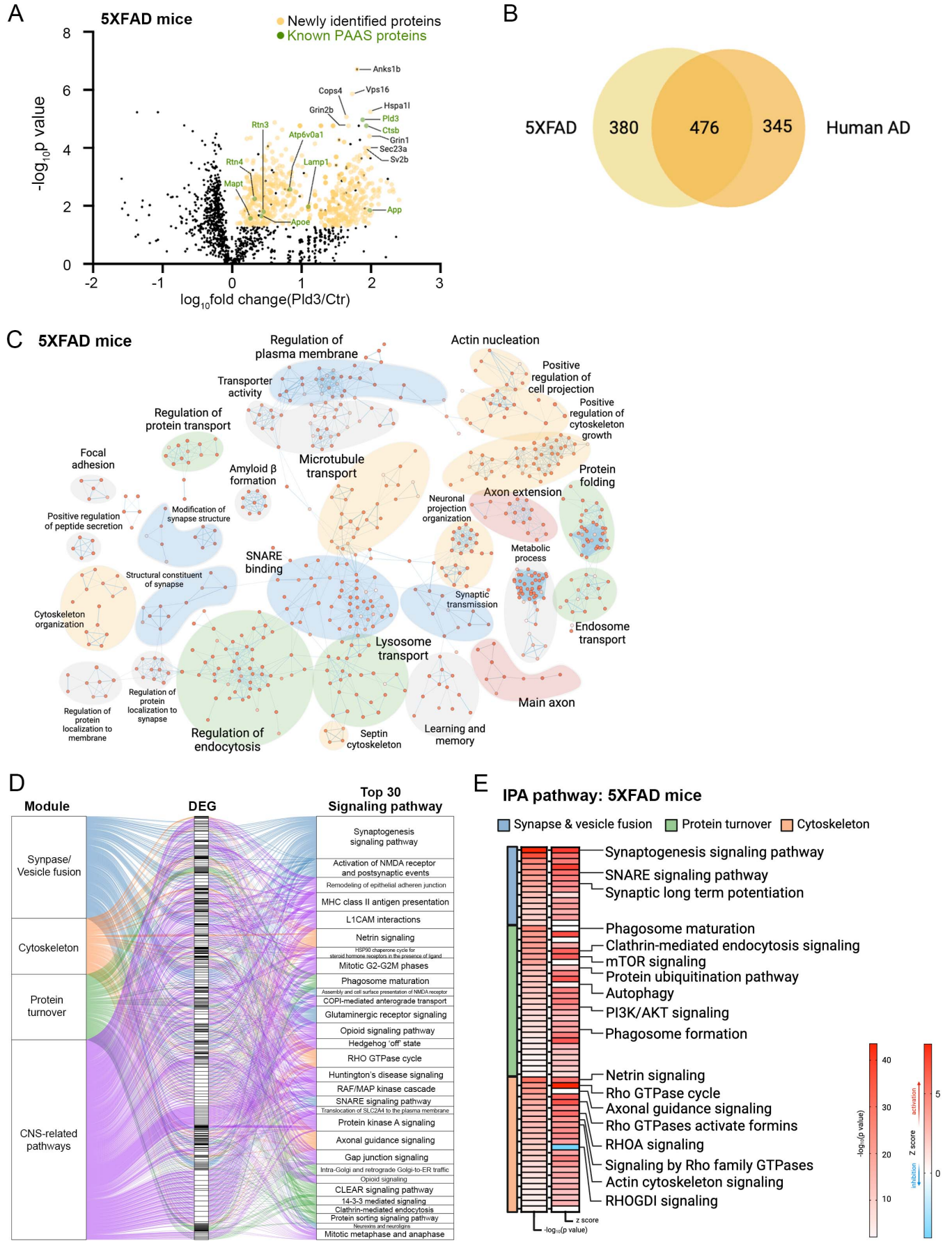
A
5XFAD mice
Newly identified proteins
Known PAAS proteins
-log10p value
log10fold change(Pld3/Ctr)
Anks1b
Cops4
Vps16
Hspa1l
Grin2b
Pld3
Ctsb
Grin1
Sec23a
Sv2b
Rtn3
Atp6v0a1
Rtn4
Lamp1
Mapt
Apoe
App
B
5XFAD
380
476
345
Human AD
C
5XFAD mice
Regulation of plasma membrane
Actin nucleation
Transporter activity
Positive regulation of cell projection
Regulation of protein transport
Positive regulation of cytoskeleton growth
Focal adhesion
Microtubule transport
Amyloid β formation
Protein folding
Axon extension
Neuronal projection organization
Positive regulation of peptide secretion
Modification of synapse structure
Metabolic process
SNARE binding
Structural constituent of synapse
Synaptic transmission
Cytoskeleton organization
Endosome transport
Lysosome transport
Main axon
Regulation of protein localization to synapse
Regulation of protein localization to membrane
Regulation of endocytosis
Septin cytoskeleton
Learning and memory
D
Module
DEG
Top 30 Signaling pathway
Synapse/ Vesicle fusion
Cytoskeleton
Protein turnover
CNS-related pathways
Synaptogenesis signaling pathway
Activation of NMDA receptor and postsynaptic events
Remodeling of epithelial adheren junction
MHC class II antigen presentation
L1CAM interactions
Netrin signaling
HSP90 chaperone cycle for steroid hormone receptors in the presence of ligand
Mitotic G2-G2M phases
Phagosome maturation
Assembly and cell surface presentation of NMDA receptor
COPI-mediated anterograde transport
Glutaminergic receptor signaling
Opioid signaling pathway
Hedgehog 'off' state
RHO GTPase cycle
Huntington's disease signaling
RAF/MAP kinase cascade
SNARE signaling pathway
Translocation of SLC2A4 to the plasma membrane
Protein kinase A signaling
Axonal guidance signaling
Gap junction signaling
Intra-Golgi and retrograde Golgi-to-ER traffic
Opioid signaling
CLEAR signaling pathway
14-3-3 mediated signaling
Clathrin-mediated endocytosis
Protein sorting signaling pathway
Neurexins and neuroligins
Mitotic metaphase and anaphase
E
IPA pathway: 5XFAD mice
Synapse & vesicle fusion
Protein turnover
Cytoskeleton
Synaptogenesis signaling pathway
SNARE signaling pathway
Synaptic long term potentiation
Phagosome maturation
Clathrin-mediated endocytosis signaling
mTOR signaling
Protein ubiquitination pathway
Autophagy
PI3K/AKT signaling
Phagosome formation
Netrin signaling
Rho GTPase cycle
Axonal guidance signaling
Rho GTPases activate formins
RHOA signaling
Signaling by Rho family GTPases
Actin cytoskeleton signaling
RHOGDI signaling
z score
-log10(p value)
-log10(p value)
Z score
activation
inhibition

1852 **Figure S9. Proteomics analysis of PLD3-labeled PAAS proteomes in 5XFAD mice**
1853 **A.** Volcano plot show proteins (represented by their gene names) that passed the statistical
1854 cutoffs (yellow dots) in 5XFAD mice. The top 10 proteomic hits with the lowest p-value and
1855 highest fold changes are indicated by their gene names in black. The selected known PAAS
1856 proteins are labeled as green dots and their gene names in green. The black dots among the
1857 yellow ones represent proteins being filtered by the statistical cutoff as shown in Figure 2B. (See
1858 **Table S1** for full list of proteomic hits). **B.** Venn diagram shows shared proteomics hits between
1859 AD humans and mice. **C.** Pathway enrichment analysis of PAAS proteome in 5XFAD mice. The
1860 Enrichment Map represents a network of pathways where edges connect pathways with many
1861 shared genes. Node color reflects the FDR of each pathway. The theme labels were curated based
1862 on the main pathways of each subnetwork. Subnetworks with a minimum of four pathways
1863 connected by edges are shown. **D**. IPA pathway analysis of the PAAS proteome in 5XFAD mice.
1864 Top 30 CNS-related signaling pathways are shown. The signaling pathways are summarized as 4
1865 modules. The alluvium plot shows different modules connect to the differentially expressed
1866 genes (DEGs) and the DEGs connects to the pathways that they are involved. **E.** IPA pathways
1867 related to the three modules with a p-value less than 0.01 are listed. Heatmaps indicate either
1868 the $-\log_{10}$ (p-value) or the z score of each signaling pathway (pathways with a z score in red are
1869 predicted to be activated while blue ones are predicted to be inhibited).

List of known and newly validated proteins in PAAS of humans and mice

Protein	known/ newly validated PAAS proteins	identified in the PAAS proteomes	reference
PLD3	known	yes	Nackenoff et al, Plos Genet. 2021, Yuan et al, Nature, 2022
Cathepsin B (CTSB)	known	yes	Gowrishankar et al, PNAS, 2015;
Cathespin D (CTSD)	known	yes	Gowrishankar et al, PNAS, 2015;
Lamp1	known	yes	Gowrishankar et al, PNAS, 2015;
neurofilament (NEFL, NEFM, NEFH)	known	yes	Gowrishankar et al, PNAS, 2015;
RagC (RRAGC)	known	yes	Gowrishankar et al, PNAS, 2015;
ATG9A	known	yes	Sharoar et al, Mol Psychiatry, 2019
Ubiquitin	known	yes	Sharoar et al, Mol Psychiatry, 2019; Torres et al, Mol. Neurodegener. 2012
Rtn1	known	yes	Shi et al, Sci Report, 2017
Rtn3	known	yes	Sharoar et al, Mol Psychiatry, 2019
PKC (alpha, beta, gamma) (PRKCA, PRKCB, PRKCG)	known	yes	Masliah et al, J. Neurosci, 1991
Synaptophysin	known	yes	Adalbert et al, Brain, 2009
SNAP25	known	yes	Ferer et al, J. NeuropathoL Exp. Neurol. 1998
VAMP2	known	yes	Gowrishankar et al, PNAS, 2015;
beta tubulin III	known	yes	Sadleir et al, Acta Neuropathol, 2016
APP	known	yes	Yuan et al, Neuron, 2016
Atp6v0a1	known	yes	Yuan et al, Nature, 2022
Tau (MAPT)	known	yes	He et al, Nat Med, 2018; Bassil et al, Nat Commun. 2021
Phospho-Tau Ser202, Thr205, AT8	known	N/A	He et al, Nat Med, 2018; Bassil et al, Nat Commun. 2021
Phospho-Tau S235	known	N/A	Bassil et al, Nat Commun. 2021
Phospho-Tau S396	known	N/A	Bassil et al, Nat Commun. 2021
Phospho-Tau S404	known	N/A	Bassil et al, Nat Commun. 2021
Saposin	known	no (did not pass statistical cutoff)	Sharoar et al, Mol Neurodegener, 2021
BACE (D10E5)	known	no	Sadleir et al, Acta Neuropathol, 2016
LC3b	known	no	Sharoar et al, Mol Psychiatry, 2019; Torres et al, Mol. Neurodegener. 2012
M6PR	known	no	Gowrishankar et al, PNAS, 2015;
PGRN	known	no	Gowrishankar et al, PNAS, 2015;
Synaptotagmin-11 (SYT11)	newly validated	yes	this study
SPTBN1	newly validated	yes	this study
APOE	newly validated	yes	this study
HDLBP	newly validated	yes	this study
C3	newly validated	yes	this study
HEXB	newly validated	yes	this study
TMEM30A	newly validated	yes	this study
mTOR	newly validated	yes	this study
p-mTOR S2448	newly validated	N/A	this study
LAMTOR1	newly validated	yes	this study
AKT1	newly validated	yes	this study
RagA (RRAGA)	newly validated	yes	this study
PIK3R4	newly validated	no (did not pass statistical cutoff)	this study
RHEB	newly validated	no (did not pass statistical cutoff)	this study
RAPTOR	newly validated	no (did not pass statistical cutoff)	this study
ITM2B	newly validated	yes	this study
ATP2B3	newly validated	yes	this study
Synaptotagmin-1 (SYT1)	newly validated	yes	this study
Calmodulin (CALM1)	newly validated	yes	this study
CAMK2A	newly validated	yes	this study
NTRK2	newly validated	yes	this study
GAPDH	newly validated	yes	this study
G3BP2	newly validated	yes	this study
PKAα/β cat (PRKACA, PRKACB)	newly validated	yes	this study
GAA	newly validated	yes	this study
SV2A	newly validated	yes	this study

Figure S10. List of known PAAS proteins and newly validated PAAS proteomic hits in human and mice

Full information of this table including the antibodies, immunofluorescence staining information and quantification can be found in **Table S2**.

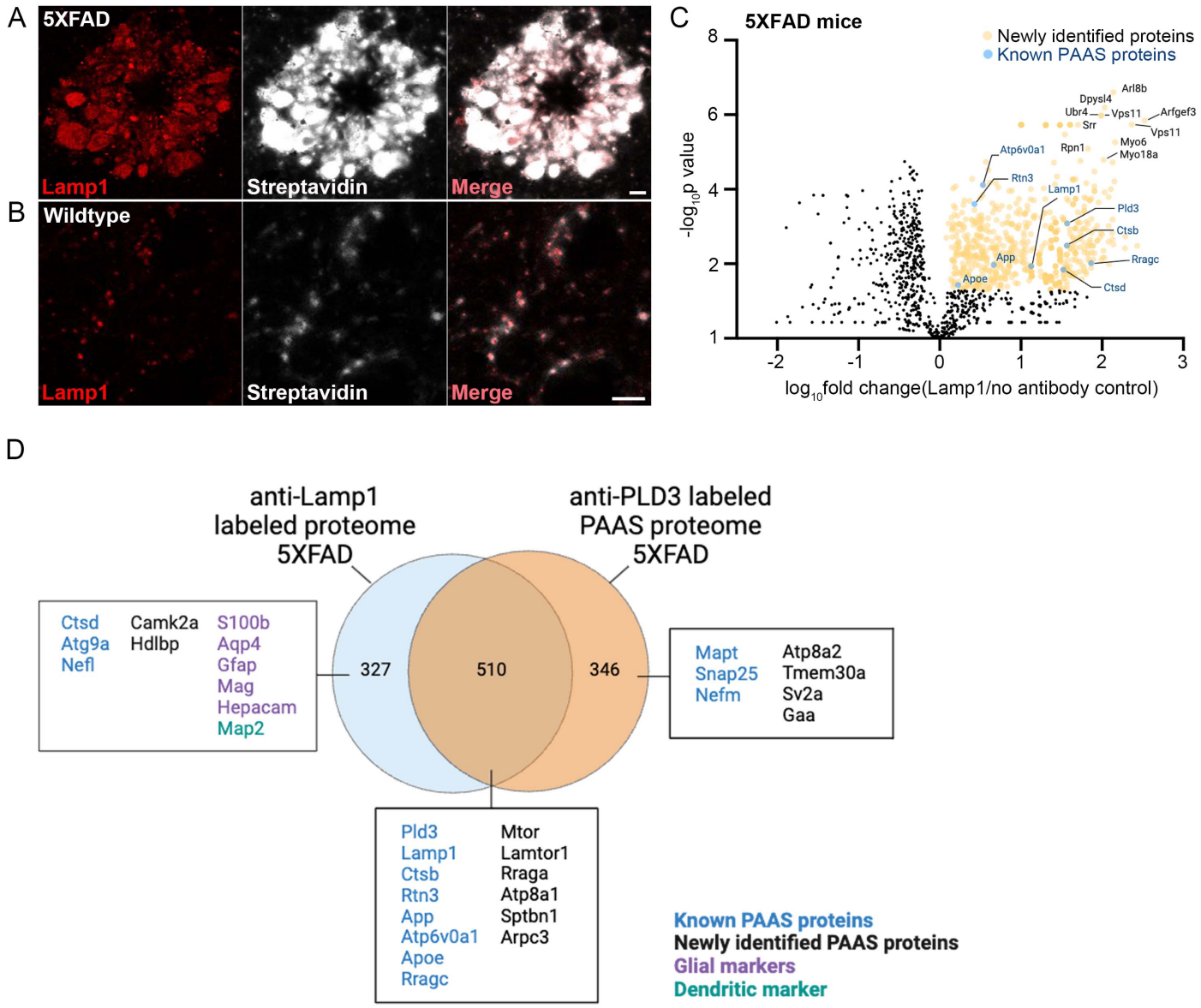

Figure S11. Comparison between anti-Lamp1 antibody labeled proteome with the anti-PLD3 antibody labeled PAAS proteomes in 5XFAD mice.

A-B. Proximity labeling of Lamp1 (red) in (**A**) 5XFAD and (**B**) wild type mice. Lamp1 (red) labeled (**A**) axonal spheroid halo in 5XFAD mice and (**B**) lysosomes in neuronal cell bodies. Biotinylated proteins were labeled by streptavidin. Scale bar 5 µm. **C.** Volcano plot shows proteins that passed the statistical cutoffs (yellow dots) in 5XFAD mice. The gene names of the top 10 proteomic hits with the lowest p-value and highest fold changes are shown in black. The known PAAS proteins are shown as dark blue dots with their gene names labeled in blue. (See **Table S1** for full list of proteomic hits). **D.** Venn diagram showing comparison of the anti-Lamp1 antibody labeled proteomes with the anti-PLD3 antibody labeled PAAS proteomes in 5XFAD mice. Selected known PAAS proteins are shown in blue, newly identified proteins are shown in black, glial marker proteins are shown in purple and dendritic marker protein is shown in green.

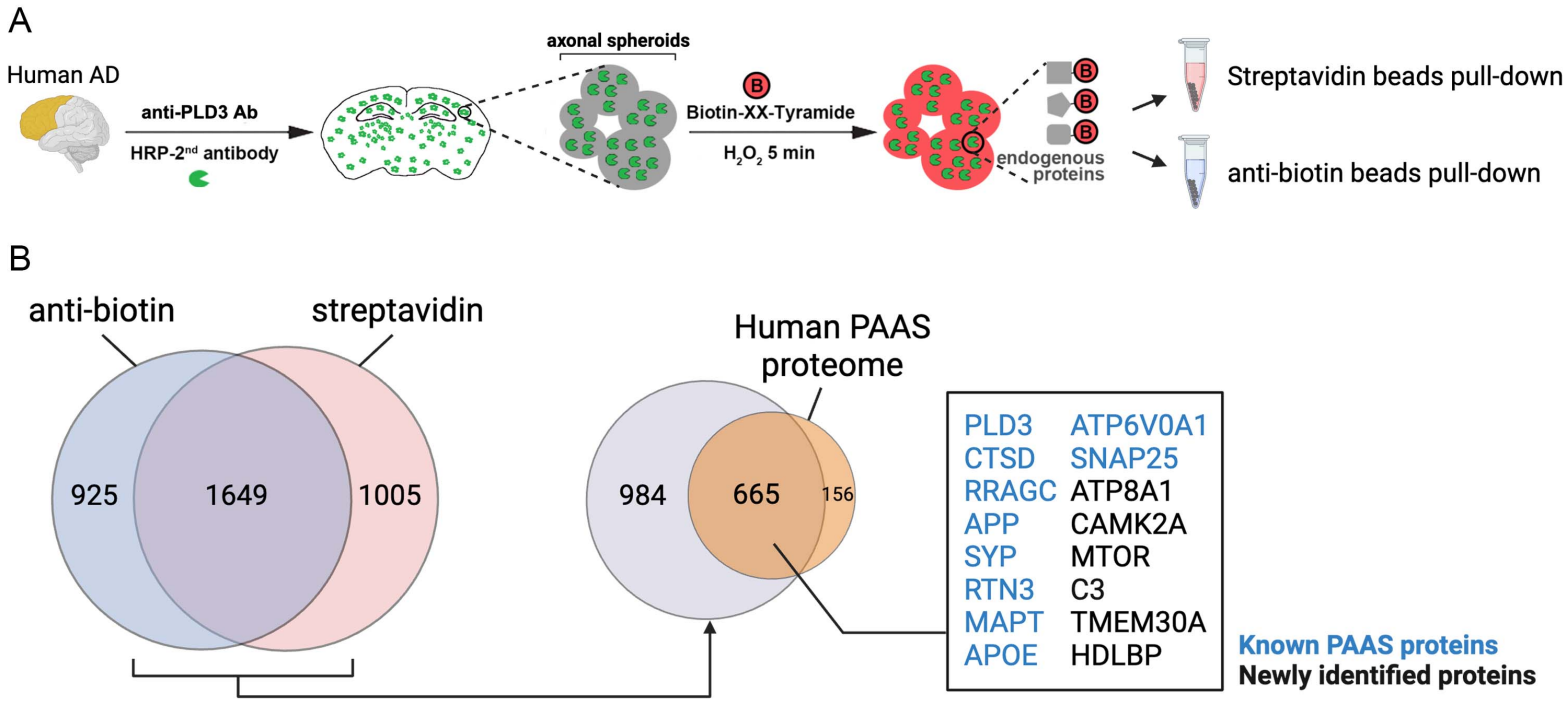

Figure S12. Comparison between anti-biotin beads pulldown with streptavidin beads pulldown of anti-PLD3 antibody labeled proteomes in AD human brains.

A. Schematic showing pipelines for using streptavidin beads or anti-biotin beads to pulldown anti-PLD3 antibody labeled proteomes in AD human brains. For streptavidin beads, tissue sections were lysed and then incubated with streptavidin beads. For anti-biotin beads, protein lysate was digested prior to anti-biotin beads pull down. **B.** Comparison of the proteomes captured using anti-biotin beads and those captured with streptavidin beads. Among the total 821proteomic hits identified in the human PAAS proteome, 665 hits were pulldown by both the streptavidin beads method and the anti-biotin beads method. Selected known PAAS proteins (blue) and newly identified proteins (black) are shown in the box.

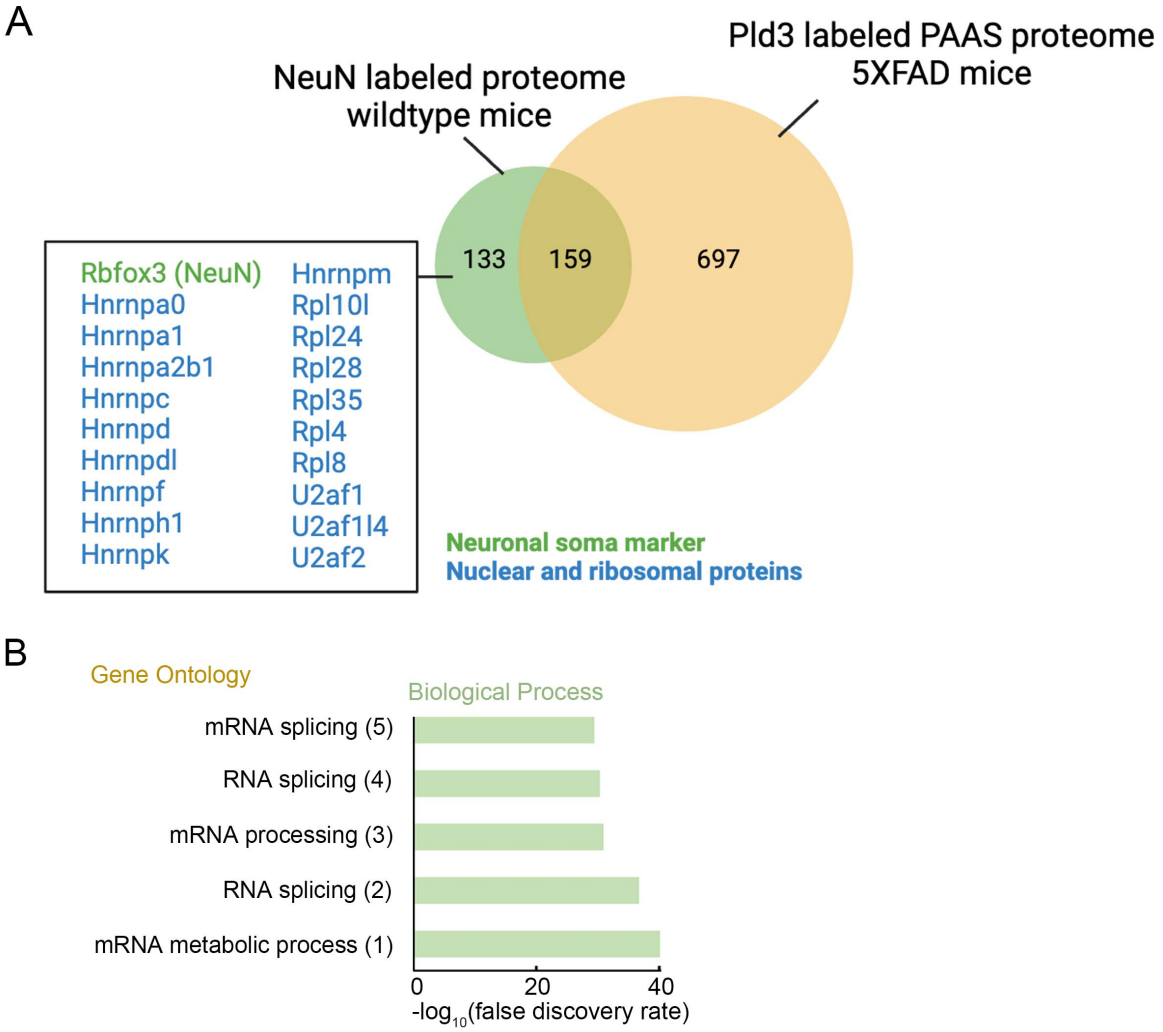

Figure S13. Proteomics analysis of NeuN-labeled neuronal nuclei and perinuclear cytoplasm proteomes in mice

A. The NeuN-labeled neuronal nuclei and perinuclear cytoplasm proteomes in wildtype C57BL/6J mice contain 292 proteomic hits. Comparison between the NeuN-labeled proteome and the PLD3-labeled PAAS proteome in mice showed 159 proteins are shared. Among the 133 unique protein hits in the anti-NeuN-labeled proteome, the protein bait and neuronal soma marker NeuN was detected, along with many nuclear and ribosomal proteins. **B** Gene Ontology analysis shows the top ranked biological process terms of the anti-NeuN-labeled proteomic dataset.

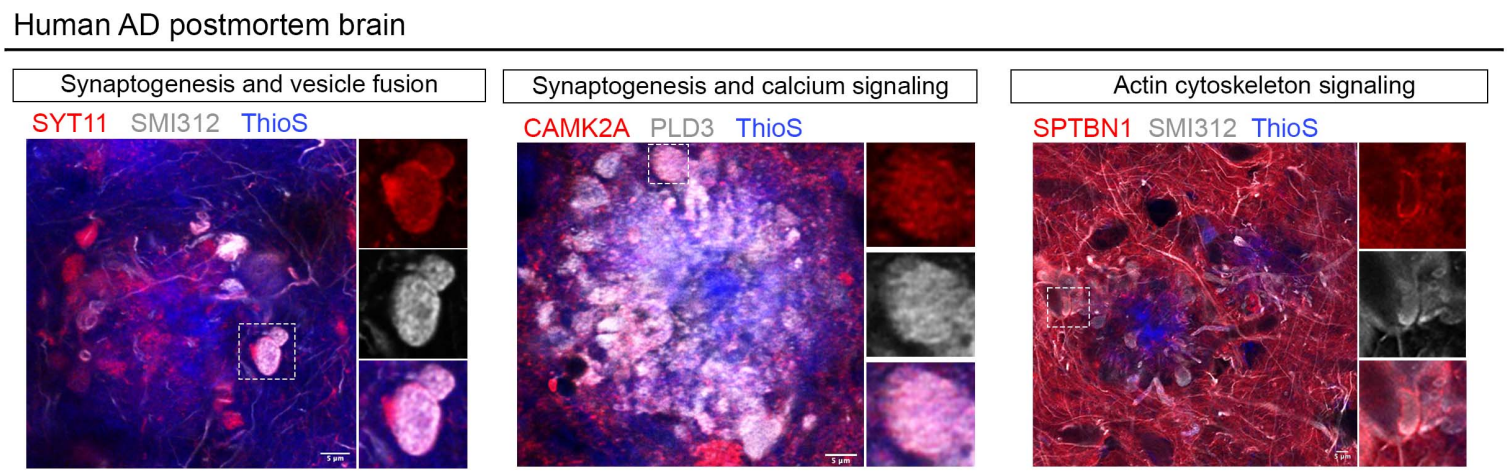

Figure S14. Immunofluorescence confocal imaging validation of new proteins related to synaptogenesis, vesicle fusion, calcium signaling and actin cytoskeleton in axonal spheroid in AD human postmortem brains.

Representative zoom-out immunofluorescence confocal images of newly identified proteins expressed in axonal spheroids in AD human postmortem brains (inserts were shown in **Figure 3E**). Scale bar = 5 µm. Quantification was performed in n = 10 AD human brains. Protein expression quantifications can be found in **Table S2**.

Human AD postmortem brain

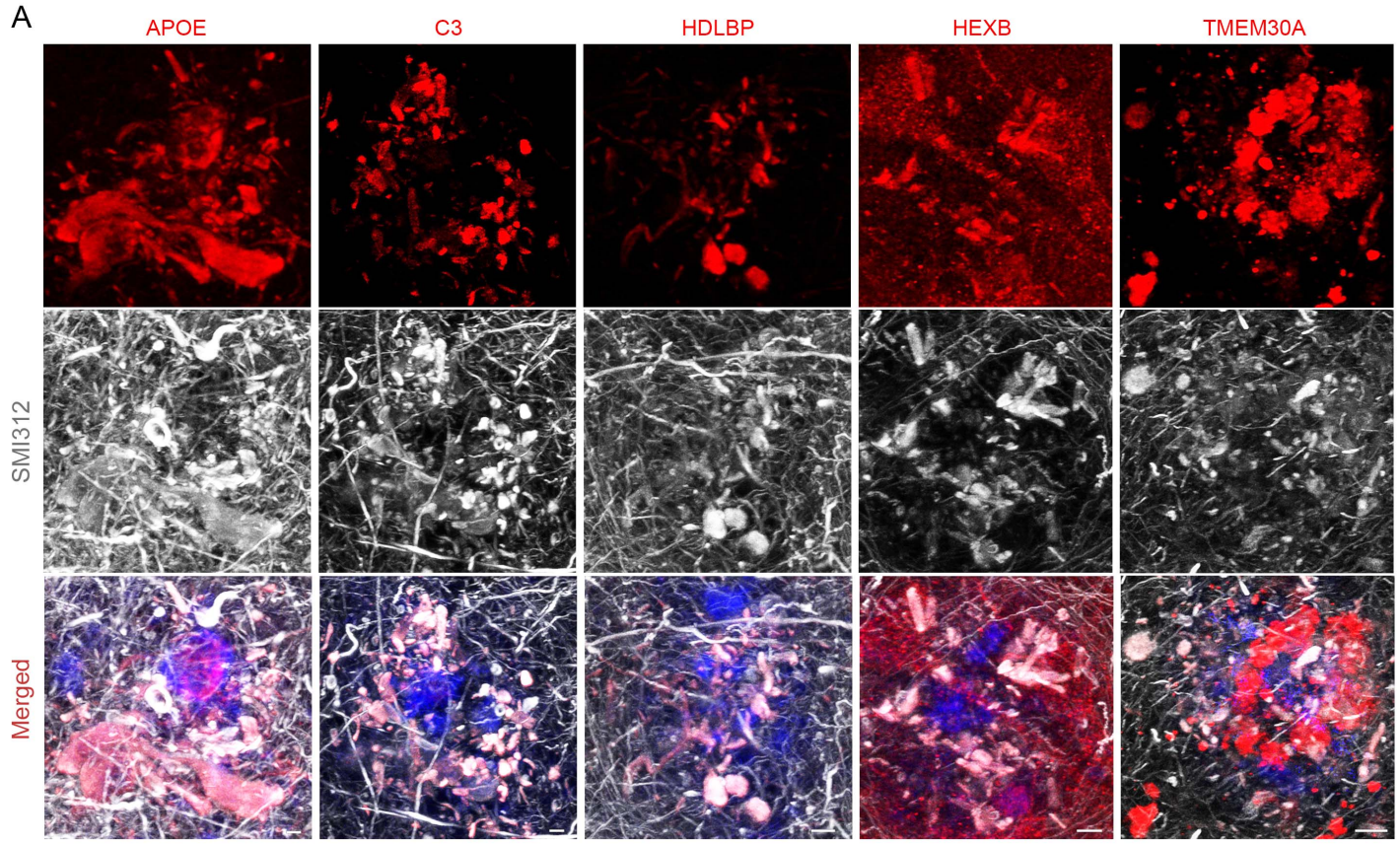

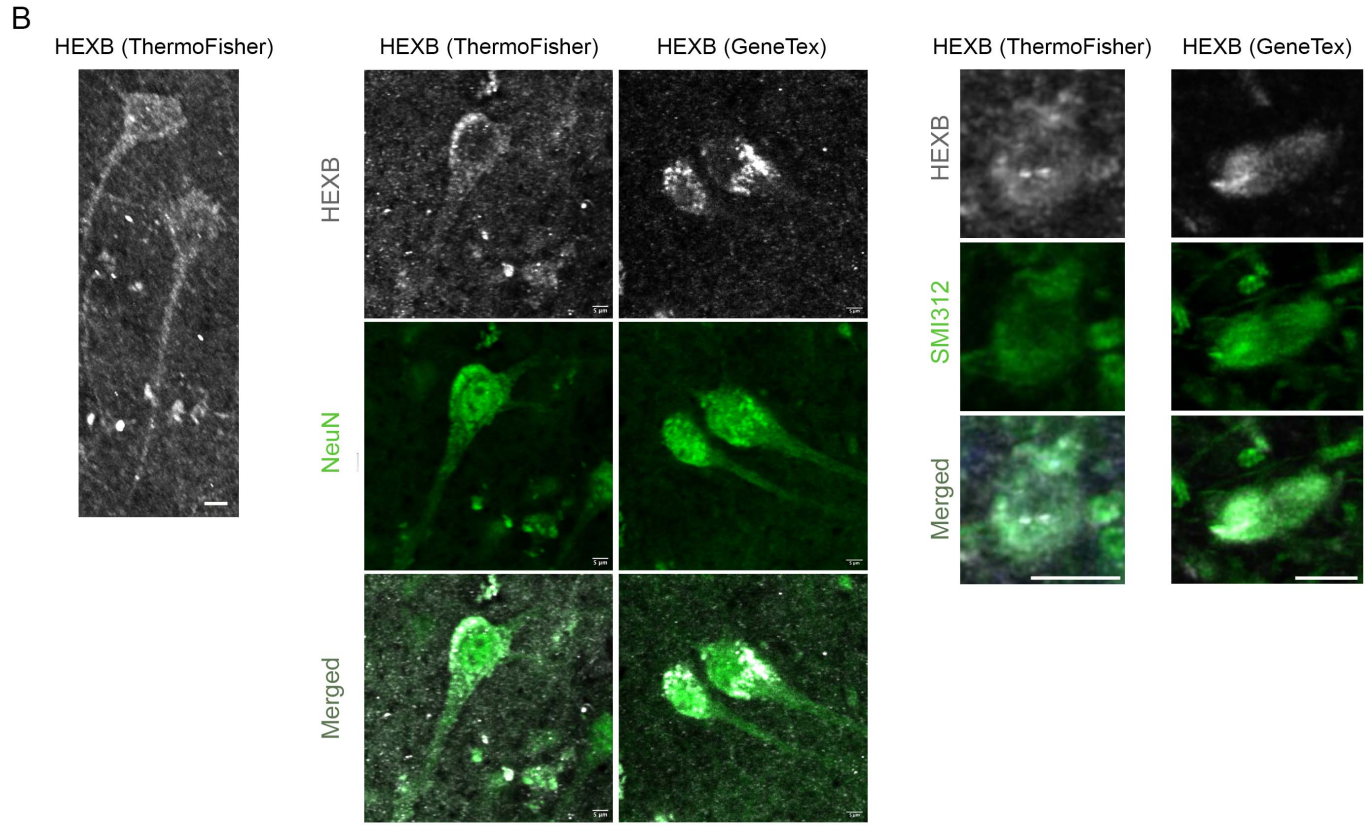

1918 **Figure S15. Lipid transport-related proteins are expressed in axonal spheroids around amyloid**
1919 **plaques in AD human postmortem brains**

1920 **A.** Representative immunofluorescence confocal images of the top-ranked lipid-related
1921 proteomic hits, including APOE, HDLBP, C3, HEXB and TMEM30A in AD humans. Lipid transport-
1922 related molecules are shown in red. Neurofilament marker SMI312 (grey) indicates the neuronal
1923 branches, and axonal spheroid structures around amyloid plaques (ThioflavinS, blue). Scale bar =
1924 5 µm. Quantification was performed in n = 3 AD human brains. Protein expression quantifications
1925 can be found in **Table S2**. **B.** Immunofluorescence confocal image shows HEXB (grey) expressed
1926 in neuronal cell bodies (NeuN, green) and axonal spheroids (SMI312, green) in AD human
1927 postmortem brain (n = 3). Two different HEXB antibodies were used for validation. Scale bar = 5
1928 µm.

1929

1930

Amyloid treatment in hiPSC-derived neuron-glia co-culture

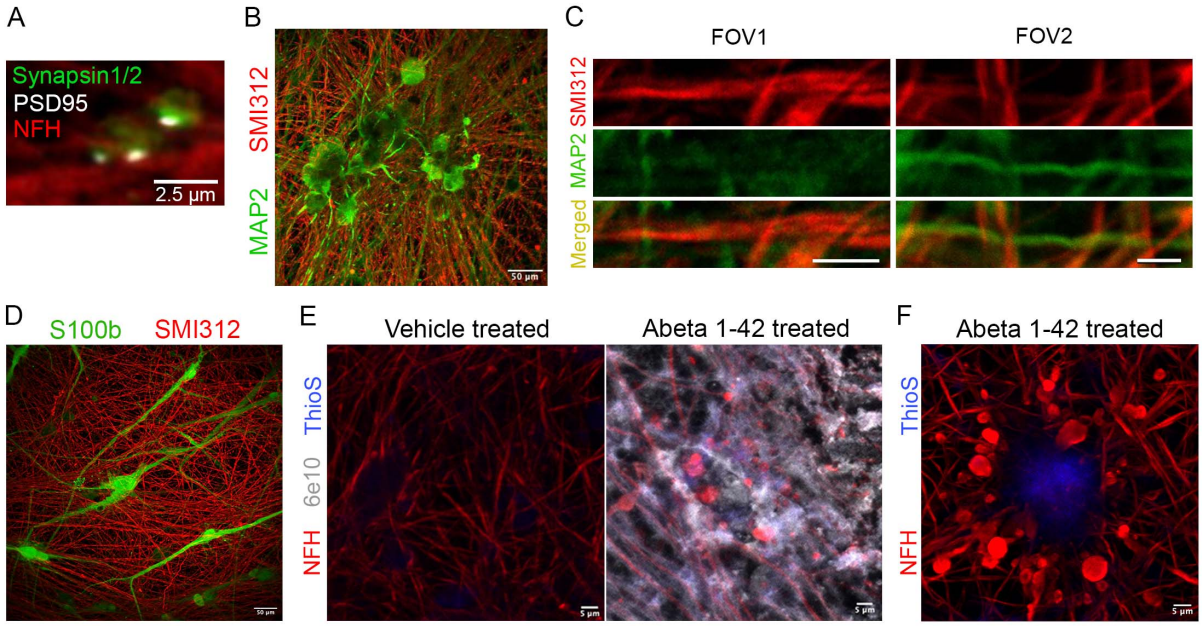

Phosphorylated Tau expression in human neuron derived axonal spheroids

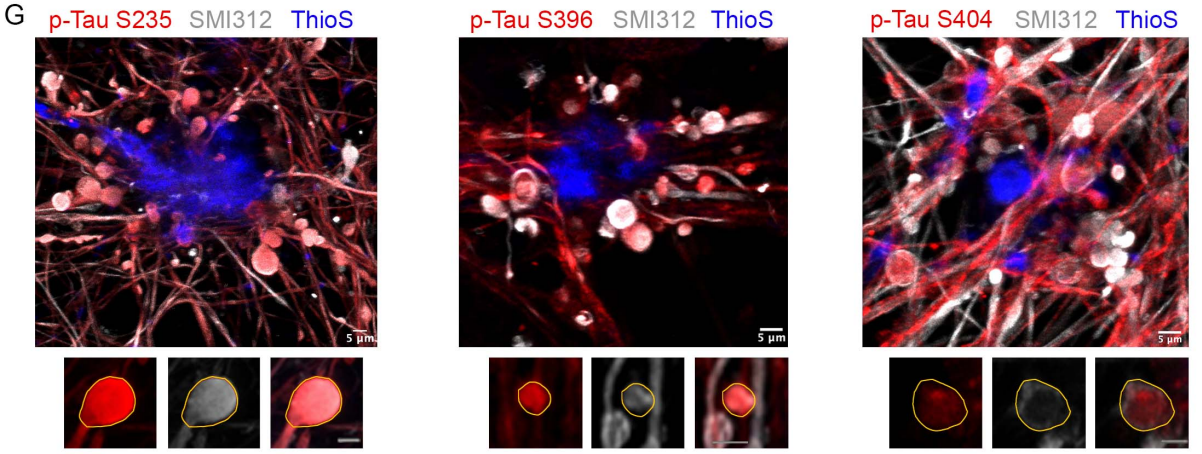

AAV transduction in human neurons

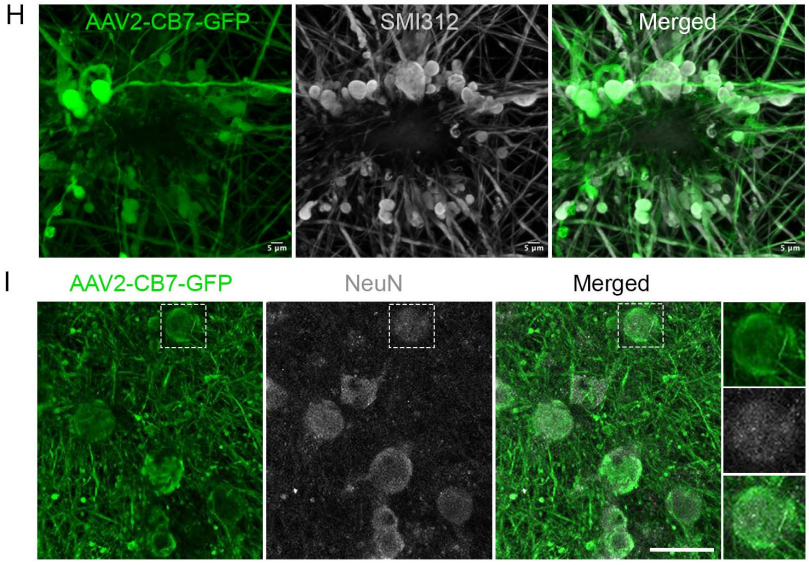

1931 **Figure S16. Characterization of the human iPSC-derived neuron-astrocyte coculture AD model**
1932 **A.** Immunofluorescence confocal deconvolved image shows iPSC-derived human neurons (red,
1933 neurofilament H) robustly expressing pre- and post-synaptic markers (green, Synapsin1/2; grey,
1934 PSD95) at day 150 of coculture. Scale bar 2.5 µm. **B-C.** Immunofluorescence confocal image
1935 shows neuronal cell bodies and dendritic processes (green, MAP2), as well as axonal processes
1936 (red, SMI312) of iPSC-derived human neurons. (**B**) A low-zoom field of view (FOV). Scale bar 50
1937 µm. (**C**) Two high-zoom FOVs showing dendritic and axonal processes. Scale bar 5 µm. **D.**
1938 Immunofluorescence confocal image shows the presence of both neurons (grey, SMI312) and
1939 astrocytes (red, S100b) in the coculture. Scale bar 50 µm. **E.** Immunofluorescence confocal
1940 images show 6e10 positive (grey) and ThioflavinS positive (blue) amyloid beta deposits formed
1941 in human iPSC-derived AD model following treatment with amyloid beta 1-42 peptides. Axonal
1942 processes were labeled with neurofilament (NFH, red). Scale bar 5 µm. **F.** Immunofluorescence
1943 confocal image shows axonal processes formed spheroids (NFH, red) around amyloid plaque
1944 deposit (ThioflavinS, blue). Scale bar 5 µm. **G.** Immunofluorescence confocal deconvolved images
1945 show phosphorylated Tau S235, S396 and S404 (red) expression in PAAS derived from human
1946 neurons (grey, SMI312). Zoom out images were maximum projected, while the zoom in images
1947 show a single plane. Scale bar 5 µm. **H-I.** Immunofluorescence confocal deconvolved images of
1948 AAV2-CB7-GFP infected (**H**) human neurons with abundant axonal spheroids (green, anti-GFP
1949 staining), co-stained with the axonal spheroid marker SMI312 (grey); **(I**) cell bodies of human
1950 neurons, as revealed by both anti-GFP (green) and anti-NeuN (grey) staining, related to **Figure**
1951 **6O**. Scale bar (**H**) 5 µm and (**I**) 50 µm.

1952

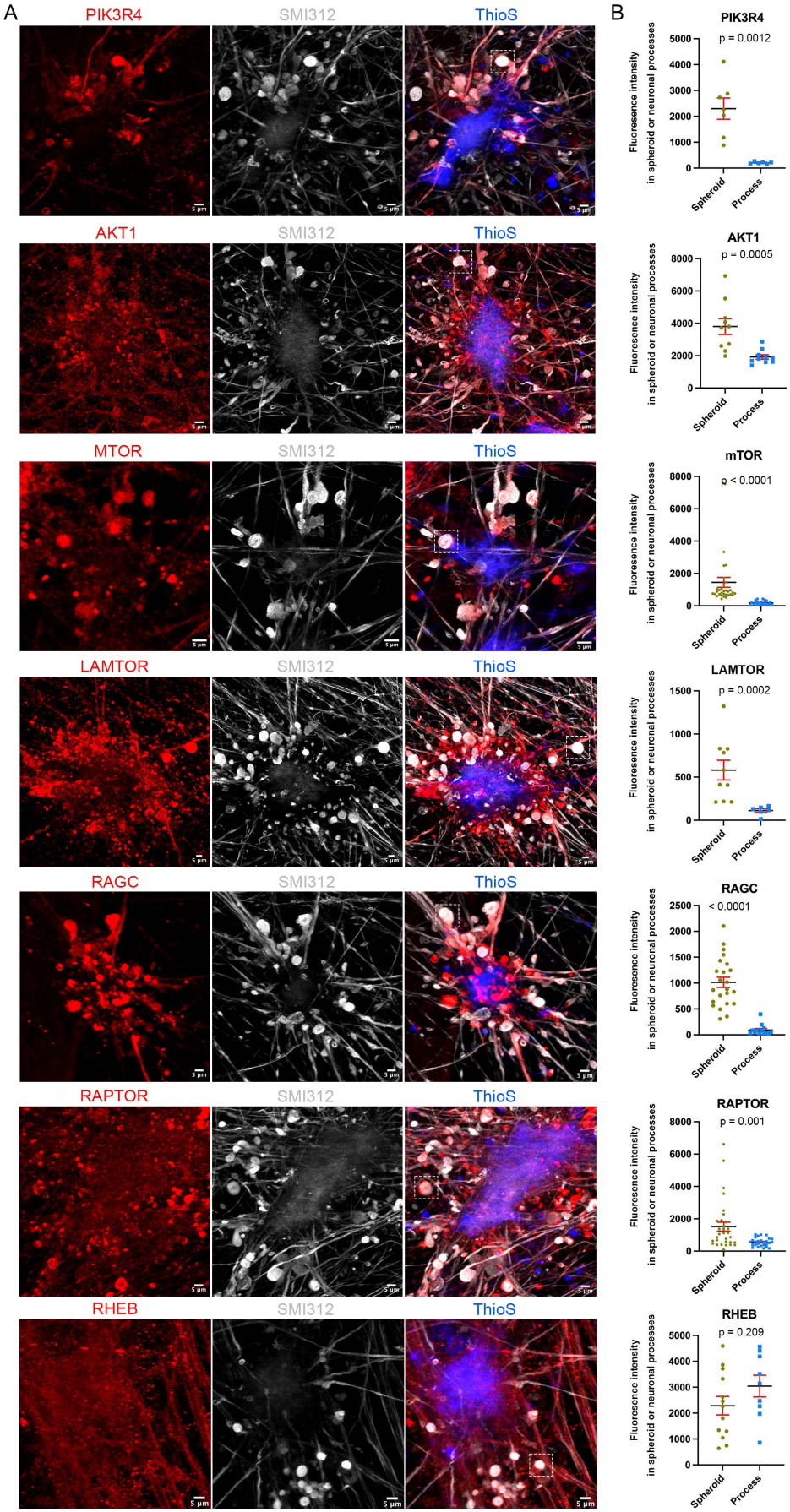
A
PIK3R4
SMI312
ThioS
AKT1
MTOR
LAMTOR
RAGC
RAPTOR
RHEB
B
PIK3R4
p = 0.0012
AKT1
p = 0.0005
mTOR
p < 0.0001
LAMTOR
p = 0.0002
RAGC
< 0.0001
RAPTOR
p = 0.001
RHEB
p = 0.209
Fluoresence intensity in spheroid or neuronal processes
Spheroid
Process

1953 **Figure S17. Immunofluorescence confocal imaging of the PI3K/AKT/mTOR signaling in human**
1954 **iPSC-derived neuron-astrocyte coculture AD model**
1955 **A.** PI3K/AKT/mTOR signaling molecules (red) are expressed in hiPSC-derived axonal spheroids
1956 (grey, SMI312) around amyloid plaque (blue, ThioflavinS). Spheroids in the white boxes in each
1957 large field-of-view image are shown as cropped images in **Figure 6I**. Scale bar 5 µm. **B.**
1958 Quantification of fluorescence intensity of protein hits in axonal spheroids versus neuronal
1959 processes. Each dot represents an ROI from three independent experiments. Unpaired non-
1960 parametric t test (Mann-Whitney) was performed. Error bars indicate SEM.

1961

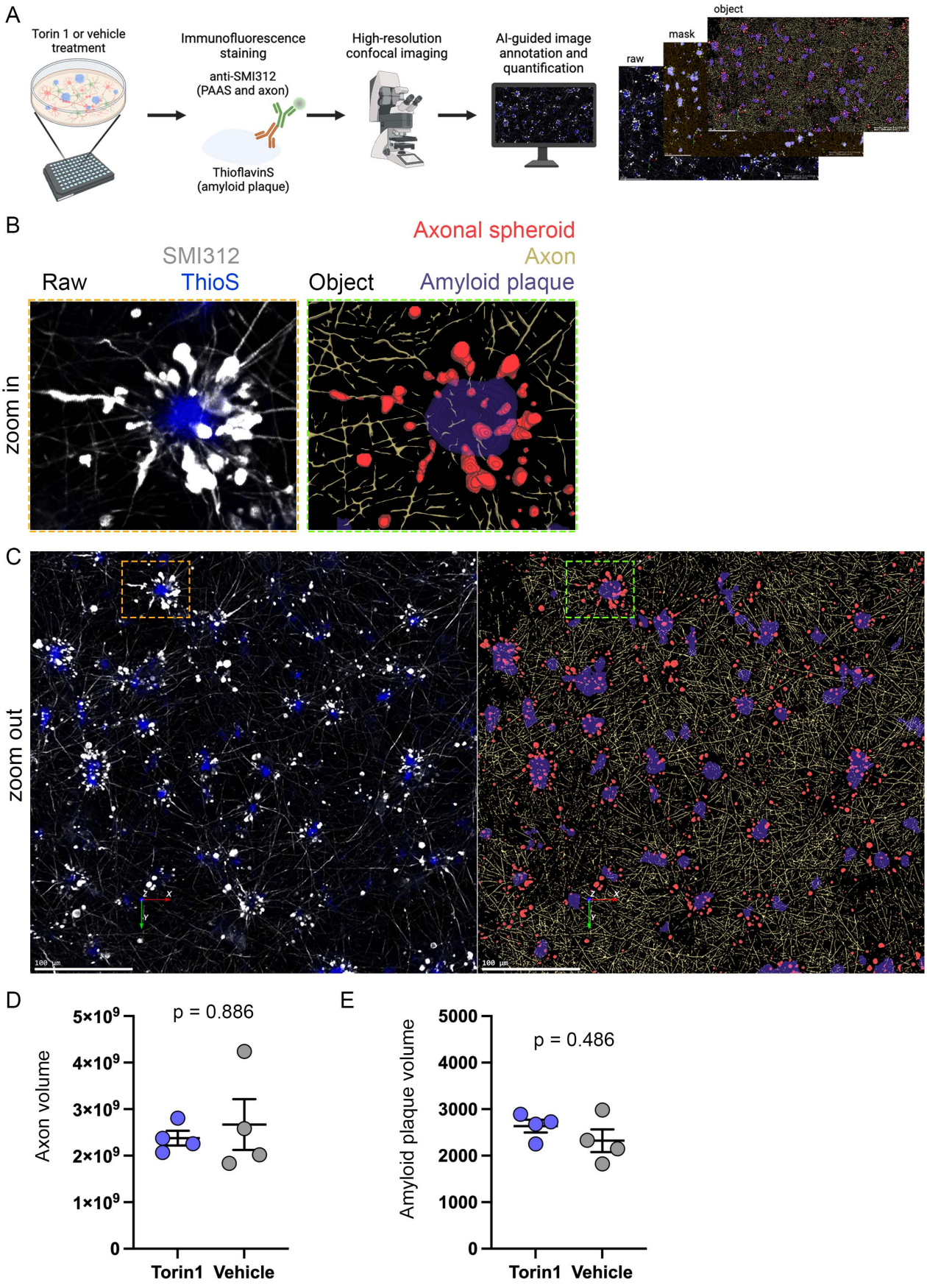
A
Torin 1 or vehicle treatment
Immunofluorescence staining
anti-SMI312 (PAAS and axon)
ThioflavinS (amyloid plaque)
High-resolution confocal imaging
AI-guided image annotation and quantification
raw
mask
object
B
Raw
SMI312
ThioS
Object
Axonal spheroid
Axon
Amyloid plaque
zoom in
C
zoom out
100 µm
D
Axon volume
p = 0.886
5×10⁹
4×10⁹
3×10⁹
2×10⁹
1×10⁹
0
Torin1
Vehicle
E
Amyloid plaque volume
p = 0.486
5000
4000
3000
2000
1000
0
Torin1
Vehicle

1962 **Figure S18. High throughput automated quantification of axonal spheroids, axons and amyloid**
1963 **plaques in human iPSC-derived AD model**

1964 **A.** Schematic showing the workflow of immunofluorescence labeling of axonal spheroids, axons
1965 and amyloid plaques in human iPSC-derived AD model, followed by confocal imaging and
1966 machine learning-based image analysis and quantification. **B-C.** Zoom in (**B**) and zoom out (**C**)
1967 images of immunofluorescence confocal imaging showing SMI312 antibody labeled axonal
1968 spheroids and axons (white), ThioflavinS labeled amyloid plaque (blue). Objects of axonal
1969 spheroids (red), axons (yellow) and amyloid plaques (purple) were generated according to the
1970 raw images after image annotation and analysis. Scale bars = 100 µm. **D-E.** Quantification
1971 showing (**D**) axon and (**E**) amyloid plaque volume (related to the experiment in **Figures 6Q and**
1972 **6R)**. Unpaired t test non-parametric two-tailed Mann Whitney test was used for all the statistical
1973 analysis.

1974

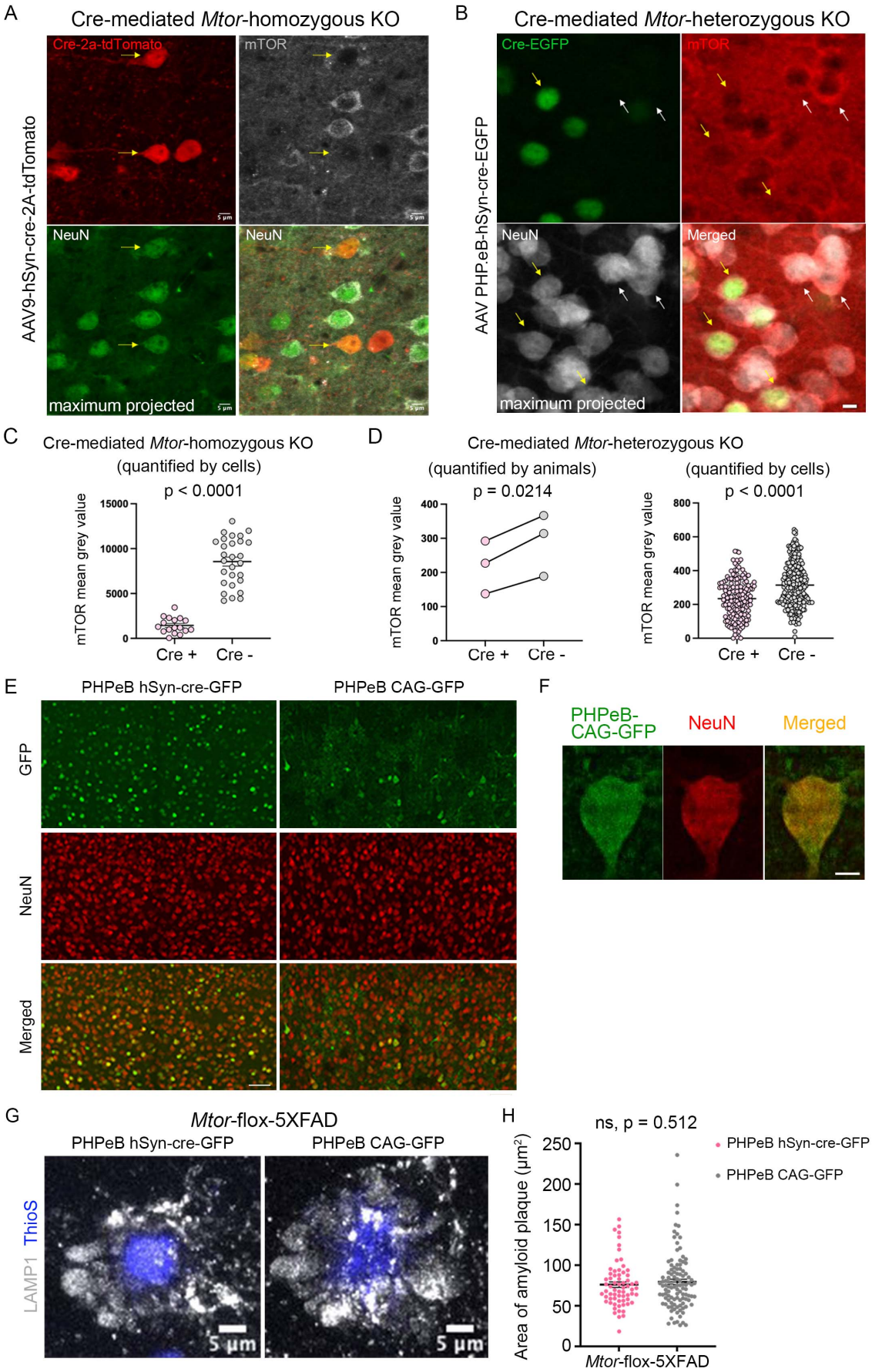
A
Cre-mediated Mtor-homozygous KO
AAV9-hSyn-cre-2A-tdTomato
Cre-2a-tdTomato
mTOR
NeuN
NeuN
maximum projected
B
Cre-mediated Mtor-heterozygous KO
AAV PHP.eB-hSyn-cre-EGFP
Cre-EGFP
mTOR
NeuN
Merged
maximum projected
C
Cre-mediated Mtor-homozygous KO
(quantified by cells)
p < 0.0001
mTOR mean grey value
Cre +
Cre -
D
Cre-mediated Mtor-heterozygous KO
(quantified by animals)
p = 0.0214
(quantified by cells)
p < 0.0001
mTOR mean grey value
Cre +
Cre -
E
PHPeB hSyn-cre-GFP
PHPeB CAG-GFP
GFP
NeuN
Merged
F
PHPeB-CAG-GFP
NeuN
Merged
G
Mtor-flox-5XFAD
PHPeB hSyn-cre-GFP
PHPeB CAG-GFP
ThioS
LAMP1
5 µm
5 µm
H
ns, p = 0.512
PHPeB hSyn-cre-GFP
PHPeB CAG-GFP
Area of amyloid plaque (µm²)
Mtor-flox-5XFAD

1975 **Figure S19. Genetic manipulation of mTOR signaling in mice**
1976 **A.** Uncropped immunofluorescence confocal images (shown in **Figures 7B** and **C**) show AAV9-
1977 hSyn-cre-2A-tdTomato-mediated *Mtor* complete knockout in homozygous *Mtor*-flox-5XFAD mice.
1978 mTOR expression (grey) was absent in Cre expressing neurons (red), compared to other adjacent
1979 neurons (green, NeuN) without Cre expression. **B.** AAV PHPeB-hSyn-cre-EGFP-mediated mTOR
1980 heterozygous knockout in heterozygous mTOR-flox-5XFAD mice. mTOR expression (red) was
1981 reduced in Cre expressing neurons (green), compared to other adjacent neurons (grey, NeuN)
1982 without Cre expression. **(A-B)** Scale bar = 5 µm. **C-D.** Quantification of mTOR fluorescence
1983 intensity (mean grey value) showed both (C) homozygous and (D) heterozygous mTOR knockout
1984 significantly reduced mTOR expression. Cre-virus positive (knockout) cells were compared to the
1985 Cre-virus negative (not knockout) cells in the same field of view. Cell bodies were outlined by
1986 NeuN staining. *Mtor*-floxed homozygous mouse (n=1), *Mtor*-floxed heterozygous mice (n=3). **E.**
1987 Immunofluorescence confocal images show AAV PHPeB virus (green) infection efficiency in the
1988 somatosensory cortex of 5XFAD mice. Anti-NeuN staining (red) indicate neuronal cell bodies.
1989 Scale bar = 50 µm. **F.** Immunofluorescence confocal image showing NeuN (red) positive neuronal
1990 soma (green, AAV PHPeB-CAG-EGFP infected) used for soma size quantification in **Figure 7K**.
1991 Scale bar = 5 µm. **G.** Representative images of axonal spheroid halos in heterozygous mTOR-flox-
1992 5XFAD mice under PHPeB-hSyn-cre-GFP (knockout) or PHPeB-CAG-GFP (not knockout) virus
1993 transduction. Spheroid halos were stained by LAMP1 (grey) and amyloid plaques were stained by
1994 ThioflavinS (blue). **H.** Quantification of the size of individual amyloid plaques within each ROI.
1995 Each dot represents a single amyloid plaque. *Mtor* knockout group n = 66 plaques, control group
1996 n = 109 plaques from 3 mice in each group. Unpaired t-test, two-tailed, p = 0.512.

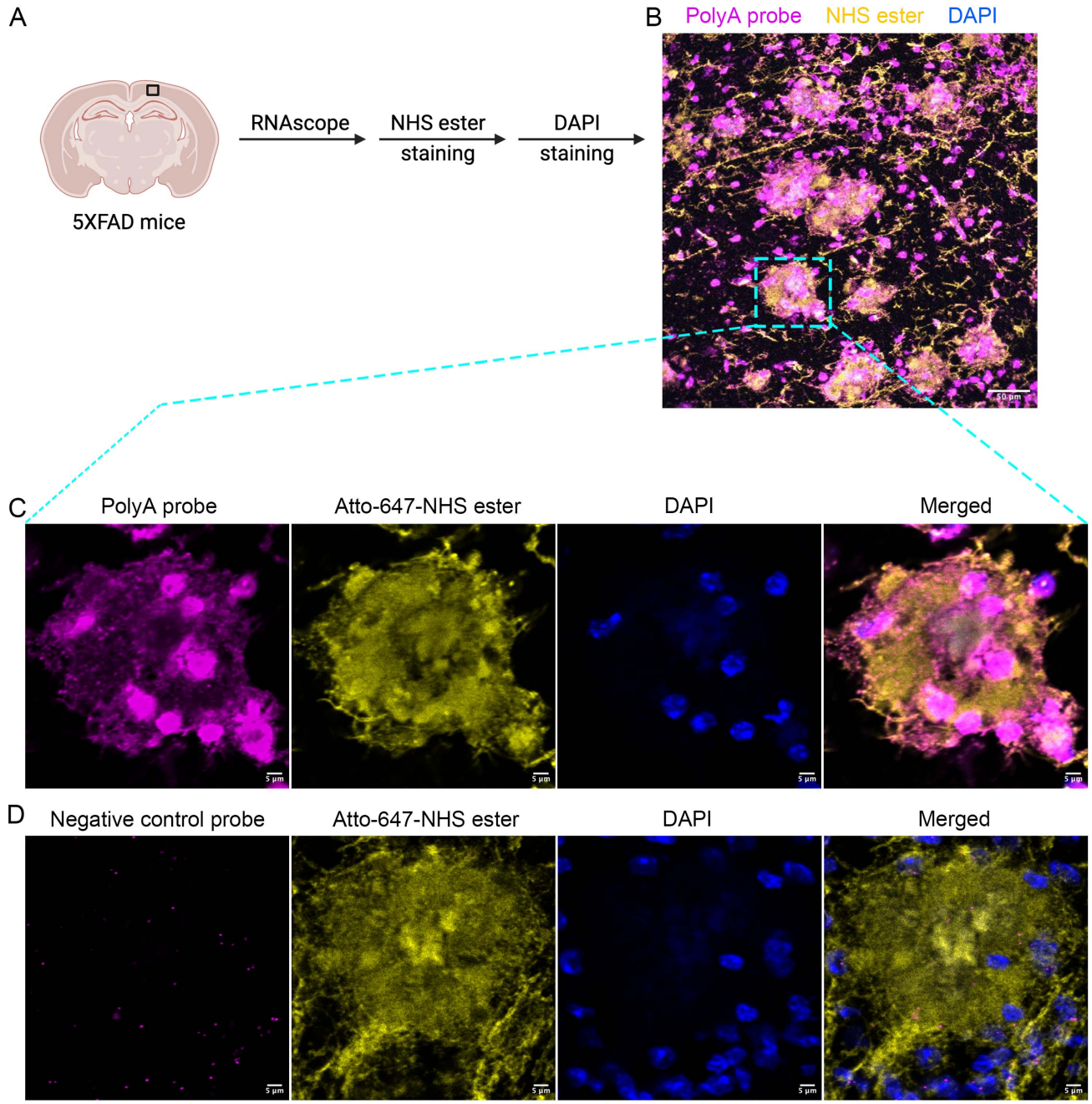

Figure S20. RNAscope revealed mRNA localization in axonal spheroids in 5XFAD mice
A. Schematic showing the RNAscope and staining pipeline in 5XFAD mice brain sections. **B-C.** (**B**) Low zoom and (**C**) high zoom (insert, blue box) RNAscope images showing mRNA species (PolyA probe labeled, magenta) are highly expressed in cell bodies (DAPI, blue) and are expressed within axonal spheroid halos (NHS ester labeled, yellow). NHS ester (yellow) labels axonal spheroid halo (including amyloid plaques), blood vessels and neuropil in 5XFAD mice cortex. **D.** High zoom image of negative control probe RNAscope in 5XFAD mice cortex. The RNA probe signal was mostly abrupted in both cell bodies (DAPI, blue) and axonal spheroid halos (NHS ester, yellow). Scale bar (**B**) 50 µm, (**C-D**) 5 µm.

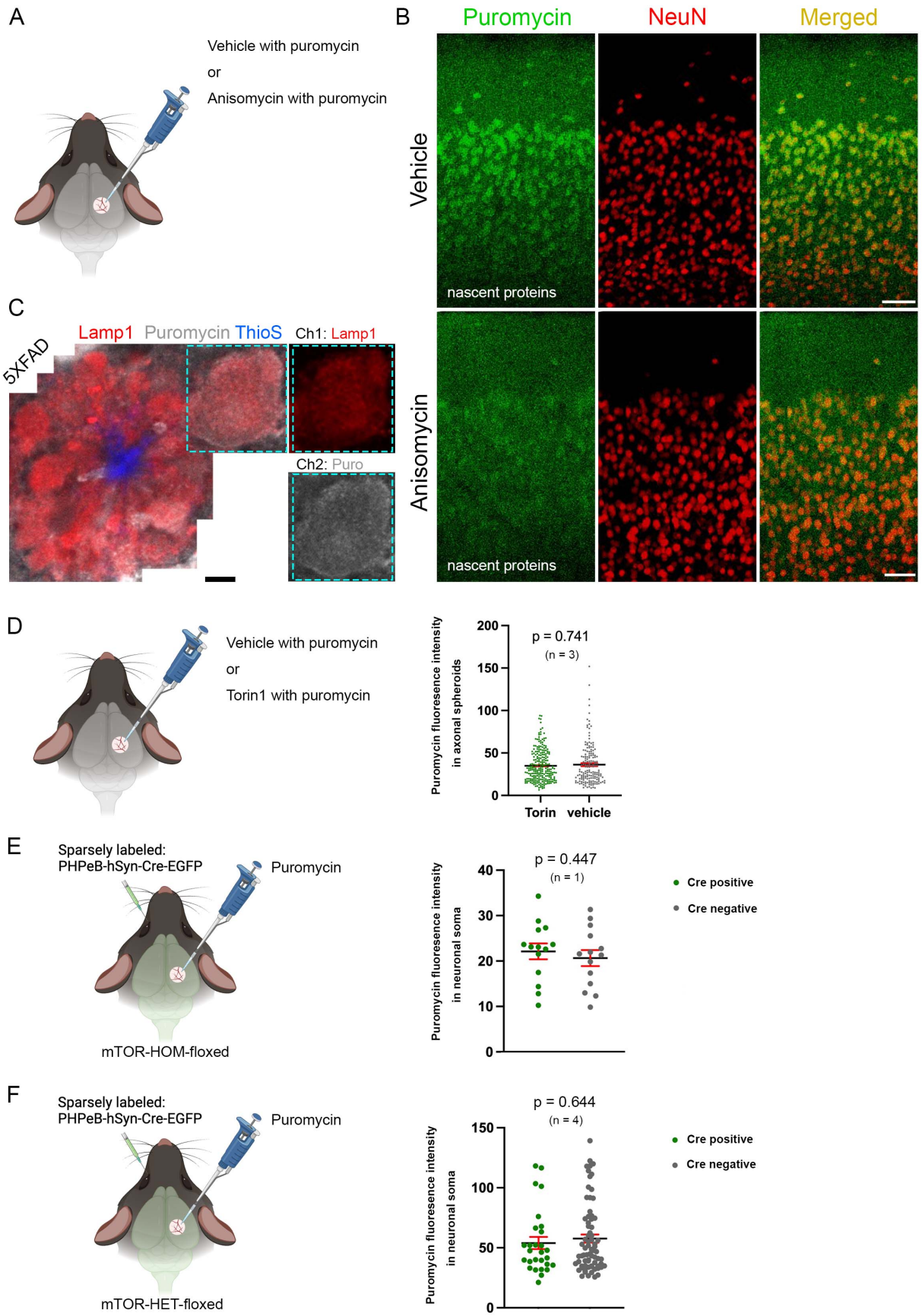
A
Vehicle with puromycin
or
Anisomycin with puromycin
B
Puromycin
NeuN
Merged
Vehicle
Anisomycin
nascent proteins
nascent proteins
C
5XFAD
Lamp1 Puromycin ThioS
Ch1: Lamp1
Ch2: Puro
D
Vehicle with puromycin
or
Torin1 with puromycin
Puromycin fluoresence intensity in axonal spheroids
p = 0.741
(n = 3)
Torin
vehicle
E
Sparsely labeled:
PHPeB-hSyn-Cre-EGFP
Puromycin
mTOR-HOM-floxed
Puromycin fluoresence intensity in neuronal soma
p = 0.447
(n = 1)
Cre positive
Cre negative
F
Sparsely labeled:
PHPeB-hSyn-Cre-EGFP
Puromycin
mTOR-HET-floxed
Puromycin fluoresence intensity in neuronal soma
p = 0.644
(n = 4)
Cre positive
Cre negative

2007

2008 **Figure S21. Puromycylation revealed nascent peptide in axonal spheroids in 5XFAD mice**
2009 **A.** Schematic showing puromycylation or anisomycin inhibition in mouse cortex. **B.**
2010 Immunofluorescence confocal images showing nascent proteins (puromycin labeled, green) in
2011 mouse cortex. Neuronal soma were labeled by NeuN (red). Anisomycin inhibition reduced the
2012 degree of puromycin labeling. **C.** Representative images showing nascent proteins (puromycin
2013 labeled, grey) in axonal spheroids (Lamp1, labeled) around amyloid plaque (ThioflavinS labeled,
2014 blue) in 5XFAD mice. Scale bar (**B-C**) 5 µm. **D.** Quantification showing 700 µM Torin treatment for
2015 two hours did not have an impact on puromycin labeling in axonal spheroids of 5XFAD mice
2016 cortices. Each dot represents an axonal spheroid, from n = 3 mice. **E-F.** Schematics showing (**E**)
2017 homozygous knockout or (**F**) heterozygous knockout of mTOR, by transducing PHP.eB-hSyn-Cre-
2018 GFP viruses in (**E**) mTOR-heterozygous-floxed or (**F**) -homozygous-floxed mice cortices.
2019 Quantification showing (**E**) homozygous knockout or (**F**) heterozygous knockout of mTOR in
2020 neurons did not have an impact on puromycin labeling in neuronal soma. Each dot represents a
2021 Cre positive, or Cre negative neuronal cell body (NeuN labeled) from (**E**) mTOR-HOM-floxed
2022 mouse (n = 1), and (**F**) mTOR-HET-floxed mice (n = 4). Unpaired t-test, two-tailed was performed.

2023 **SUPPLEMENTARY TABLES**

2024 **Table S1:** Raw and analyzed proteomics results of PAAS, Lamp1-labeling proximity labeling
2025 proteomics and neuronal soma in humans and mice.

2026 **Table S2:** Lists of newly identified and known PAAS proteins, as well as details and instructions of
2027 antibodies and immunofluorescence staining.

2028 **Table S3:** Proteomic sample information (also available at Proteomexchange).

2029 **Table S4:** Pathway enrichment analysis of Gene Ontology of PAAS proteomes in AD humans and
2030 mice.

2031 **Table S5:** IPA signaling pathways of PAAS proteomes in AD humans and mice.

2032 **Table S6:** GSEA analysis of PLD3-labeled proteomes in AD humans v.s. unaffected control humans.

2033 **SUPPLEMENTARY MOVIE CAPTION**

2034 **Movie S1:** A 3D video captured using FIB-SEM from a 12-month-old 5XFAD mouse shows
2035 spheroids (magenta) filled with a large number of vesicles, located around amyloid plaques (cyan).